Article

SOURCE DATA | TRANSPARENT PROCESS | OPEN ACCESS | CHECK FOR UPDATES

EMBO Molecular Medicine

Tenascin-C orchestrates radiotherapy-induced head and neck tumor regression

Thomas Loustau[1,2,3,17]✉, Ioanna Mitrentsi[1,2,17], Nuohan Wang[1,2], Caroline Spenlé[1,2,4], Alexia Pavlidaki[1,2], Thibaud Tranchant[1,2], Gilles Riegel[1,2], Akhil Venu[1,2], Rime Oueidat[1,2], Manuel Koch[5], Marion Dumas[1,2], Fanny Wack[1,2], Aurelie Hirschler[6], Christine Carapito[6], Nicodème Paul[7], Raphael Carapito[7], Matthias Mörgelin[8], Uwe Hansen[9], Joyce Azzi[10,11], Lucie Aubergeon[12], Nathalie Salomé[1,2], Sayda Dhaouadi[13], Pierre Grenot[14], Balkiss Bouhaouala-Zahar[13], Simona La Cioppa[15], Philippe Oertle[15], Valerio Izzi[16], Marija Plodinec[15], Georges Noel[10,11], Hélène Burckel[10,11] & Gertraud Orend[1,2]✉

Abstract

Given that head and neck squamous cell carcinoma (HNSCC) patients have poor survival outcomes, a better understanding of the therapeutic benefits of ionizing irradiation (IR), the major treatment modality besides surgery, is needed. A confounding factor is the immunosuppressive tumor microenvironment determined by tenascin-C (TNC), a highly abundant extracellular matrix molecule upregulated by IR. We investigated the roles of TNC on radio-induced tumor regression in a murine oral HNSCC model expressing or lacking TNC. While tumors in a TNC-expressing host were radiosensitive, they were radioresistant in TNC genetically depleted mice. We identified fibroblast reticular cells (FRCs) as critical regulators. TNC plays a compartmentalized and dual role in regulating tumor radiosensitivity with a detrimental role in the tumor stroma opposed to an essential role in the tumor-draining lymph nodes. This is relevant as a high FRC signature and high TNC levels together correlate with shorter HNSCC patient survival. TNC-expressing FRCs may be an excellent novel target to improve radiotherapy-induced tumor eradication, as our TNC targeting MAREMO peptide reduced tumor cell numbers and plasticity upon IR.

Keywords Tenascin-C; Radiotherapy; Fibroblast Reticular Cells; Tumor Draining Lymph Nodes; MAREMO Peptide
Subject Category Cancer
https://doi.org/10.1038/s44321-026-00406-8

Received 2 April 2025; Revised 11 February 2026; Accepted 2 March 2026
Published online: 31 March 2026

Introduction

Head and neck squamous cell carcinoma (HNSCC) is an aggressive malignancy with poor patient survival despite advances in therapy (reviewed in Chinn and Myers, 2015). Ionizing radiation (IR) remains a key treatment strategy, effectively inducing tumor and stromal cell death and activating anti-tumor immunity through the tumor-draining lymph nodes (TdLNs), which serve as critical sites for T-cell priming and expansion (Buchwald et al, 2020; Koukourakis and Giatromanolaki, 2022). However, IR paradoxically fosters an immunosuppressive tumor microenvironment (IS-TME), which limits its therapeutic efficacy (Menon et al, 2019; Guo et al, 2023). A central component of the IS-TME is tenascin-C (TNC), an extracellular matrix (ECM) glycoprotein implicated in immune modulation and tumor progression across various cancers (Yilmaz et al, 2022). In HNSCC, fibroblast reticular cells (FRCs) are a major source of TNC (Spenlé et al, 2020). TNC promotes immune evasion by inducing tolerogenic molecules, skewing macrophages toward an M2 phenotype, enhancing regulatory T cell (Treg) infiltration, and dampening CD8 + T cell responses (Deligne et al, 2020; Spenlé et al, 2020; Jachetti et al, 2015). Moreover, TNC induces the expression of ECM molecules that form immunosuppressive niches, so-called tumor matrix tracks (TMT) (Spenlé et al,

[1]INSERM UMR_S 1109, The Tumor Microenvironment Laboratory, Hôpital Civil, Institut d'Hématologie et d'Immunologie, Strasbourg, France. [2]University of Strasbourg, Strasbourg, France. [3]University of Strasbourg, UPR CNRS 9002, ARN, IUT Louis Pasteur, 1 allée d'Athènes, Schiltigheim, France. [4]University of Strasbourg, ESBS, INSERM-ERL1321, groupe Biothérapie peptidique, Pôle Api, Bâtiment D, 300 Boulevard Sébastien Brant, Illkirch, France. [5]University Cologne, Faculty of Medicine and University Hospital Cologne, Center for Dental, Oral and Maxillofacial Medicine (central facilities), Cologne, Germany. [6]Laboratoire de Spectrométrie de Masse BioOrganique, Institut Pluridisciplinaire Hubert Curien (IPHC), UMR 7178, Université de Strasbourg, CNRS, Infrastructure Nationale de Protéomique ProFi - UAR2048, Strasbourg, France. [7]Laboratoire d'ImmunoRhumatologie Moléculaire, INSERM UMR_S 1109, Plateforme GENOMAX, ITI Médecine de Précision de Strasbourg, Transplantex NG, Faculté de Médecine, Fédération Hospitalo-Universitaire OMICARE, Strasbourg, France. [8]Colzyx AB, Lund, Sweden. [9]Institute for Musculoskeletal Medicine (IMM), University Hospital Muenster, Muenster, Germany. [10]Institut de Cancérologie Strasbourg Europe (ICANS), UNICANCER, Radiobiology Laboratory, Paul Strauss Comprehensive, Cancer Center, Strasbourg, France. [11]ICube, UMR7357, Equipe Imagerie Multimodale Intégrative en Santé, Université de Strasbourg, Strasbourg, France. [12]University of Strasbourg, UPR CNRS 3572, I2CT, 2 allée Konrad Roentgen, Strasbourg, France. [13]Pasteur Institute of Tunis, NanoBioMedika research Team, 13 Place Pasteur - B.P. 74 - 1002, Tunis, Tunisia. [14]Laboratoire d'ImmunoRhumatologie Moléculaire, INSERM UMR_S 1109, Plateforme CYTOMAX, Institut d'Hématologie et d'Immunologie, Strasbourg, France. [15]Artidis, Hochbergerstrasse 60c, Basel, Switzerland. [16]Faculty of Biochemistry and Molecular Medicine at University of Oulu, Oulu, Finland. [17]These authors contributed equally as first authors: Thomas Loustau, Ioanna Mitrentsi. ✉E-mail: thomas.loustau@unistra.fr; gertraud.orend@inserm.fr

The paper explained

Problem

Ionizing radiation is the standard treatment for head and neck tumors and effectively reduces tumor burden. However, it simultaneously induces an immunosuppressive tumor microenvironment, particularly marked by increased expression of the tumor-promoting extracellular matrix glycoprotein tenascin-C (TNC). In this study, we sought to determine the specific contribution of TNC to tumor response following irradiation, using models with genetic or functional loss of TNC.

Results

Our work reveals that tenascin-C plays multiple regulatory roles in tumor radiosensitivity. In addition to directly influencing tumor cells, irradiation profoundly alters the phenotype of fibroblastic reticular cells (FRCs), a major source of TNC both within the tumor and in tumor-draining lymph nodes (TdLNs). Irradiation-surviving FRCs expand and acquire enhanced immunosuppressive properties, thereby promoting tumor progression. We demonstrate that physical interactions between tumor cells and FRCs drive FRC expansion and activation, increased tumor-cell survival and radioresistance, all in a TNC-dependent manner. Irradiation also remodels the TdLNs, where FRCs maintain the structural and functional networks required for adaptive immunity. In TNC-deficient tumor-bearing mice, TdLN immunity is deregulated, which likely contributes to the observed radioresistance.

Impact

TNC supports tumor regrowth after irradiation, in contrast to its protective role within the TdLNs, where TNC maintains immune-supportive functions. Our findings indicate that the balance between these opposing roles critically shapes radiotherapy outcomes. This identifies both FRCs and TNC as promising targets to enhance radiotherapeutic efficacy. Importantly, a high intratumoral abundance of highly TNC-expressing FRCs correlates with reduced survival in irradiated head and neck cancer patients. Finally, we demonstrate that therapeutic targeting of TNC using the MAREMO peptide increases tumor radiosensitivity, underscoring its clinical potential.

Synopsis

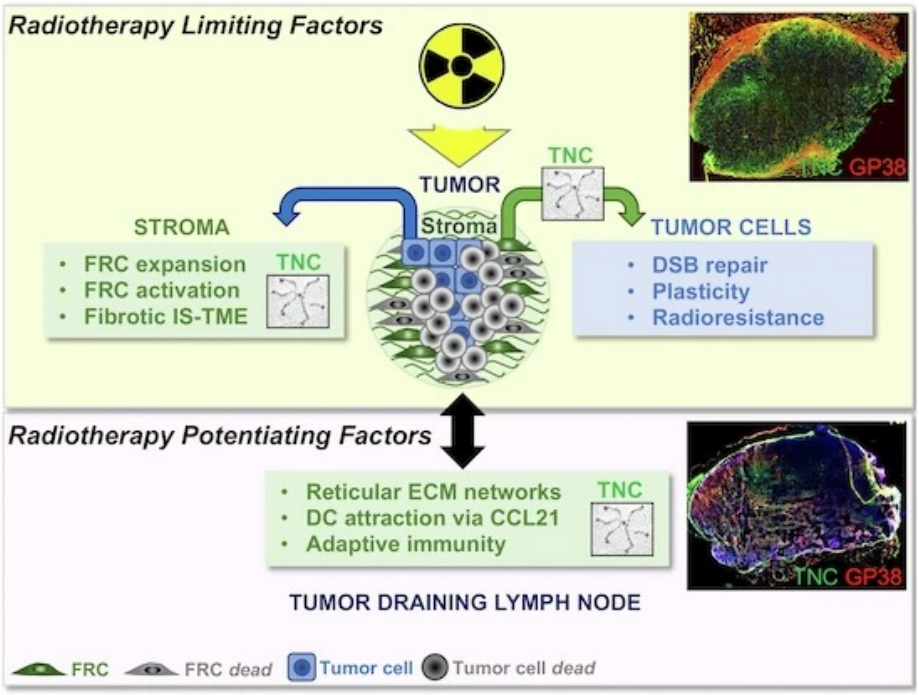

Radiotherapy lowers tumor burden but also induces tenascin-C (TNC), promoting immunosuppression and radioresistance; unlike in radiosensitive tumor draining lymph nodes, TNC-positive reticular fibroblasts promote tumor radioresistance, enabling radiosensitization by a TNC targeting MAREMO peptide.

- In HNSCC, fibroblast reticular cell (FRC) abundance is increased after radiotherapy through tenascin-C (TNC) dependent mechanisms.
- TNC is shown to determine distinct FRC phenotypes in the tumor microenvironment and tumor draining lymph nodes.
- TNC-dependent FRCs are demonstrated to promote tumor cell DNA double-strand break repair, plasticity and radioresistance.
- Radio-induced plasticity and tumor cell survival are shown to be reduced by TNC targeting with the MAREMO peptide.
- High intratumoral abundance of TNC-expressing FRCs is associated with inferior overall survival in HNSCC patients.

Article

SOURCE DATA | TRANSPARENT PROCESS | OPEN ACCESS | CHECK FOR UPDATES

EMBO Molecular Medicine

Tenascin-C orchestrates radiotherapy-induced head and neck tumor regression

Thomas Loustau[1,2,3,17]✉, Ioanna Mitrentsi[1,2,17], Nuohan Wang[1,2], Caroline Spenlé[1,2,4], Alexia Pavlidaki[1,2], Thibaud Tranchant[1,2], Gilles Riegel[1,2], Akhil Venu[1,2], Rime Oueidat[1,2], Manuel Koch[5], Marion Dumas[1,2], Fanny Wack[1,2], Aurelie Hirschler[6], Christine Carapito[6], Nicodème Paul[7], Raphael Carapito[7], Matthias Mörgelin[8], Uwe Hansen[9], Joyce Azzi[10,11], Lucie Aubergeon[12], Nathalie Salomé[1,2], Sayda Dhaouadi[13], Pierre Grenot[14], Balkiss Bouhaouala-Zahar[13], Simona La Cioppa[15], Philippe Oertle[15], Valerio Izzi[16], Marija Plodinec[15], Georges Noel[10,11], Hélène Burckel[10,11] & Gertraud Orend[1,2]✉

Abstract

Given that head and neck squamous cell carcinoma (HNSCC) patients have poor survival outcomes, a better understanding of the therapeutic benefits of ionizing irradiation (IR), the major treatment modality besides surgery, is needed. A confounding factor is the immunosuppressive tumor microenvironment determined by tenascin-C (TNC), a highly abundant extracellular matrix molecule upregulated by IR. We investigated the roles of TNC on radio-induced tumor regression in a murine oral HNSCC model expressing or lacking TNC. While tumors in a TNC-expressing host were radiosensitive, they were radioresistant in TNC genetically depleted mice. We identified fibroblast reticular cells (FRCs) as critical regulators. TNC plays a compartmentalized and dual role in regulating tumor radiosensitivity with a detrimental role in the tumor stroma opposed to an essential role in the tumor-draining lymph nodes. This is relevant as a high FRC signature and high TNC levels together correlate with shorter HNSCC patient survival. TNC-expressing FRCs may be an excellent novel target to improve radiotherapy-induced tumor eradication, as our TNC targeting MAREMO peptide reduced tumor cell numbers and plasticity upon IR.

Keywords Tenascin-C; Radiotherapy; Fibroblast Reticular Cells; Tumor Draining Lymph Nodes; MAREMO Peptide
Subject Category Cancer
https://doi.org/10.1038/s44321-026-00406-8

Received 2 April 2025; Revised 11 February 2026;
Accepted 2 March 2026
Published online: 31 March 2026

Introduction

Head and neck squamous cell carcinoma (HNSCC) is an aggressive malignancy with poor patient survival despite advances in therapy (reviewed in Chinn and Myers, 2015). Ionizing radiation (IR) remains a key treatment strategy, effectively inducing tumor and stromal cell death and activating anti-tumor immunity through the tumor-draining lymph nodes (TdLNs), which serve as critical sites for T-cell priming and expansion (Buchwald et al, 2020; Koukourakis and Giatromanolaki, 2022). However, IR paradoxically fosters an immunosuppressive tumor microenvironment (IS-TME), which limits its therapeutic efficacy (Menon et al, 2019; Guo et al, 2023). A central component of the IS-TME is tenascin-C (TNC), an extracellular matrix (ECM) glycoprotein implicated in immune modulation and tumor progression across various cancers (Yilmaz et al, 2022). In HNSCC, fibroblast reticular cells (FRCs) are a major source of TNC (Spenlé et al, 2020). TNC promotes immune evasion by inducing tolerogenic molecules, skewing macrophages toward an M2 phenotype, enhancing regulatory T cell (Treg) infiltration, and dampening CD8 + T cell responses (Deligne et al, 2020; Spenlé et al, 2020; Jachetti et al, 2015). Moreover, TNC induces the expression of ECM molecules that form immunosuppressive niches, so-called tumor matrix tracks (TMT) (Spenlé et al,

[1]INSERM UMR_S 1109, The Tumor Microenvironment Laboratory, Hôpital Civil, Institut d'Hématologie et d'Immunologie, Strasbourg, France. [2]University of Strasbourg, Strasbourg, France. [3]University of Strasbourg, UPR CNRS 9002, ARN, IUT Louis Pasteur, 1 allée d'Athènes, Schiltigheim, France. [4]University of Strasbourg, ESBS, INSERM-ERL1321, groupe Biothérapie peptidique, Pôle Api, Bâtiment D, 300 Boulevard Sébastien Brant, Illkirch, France. [5]University Cologne, Faculty of Medicine and University Hospital Cologne, Center for Dental, Oral and Maxillofacial Medicine (central facilities), Cologne, Germany. [6]Laboratoire de Spectrométrie de Masse BioOrganique, Institut Pluridisciplinaire Hubert Curien (IPHC), UMR 7178, Université de Strasbourg, CNRS, Infrastructure Nationale de Protéomique ProFi - UAR2048, Strasbourg, France. [7]Laboratoire d'ImmunoRhumatologie Moléculaire, INSERM UMR_S 1109, Plateforme GENOMAX, ITI Médecine de Précision de Strasbourg, Transplantex NG, Faculté de Médecine, Fédération Hospitalo-Universitaire OMICARE, Strasbourg, France. [8]Colzyx AB, Lund, Sweden. [9]Institute for Musculoskeletal Medicine (IMM), University Hospital Muenster, Muenster, Germany. [10]Institut de Cancérologie Strasbourg Europe (ICANS), UNICANCER, Radiobiology Laboratory, Paul Strauss Comprehensive, Cancer Center, Strasbourg, France. [11]ICube, UMR7357, Equipe Imagerie Multimodale Intégrative en Santé, Université de Strasbourg, Strasbourg, France. [12]University of Strasbourg, UPR CNRS 3572, I2CT, 2 allée Konrad Roentgen, Strasbourg, France. [13]Pasteur Institute of Tunis, NanoBioMedika research Team, 13 Place Pasteur - B.P. 74 - 1002, Tunis, Tunisia. [14]Laboratoire d'ImmunoRhumatologie Moléculaire, INSERM UMR_S 1109, Plateforme CYTOMAX, Institut d'Hématologie et d'Immunologie, Strasbourg, France. [15]Artidis, Hochbergerstrasse 60c, Basel, Switzerland. [16]Faculty of Biochemistry and Molecular Medicine at University of Oulu, Oulu, Finland. [17]These authors contributed equally as first authors: Thomas Loustau, Ioanna Mitrentsi. ✉E-mail: thomas.loustau@unistra.fr; gertraud.orend@inserm.fr

2020; Murdamoothoo et al, 2021; Fonta et al, 2023). TMT might phenocopy immune-regulating reticular matrix networks or so-called conduits in TdLNs as well as other lymphoid tissues, where TNC is an integral component (Spenlé et al, 2015; Huang et al, 2018; Drumea-Mirancea et al, 2006; Panocha et al, 2025). By sequestering soluble factors that attract immune cells, TNC creates an adhesive substratum that retains dendritic cells (DCs), macrophages (M-phages), and CD8 + T cells in the tumor stroma. This physical restriction prevents these immune cells from interacting with the tumor cells, thereby inhibiting both innate and adaptive immune responses (Spenlé et al, 2020; Deligne et al, 2020; Murdamoothoo et al, 2021). As IR induces TNC in human and mouse models (Spenlé et al, 2021; Omori et al, 2024; Toyomasu et al, 2022) we aimed to determine whether TNC plays a role in IR-induced tumor regression. To address this possibility, we applied the previously used carcinogen 4-NQO (4-Nitroquinoline 1-oxide)-induced tongue oral squamous cell carcinoma (OSCC) model, recapitulating the genetic alterations of human HNSCC (Wang et al, 2019) in mice, that express TNC (wild-type, WT) or are genetically depleted of TNC (TNC knockout, TNCKO). We investigated these tumors and the TdLNs at the cellular and molecular levels, including the immune cell infiltrate and FRCs, and observed that tumors expressing TNC were radiosensitive in contrast to TNC-depleted tumors, which were radioresistant. We discovered that TNC exerts opposing roles, promoting tumor regrowth after irradiation, while supporting immune functions within the TdLNs, where TNC maintains immune-supportive functions. Our findings indicate that the balance between these opposing roles critically shapes radiotherapy outcomes. We identified both FRCs and TNC as promising targets to enhance radiotherapeutic efficacy. High intratumoral levels of FRCs with strong TNC expression are associated with poorer survival in irradiated HNSCC patients. Moreover, therapeutic inhibition of TNC using the MAREMO peptide enhances tumor radiosensitivity, highlighting its potential clinical relevance.

Results

Expression of TNC impacts tumor radiosensitivity, and immune cell infiltration in the TdLNs of a murine model of OSCC

To investigate the effect of IR on tumors, we used tumor-bearing mice with 4NQO-induced tongue OSCC in both WT and TNCKO hosts. The tumors were then locally irradiated with a single dose of 2 Gray (Gy), a dose that represents the standard daily fraction used in conventional clinical fractionation protocols for head and neck cancer (5 × 2 Gy over 7 weeks), thereby enabling direct translational comparison to human regimens (Combs et al, 2005). We selected single-dose rather than fractionated irradiation to minimize confounding variables inherent to multi-fraction scheduling while maintaining a clinically relevant dose per fraction. This single-dose approach provided a controlled and reproducible perturbation of the tumor–stroma–immune ecosystem that induced tumor regression while preserving sufficient tissue for comprehensive downstream analysis. We collected the tumors and TdLNs 6 weeks later for further investigation in order to determine their longer-term consequences (Fig. EV1A). As previously reported, WT mice developed an average of two tumors per tongue, in contrast to TNCKO mice, which showed an average of one tumor per tongue (Fig. EV1B; Appendix Fig. S1A (Spenlé et al, 2020)). While the number and size of the tumors regressed upon 2 Gy IR in WT mice expressing TNC, this was not observed in TNCKO mice, indicating that tumors are radiosensitive in the presence of TNC, but not in its absence (Figs. 1A and EV1B). Whereas most IR-treated tumors in TNCKO mice were in situ carcinomas, TNC-expressing tumors presented a lower proportion of in situ carcinomas, accompanied by a higher prevalence of invasive carcinomas and in situ carcinomas expressing keratin. This suggests a tumor progression-promoting effect of IR, however, only in TNC-expressing tumors (Appendix Fig. S1B). As increased stiffness counteracts IR tumor remission (Mottareale et al, 2024), we applied atomic force microscopy (AFM) measurements and noticed that the TNC-depleted tumors showed no difference in stiffness in comparison to the WT tumors (Appendix Fig. S1C, Batasheva et al, 2024). By staining for Ki67 and subsequent signal quantification, we demonstrate a reduced proliferation rate upon 2 Gy IR in agreement with a reduced number and size of tumors in a TNC expression context (Fig. 1B,C). However, the already lowered proliferation in tumors depleted of TNC showed no further decrease upon irradiation (Figs. 1A,C and EV1B). By TNC staining, we confirmed higher TNC expression in the WT tumors and proved its absence in the TNCKO tumors (Fig. 1B). As TNC orchestrates an immune suppressive TME in this model (Spenlé et al, 2020), we used the leukocyte marker CD45 and the myeloid/dendritic (DC) cell marker CD11c, imaged immune cells using flow cytometry (all cells) or tissue staining (tumor islet cells) (Figs. 1D–F and EV1C; Appendix Fig. S1D–O). Whereas the number of leukocytes and DCs increased in the TNCKO tumors, their numbers were lower in WT tumors. Moreover, while these cells further decreased inside the tumor islets in the irradiated WT tumors, they did not in the irradiated TNCKO tumors (Fig. 1D,E; Appendix Fig. S1E, Spenlé et al, 2020). As TNC impacted CCR7+ expressing DCs (Spenlé et al, 2020), we used flow cytometry to analyze CCR7+ cells and showed TNC-dependent differences upon IR, in a similar direction. Whereas CCR7+ cells comprising DCs, macrophages, CD4 + T cells, Tregs, and CD8 + T cells were highly abundant in TNC-expressing IR tumors, they were much less present in the TNC-depleted IR tumors (Fig. 1E; Appendix Fig. S1D–I).

By flow cytometry, we observed that FRCs are more numerous upon IR in the TNC-expressing tumors, whereas TNC-depleted tumors presented much lower FRC levels (Figs. 1G and EV1D). In order to understand whether the FRC abundance influences the expression of CCL21, one of the ligands of CCR7 (Nagira et al, 1997), we applied ELISA. CCL21 expression was significantly higher in the WT tumors after IR, which was not the case in the TNCKO context, where CCL21 levels remained at already reduced levels (Fig. 1H). As there were more DCs in the TNCKO tumors and tumor islets, potentially acting as antigen-presenting cells (APCs), we investigated whether DCs were also more abundant in the TdLNs of these mice. Indeed, DCs were more numerous in these lymph nodes, although again their numbers remained unaffected by IR (Fig. EV1E). While CCR7+ and activated DCs (CD86 + /CD80 +) were more abundant, immune suppressive Tregs were less numerous in the TdLNs and tumors of mice lacking TNC, presumably reflecting a deregulated adaptive immunity

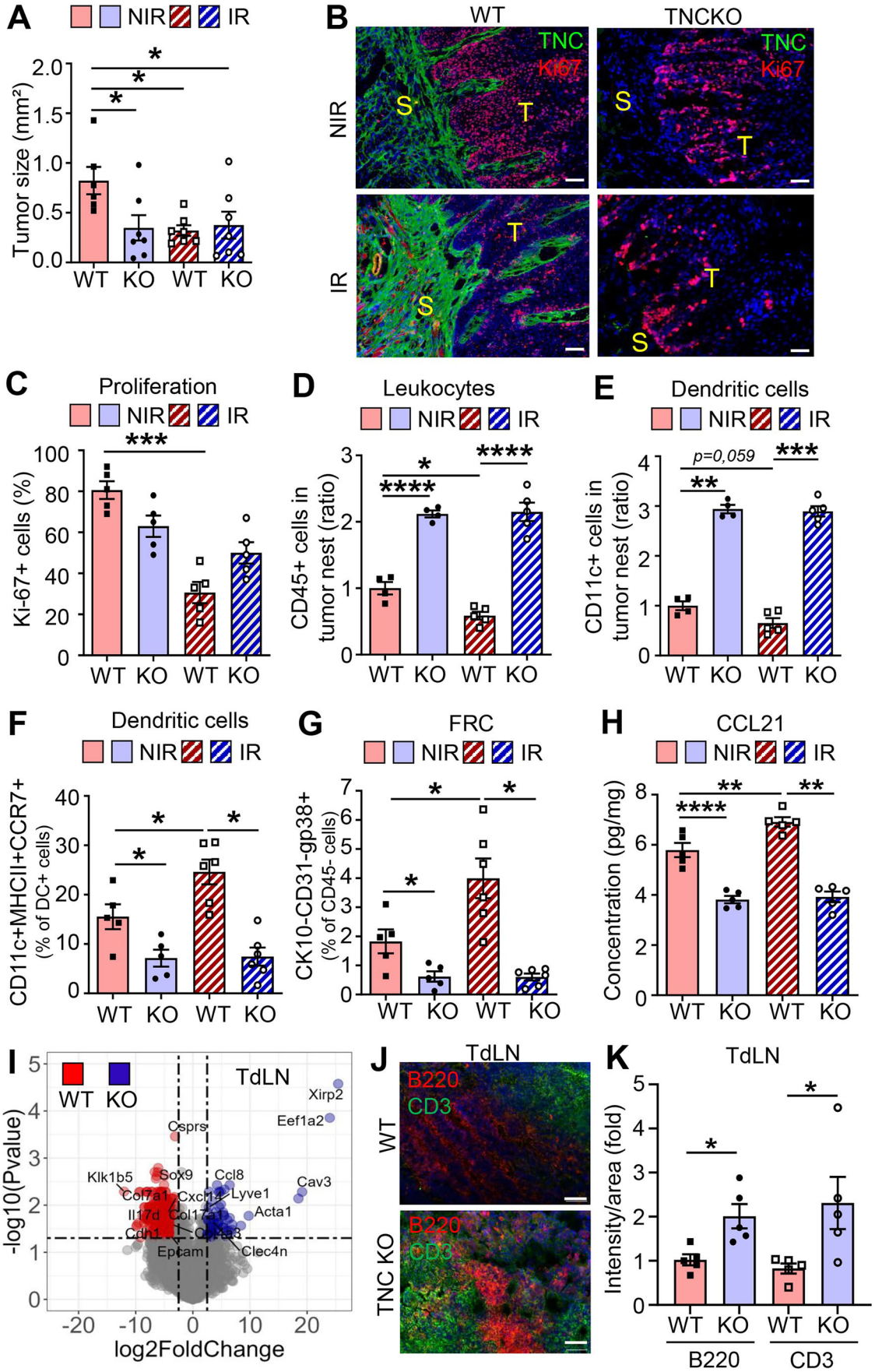
A
NIR
IR
Tumor size (mm²)
2.0
1.5
1.0
0.5
0.0
WT KO WT KO
B
WT
TNCKO
NIR
IR
TNC
Ki67
S
T
C
Proliferation
Ki-67+ cells (%)
100
80
60
40
20
0
D
Leukocytes
CD45+ cells in tumor nest (ratio)
E
Dendritic cells
p=0,059
CD11c+ cells in tumor nest (ratio)
F
Dendritic cells
CD11c+MHCII+CCR7+ (% of DC+ cells)
G
FRC
CK10-CD31-gp38+ (% of CD45- cells)
H
CCL21
Concentration (pg/mg)
I
TdLN
WT KO
-log10(Pvalue)
log2FoldChange
Xirp2
Eef1a2
Csprs
Klk1b5
Sox9
Ccl8
Cav3
Col7a1
Cxcl14
Lyve1
Il17d
Col17a1
Acta1
Cdh1
Epcam
Clec4n
J
TdLN
B220
CD3
WT
TNC KO
K
TdLN
Intensity/area (fold)
B220
CD3

Figure 1. Expression of TNC impacts tumor radiosensitivity, and immune cell infiltration in the TdLNs of a murine model of OSCC.

(**A**) Quantification of the tongue tumor size in 4NQO-treated WT and TNCKO (KO) mice non-irradiated (NIR) or irradiated (IR), $n = 5$ per group. (**B**) Representative IF images for TNC and the proliferation marker Ki67 in NIR and IR 4NQO tumors of WT and TNCKO mice (T, tumor islet, S, Stroma). Scale bar, 200 µm. (**C**) Quantification of Ki67-positive cells (%) in the tumor per image. Four images per tumor, $n = 5$ mice per group. (**D**, **E**) Quantification of the immunostaining signal to evaluate the spatial distribution of the CD45+ (**D**) and CD11c+ (**E**) cells present in the tumor nest as a ratio of positive cells over the total of cells per image. (**F**, **G**) FACS analysis of CCR7+ dendritic cells (DC) expressed as a ratio (%) of the total DC population (CD45 + , CD11c + , MHCII +) (**F**) and FRCs (GP38 + , CK10-, CD31−) expressed as a ratio (%) of the total CD45-negative cells (**G**). (**H**) ELISA for CCL21 in NIR and IR 4NQO tumors of WT and TNCKO mice. $N = 5$–6 per group. (**I**) Volcano plot of deregulated genes, after RNA sequencing of the TdLN of WT and TNC KO mice. $N = 3$ WT and 3 TNCKO TdLN. (**J**, **K**) Representative IF images for CD3 and B220 in the TdLN of WT or TNC KO mice (**J**) and quantification of their intensity/area in $n = 2$–4 sections of $N = 5$ TdLNs per group (**K**). Scale bar, 50 µm. Mean ± SEM; Kruskal–Wallis test and Dunn post-test, $^{*}P < 0.05$, $^{**}P < 0.01$, $^{***}P < 0.005$. The exact P values are listed in Appendix Table S5. Source data are available online for this figure.

(Fig. EV1F–H; Appendix Fig. S1E–O). The levels of CCL21, needed not only as a chemoattractant but also for cell activation (Marsland et al, 2005), were similar in the TdLNs of both genotypes and remained unchanged upon IR in the WT and TNC-depleted conditions (Appendix Fig. S1P). This altogether suggests that TNC might play a role in sustaining adaptive immunity responses against the tumor cells, in particular in response to IR, a function that seems to be impaired in the TdLNs of TNCKO mice. This is supported by a higher number of immature CCR7+ cells comprising CD4 + T and CD8 + T cells in the tumors of the TNC-depleted mice (Appendix Fig. S1M,N).

Next, we determined gene expression differences in the TdLNs between genotypes using RNA seq analysis with a cutoff of log2 fold change of 2.5 and an adjusted P value of 0.05, and noticed profound differences in 493 genes to be downregulated and 62 genes to be upregulated in WT in comparison to the TNCKO TdLNs. Gene Set Enrichment Analysis (GSEA) demonstrated that the most deregulated categories showed downregulation of processes linked to the structural organization of the reticular networks (epithelial tube formation, cell–cell junctions, namely *Cdh1*, *Epcam*) in the TNC-depleted TdLNs, while processes involved in adaptive immunity (immunoglobulin production, B cell mediated immunity) were the most upregulated categories in the same TdLNs (Figs. 1I and EV1I; Appendix Table S1). Moreover, markers for lymphatic endothelial cells (LEC) such as Lyve 1 and Acta 1 (for cytoskeletal reorganization) were higher in the TNCKO than WT TdLNs, indicating an altered cellular composition and function in the TdLNs in the absence of TNC (Appendix Table S1). As expected, TNC was not expressed in the TdLNs of the TNCKO mice, whereas TNC overlaps with glycoprotein 38 (GP38) staining, supporting that FRCs express TNC in the WT TdLNs (Appendix Fig. S1Q). Staining for CD3 and B220 and subsequent quantification showed an excessive number of positive cells in the TNCKO TdLNs, suggesting a deregulated and impaired immunity (Fig. 1J,K; Appendix S1U). Gene expression was largely unaffected by 2 Gy IR in both WT and TNCKO TdLNs and showed similar patterns in direct comparisons of irradiated TdLNs from the two genotypes. However, the profound difference in the non-irradiated TdLNs between genotypes is lost upon IR. This suggests a major role of TNC in regulating the TdLN function and little or no direct effect of 2 Gy IR on gene expression (Appendix Fig. S1R–T). A heatmap representation reveals a significantly deregulated expression of around 200 genes comprising GO terms related to inflammatory and adaptive immune responses, including *Ccl28, Cx3cl1*, and *Il34* downregulated and, *Ifng, Granzyme B, Ifnar, Il17, Ctla4*, and *Cd4*, as well as several *Igh* and *Igk* genes upregulated in the TdLNs from TNCKO mice (Appendix S1V,W; Table S1).

Altogether, these results demonstrate that TNC plays a profound role in OSCC radiosensitivity, the IR-induced stroma responses, the immune cell infiltration, and TdLN functionality. Importantly, a deregulated and likely impaired TdLN immunity in the TNC-depleted mice may contribute to the radioresistance of the tumors in these mice. In the tumors, we discovered an increased abundance of FRCs upon IR that play an instrumental role in enforcing an IS-TME.

TNC regulates the FRC phenotype

To further explore the impact of TNC on the FRC phenotype, FRCs were isolated from the lymph nodes of two naïve 10-week-old TNCKO mice and were investigated as previously done for FRCs isolated from two age-matched naïve WT mice (Spenlé et al, 2020). While FRCs expressing TNC had an elongated fibroblastic cell shape with parallel aligned actin stress fibers, FRCs depleted of TNC were less well spread with poorly formed actin stress fibers, thus appearing smaller (Figs. 2A and EV2A). To better understand the FRC phenotypes we conducted RNA sequencing (RNA seq) (Appendix Table S2) and mass spectrometry (Mass spec) analysis (Appendix Table S3), followed by IF staining and ELISA, and observed profound TNC-dependent differences (however not between cell isolates) (Figs. 2B and EV2B). Expression of well-established lymph node FRC markers (Fletcher et al, 2015; Ferreira et al, 2021; Förster and Moschovakis, 2013), such as GP38 (podoplanin), VCAM-1, and Collagen VI (ColVI, ER-TR7 epitope), was largely reduced in TNCKO FRC isolates at both protein and mRNA levels (Fig. 2C; Appendix Table S3). As all lymph nodes were collected for FRC isolation, we wanted to know whether there are genotype-specific differences in the abundance of distinct FRC subtypes (Rodda et al, 2018). However, by comparing the abundance of subtype-specific gene expression markers, this was not the case (Appendix Fig. S2A). Expression of *Gp38*, *Vcam1, Col6a1, Ccl19*, and *Ccl21*, which are normally expressed by mature lymph node FRCs, was lower in the absence of TNC, highlighting that TNC is an important regulator of the FRC identity (Fig. 2C,D). Among the 12,456 expressed genes, 9% (1245) were upregulated, and 8% (1021) were downregulated in the two duplicates of TNCKO compared to the two duplicates of the WT FRCs (Appendix Table S2). From all 2717 proteins detected by mass spectrometry analysis, expression of 1310 proteins also showed a significant difference in the same samples. GSEA demonstrated downregulation of processes related to "fibroblast proliferation", "ECM expression and organization", "collagen production", "regulation of cell signaling", "cytokine activity/chemokine production" and "TGFβ signaling" at both mRNA and protein level (Fig. EV2D,E; Appendix Fig. S2B–E). Also, chemokine and cytokine expression was altered at the transcriptional level in the absence of TNC with *Tgfb1, Ccl21,*

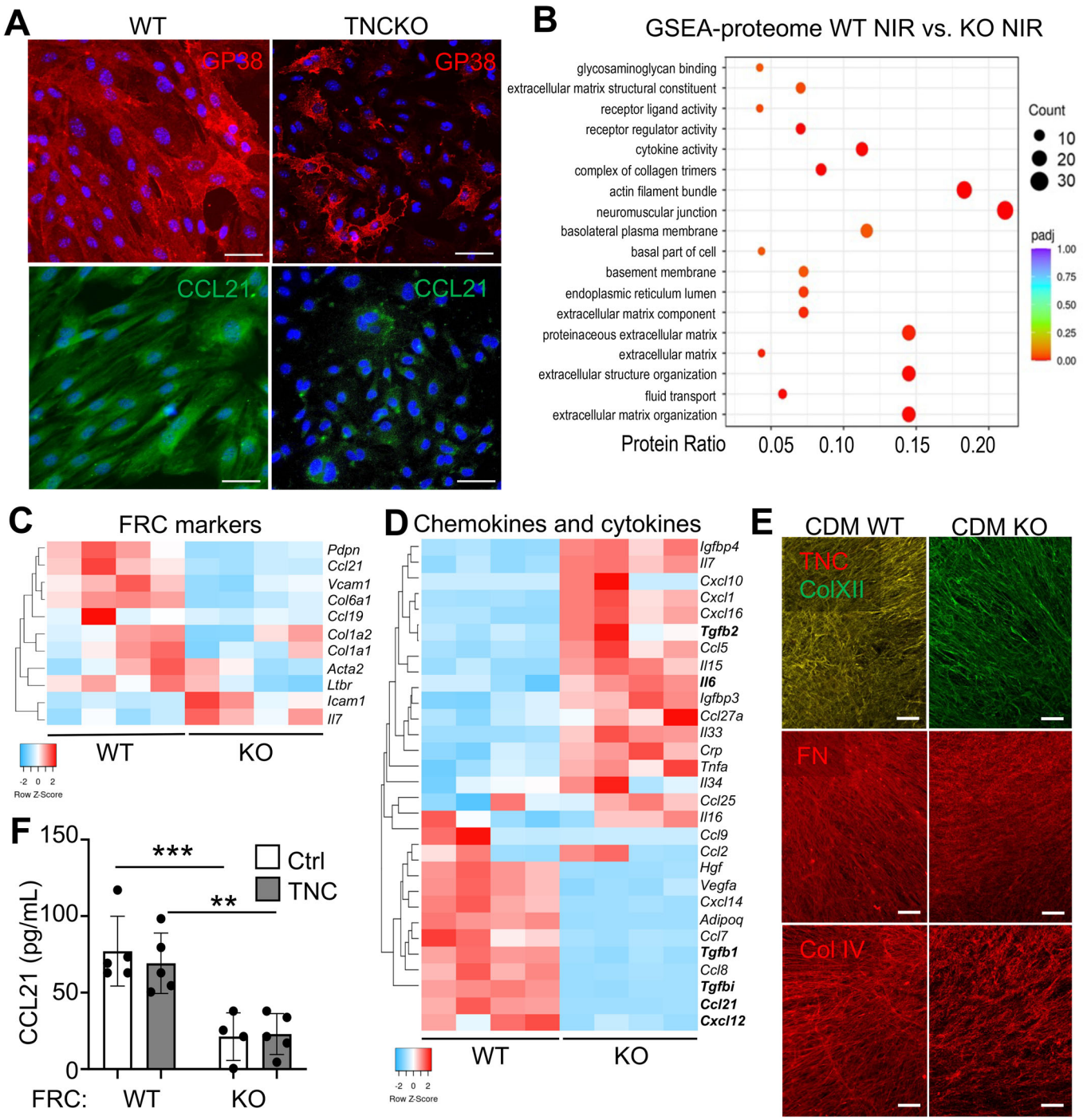

Figure 2. TNC expression plays a pivotal role in defining the FRC phenotype.

(**A**) Representative IF images for GP38 (podoplanin) and CCL21 in non-irradiated (NIR) FRCs isolated from lymph nodes of naïve WT or TNCKO mice. The same microscopic field of the image showing DAPI (blue) and GP38 (red) in the TNCKO FRCs was co-stained for the marker VCAM1 (green), which is displayed separately in Fig. EV2A. Scale bar, 50 µm. (**B**) Display of differentially expressed proteins in WT and TNCKO FRCs applying the GSEA analysis tool. The color code indicates the adjusted *P* value range and the black circles the approximate number of proteins that belong to each GO term. RNA seq gene expression analysis of WT and TNCKO FRCs represented as heatmaps for deregulated genes according to FRC markers (**C**) and chemokine and cytokine molecules (**D**). Bold text indicates genes with established roles in the respective category that are discussed in the text. (**E**) Representative image of Col XII, TNC, FN, and Col IV expression in the CDM of WT or TNCKO FRCs. Scale bar, 200 µm. (**F**) Quantification of CCL21 by ELISA in WT or TNCKO FRCs, either non-treated control (Ctrl) or treated with soluble TNC (10 µg/mL) for 24 h. $N = 4$ experiments. Mean ± SD, Kruskal–Wallis test and Dunn post-test, $^{*}P < 0.05$, $^{**}P < 0.01$ $^{***}P < 0.001$. The exact *P* values are listed in Appendix Table S5. Source data are available online for this figure.

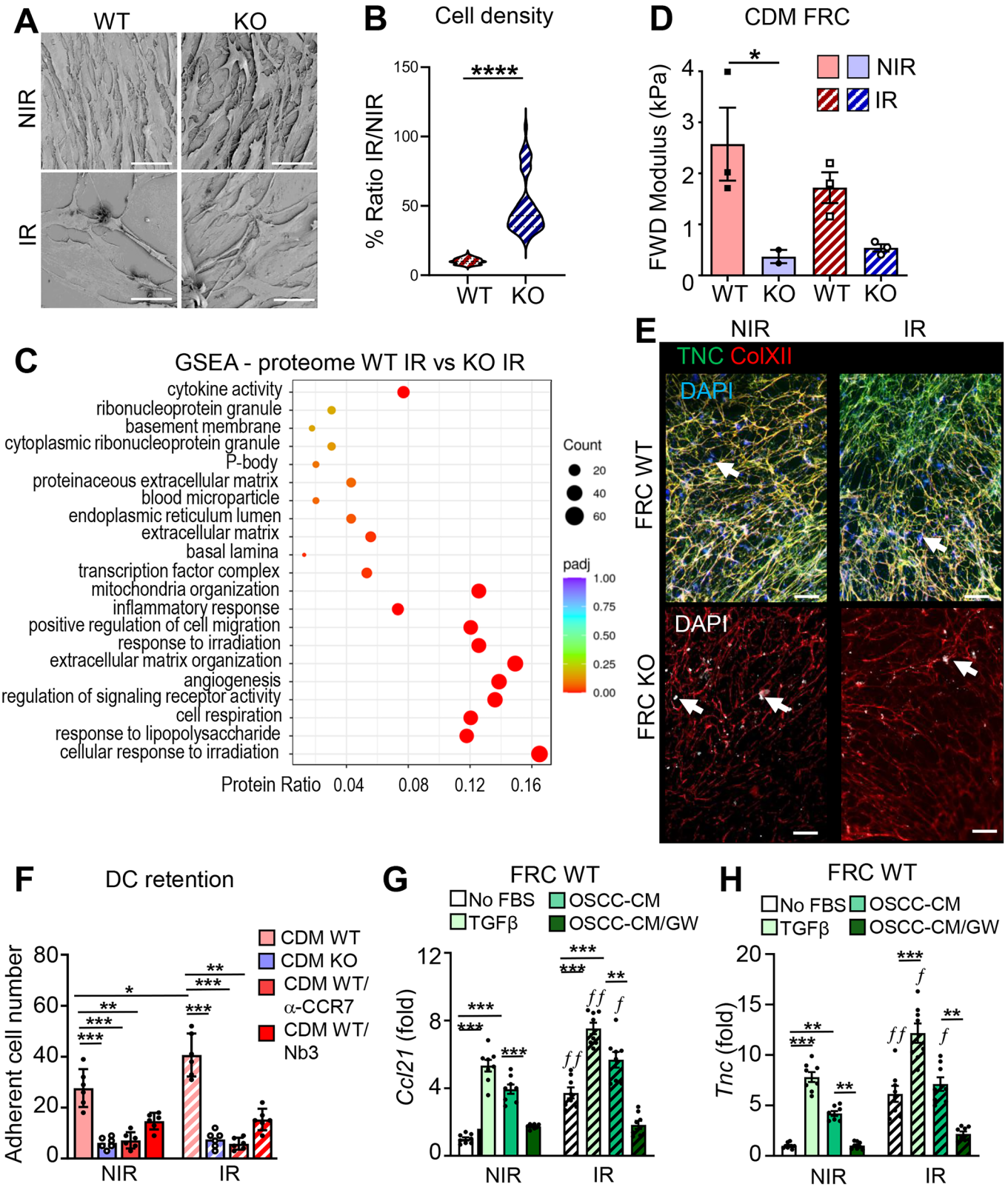

Cxcl12 to be lower and *Il7, Cxcl10* and *Il6* higher in the TNC-depleted tumors (Figs. 2D and EV2D; Appendix Fig. S2D,H; Appendix Tables S2 and S3). Next, we investigated the cell-derived matrix (CDM) that had been deposited by the FRCs over 10 days and observed a complete absence of TNC in the TNC-depleted FRCs, as expected, accompanied by reduced levels and less fibrillar or dense patterns of fibronectin (FN), Col IV and Collagen XII (Col XII) (Figs. 2E and EV2F). CCL21 expression was also significantly reduced

Figure 3. FRC cell responses to irradiation are dependent on TNC expression.

(**A**) Representative Scanning Electron Microscopy (SEM) images of irradiated (IR) or non-irradiated (NIR) WT and TNCKO FRCs. Scale bar, 50 µm. (**B**) Cell density (analysis of 100 SEM images for each condition) of WT and TNCKO FRCs expressed as a ratio of IR to NIR cells. Mean ± SD; Student *T* test, ****$P < 0.0001$. (**C**) GSEA map display of differentially expressed protein categories in WT or TNCKO FRCs after irradiation. The color code indicates the adjusted *P* value range, and the black circles the approximate number of proteins that belong to each GO term. (**D**) Forward (FWD) E-Modulus average (kPA) of the corresponding Atomic Force Microscopy measurement of the CDM of WT or TNCKO FRCs before (NIR) or after irradiation (IR). $N = 3$. Mean ± SEM (**E, F**) Representative IF images of DC2.4 cells adherent on the CDM from the FRCs (WT or KO) after the chemoretention assay. DC2.4 nuclei are stained with DAPI (arrows point at the nuclei) and were counted on the CDM in (**F**) upon migration toward CCL21, pre-treatment with the anti-CCR7 neutralizing antibody (αCCR7), the TNC inhibitory nanobody Nb3, or no treatment control. Scale bar, 200 µm. Mean ± SEM; $n = 6$ per condition; Kruskal–Wallis test and Dunn post-test, *$P < 0.05$, **$P < 0.01$, ***$P < 0.005$. (**G, H**) Expression of Ccl21 (**G**) and Tnc (**H**) was determined by qRTPCR after treatment of FRCs (WT, KO, NIR, IR) with TGFβ (10 ng/mL for 24 h) or with the CM from the OSCC13 cells in the presence or absence of GW788388 (GW). Mean ± SEM; $n = 6$–9 per condition; Kruskal–Wallis test and Dunn post-test, *$P < 0.05$, **$P < 0.01$. The exact *P* values are listed in Appendix Table S5. Source data are available online for this figure.

in the TNC-depleted FRCs (Fig. 2F; Appendix Fig. S2E). Consistent with what was previously shown in the WT FRCs, TNC addition did not upregulate CCL21 in the TNC-depleted FRCs, suggesting that TNC is not directly inducing CCL21 in either genotype cells (Fig. 2F; Appendix Fig. S2E, see below). Although lymphatic endothelial cells (LECs) are another important source of CCL21, their abundance, as determined by flow cytometry, did not differ between the two genotypes or upon IR, thus likely not contributing to the observed changes in CCL21 expression (Appendix Fig. S2F).

These results reveal that TNC has a key role in defining the FRC identity in both tumors and lymph nodes.

Irradiation enhances an immunosuppressive phenotype in FRCs in a TNC-dependent manner

By using electron microscopy (EM), we analyzed the phenotype of the irradiated FRCs and observed differences in cell shape and density. We observed a higher cell density and number of vesicles in the irradiated WT FRCs compared to the irradiated TNCKO cells, indicating an elevated cell death upon IR in the presence of TNC (Fig. 3A,B; Appendix Fig. S3A,B). Indeed, while only 10% of the TNC-expressing FRCs survived IR, a fivefold higher population of TNC-depleted FRCs (50%) remained viable after 2 Gy IR exposure (Fig. 3B).

RNA seq and proteomic analyses also demonstrated strong differences upon IR in both genotypes and in dependence of TNC (Fig. 3C; Appendix Fig. S3C). Upon IR, 22% (2842) of all 13,025 genes were differentially expressed with 1369 (11%) genes upregulated and 1473 (11%) genes downregulated in the irradiated WT FRCs compared to the irradiated TNCKO FRCs (Appendix Table S2). At the protein level, 530 proteins were deregulated in the TNC-expressing irradiated FRCs, whereas only 126 proteins in the TNC-depleted irradiated FRCs were impacted, again reflecting the lower radiosensitivity of the TNCKO FRCs (Fig. 3C; Appendix Fig. S3C and Appendix Table S3).

The most significantly deregulated category between genotypes upon IR, was "Cellular response to irradiation" where the WT cells showed induction by IR in contrast to the TNC-depleted FRCs that showed mostly reduced expression upon IR (Figs. 3C and EV3A; Appendix Fig. S3D and Appendix Table S3). In the irradiated WT FRCs these molecular categories comprised "Regulation of cell proliferation", "Cellular response to cytokines", "Regulation of leukocyte migration" (e.g., *Cxcl12, RhoA, Rac*), and "ECM organization" (e.g., LOX, LOXL3, MMPs 2, 11, 14), altogether indicating that IR induced an activated FRC phenotype in the fewer surviving TNC-expressing cells (Appendix Fig. S3E–I). While almost all gene ontology and GSEA proteome categories were downregulated in the irradiated TNC-depleted compared to the irradiated TNC-expressing FRCs, several proteins in the "Cellular respiration" pathway were upregulated in the TNC-depleted FRCs, potentially increasing metabolic activity contributing to their enhanced survival after IR (Appendix Fig. S3I).

To investigate potential differences in matrix stiffness in dependence of TNC and IR, we used AFM and noticed that despite an elevated expression of ECM molecules upon IR, the stiffness of the CDM deposited by the irradiated TNC-expressing FRCs was surprisingly not increased (Fig. 3D). Potentially altered crosslinking and/or degradation of the ECM networks upon IR may explain this phenotype, as e.g., LOX, TGM2, MMP2, MMP11 and MMP14 were upregulated upon IR (Appendix Fig. S3J,K). In contrast, stiffness was much reduced in the CDM from the TNC-depleted FRCs and remained unchanged upon IR, reinforcing the lack of IR responsiveness in the TNCKO FRCs (Fig. 3D). In support of an impact of IR on the matrix, EM image analysis of the tumors revealed spaces filled with loose matrix in the irradiated WT tumors (Appendix Fig. S3L).

As the proteome analysis revealed an increased expression of molecules involved in leukocyte migration and ECM organization in irradiated TNC-expressing FRCs, we wondered whether IR impacts migration and retention of DCs and performed a modified Tumor Infiltrating Leucocyte (TIL)-matrix-chemoretention assay on CDM deposited by the irradiated FRCs in the lower chamber in the context of CCl21 (Fig EV3F). First, staining of the CDM deposited by the TNCKO cells revealed a lowered Col XII expression and assembly in the absence of TNC, not only in the non-irradiated (NIR) but also in the IR condition (Fig. 3E). Although the CDM from TNC-depleted FRCs is still comprised of abundant fibrillar FN and Col IV and likely other matrix molecules, this matrix was impaired in retaining the DCs (Figs. 2E, 3F, and EV3C). In contrast, DC retention was elevated on CDM derived from the irradiated TNC-expressing FRCs and was significantly reduced with an anti-CCR7 antibody and with the TNC-specific nanobody 3 (Nb3), previously shown to block cell retention of DCs on TNC/CCL21 (Figs. 3F and EV3D, Dhaouadi et al, 2021). This suggests that IR enforces FRCs to retain DCs via a sticky TNC/CCL21 substratum. Taking into account the important role of TGFβ signaling in radio responses (Massagué, 2008) and given the increased TGFβ signaling in the TNC-expressing WT FRCs (Fig. EV2E; Appendix Table S3) and an increased expression of *Tgfb1* in these cells upon IR (Fig. EV3E), we addressed whether tumor cells can impact the FRC phenotype upon IR, potentially through TGFβ signaling. We collected conditioned medium (CM)

from OSCC13 cells and investigated gene expression in the irradiated FRCs by qRTPCR 48 h after exposure to either the CM or TGFβ (Fig. EV3F). This analysis revealed that both the OSCC13-derived CM and TGFβ itself induced expression of *Acta2, Col1a2, Tnc*, and *Ccl21* in the irradiated FRCs (more than in the non-irradiated counterparts), however, only when the cells were derived from a WT but not a TNCKO mouse (Fig. 3G,H; Appendix Fig. S3M–P). Most importantly, this effect was TGFβ-dependent as the TGFβRI inhibitor GW788388 (GW) impaired gene induction by IR. This result establishes an IR-stimulated crosstalk between OSCC13 cells and FRCs through TGFβ (Fig. EV3F; Appendix Table S3).

Altogether, we identified a profound effect of IR on FRC survival and phenotype. The surviving cells enforce the deposition of ECM and the expression of chemoattracting factors. TNC is crucial in defining the FRC identity, facilitating ECM deposition and promoting CCL21 expression, a process dependent on TGFβ signaling, a major pathway elicited by IR (Massagué, 2008). Moreover, TNC is essential for FRCs to establish a DC-retaining substratum, which again occurs in a TGFβ-dependent manner. Our results suggest that TGFβ signaling is largely impaired in the TNC-depleted FRCs by an unknown mechanism, which may contribute to the reduced response of FRCs to IR and subsequent tumor radioresistance.

Irradiation enforces a TNC-dependent tumor cell-fibroblast crosstalk, promoting activation of FRCs and tumor radioresistance

Having identified TGFβ secreted by the tumor cells to impact FRC responses upon IR, we wanted to know how the contact of the two cell types is impacted by IR and TNC. Therefore, we established FRCs with stable TNC knockdown (shTNC) and confirmed effective TNC repression by western blot (Appendix Fig. S4A). Notably, neither TNC knockdown nor complete knockout affected FRC expansion in vitro (Appendix Fig. S4B). Our RNA seq and mass spectrometry analysis revealed that the FRCs express integrin α7β1, typically restricted to muscle tissue (Song et al, 1993, 1992; Liu et al, 2008; Tomatis et al, 1999), which was marginally affected by TNC depletion (Appendix Fig. S4C,D). We subsequently used, integrin α7β1 along with GP38, to identify FRCs by flow cytometry and staining. Upon a OSCC13/FRC coculture we observed sorting of cells into tumor cell islets surrounded by the FRCs, which generated a 3D-like TNC-rich stroma, resembling the tumor islet-stroma segregation seen in human HNSCC (Figs. 4A and EV4A,B, Spenlé et al, 2020). In contrast, TNC-deficient FRCs failed to segregate and instead intermingled with tumor cells, suggesting a loss of structural organization (Figs. 4A and EV4A,B).

As OSCC13 cells are radiosensitive (Spenlé et al, 2021), we applied 10 Gy which is in a similar range of 5 ×2 Gy applied in the clinic (Combs et al, 2005) to reach an optimal effect. To dissect cell-type-specific responses to IR, the two cell populations were magnetically sorted using antibodies against GP38 and integrin α7β1. Sorted FRCs ($GP38^+/α7β1^+$) expressed GP38 and integrin α7β1 but lacked *Cdh1* encoding for E-cadherin (Ecad), whereas the negative fraction ($GP38^-/α7β1^-$) expressed high levels of *Cdh1*, identifying them as tumor cells (Appendix Fig. S4E,F). Subsequently, we compared gene expression in the irradiated cocultures to that of the monocultures. In the irradiated cocultures, FRCs became more activated by IR than in the monocultures as indicated by higher levels of *Ccl21*, TNC, GP38, α7β1, and *Col1a2* expression (Figs. 4B and EV4C–F; Appendix Fig. S4G–L). Except for IR-induced TNC mRNA changes, no other expression changes were observed in the TNC-depleted FRCs for all investigated genes, supporting an altered, potentially immature FRC phenotype in the absence of TNC (Figs. 4B and EV4D–F; Appendix Fig. S4G–L). Induction of TNC and GP38 in the irradiated FRCs was also confirmed by immunofluorescence staining of the cultured cells (Figs. 4C and EV4C).

In order to investigate the resistance of these cells to irradiation, we measured the RNA and protein levels of Rad51, the main factor of homologous recombination repair (Shinohara et al, 1992). Interestingly, Rad51 was elevated in the cocultures of OSCC13 and FRCs after IR, in a TNC-dependent manner, with this effect more pronounced in the tumor cells than in the FRCs (Fig. 4C,D; Appendix Fig. S4M,P).

One process that, along with its other effects, is well known to contribute to the radioresistance of the cancer cells, is epithelial to mesenchymal transition (EMT) (Theys et al, 2011; Nantajit et al, 2015). This phenomenon was also observed in our study. Specifically, in the irradiated cocultures, the expression of various markers analyzed apart from TNC itself, described as early EMT marker (Lüönd et al, 2021), also *Tgfb1*, *Vim* and *Twist* were elevated in the OSCC13 cells with a greater increase in comparison to the monocultures, again in a TNC-dependent manner (Figs. 4E,F and EV4C,D,G; Appendix Fig. S4Q–S). In parallel, *Cdh1* expression levels were decreased after IR, suggesting that upon IR, OSCC13 cells cocultured with TNC-expressing FRCs start undergoing EMT (Fig. EV4H; Appendix Fig. S4T). To further investigate the underlying mechanism, and since *Tgfb1* was increased in the OSCC13 tumor cells after irradiation (Fig. 4E), we used the TGFβRI inhibitor GW to abolish its action and investigated whether TGFβ signaling has an effect on the protein levels of Vim and the phosphorylated nuclear Smad3 (pSMAD3). Indeed, while both Vim and pSMAD staining increased in the cocultured OSCC13 cells after irradiation, this effect was diminished with the inhibitor, suggesting TNC-dependent pathway activation by IR (Fig. 4G–I). Also, *Cxcl12* (induced by IR in the FRCs, Appendix Fig. S3D) was increased in the cocultures with WT FRCs upon IR, whereas *Il6* remained unchanged, indicating a potential role for CXCL12 that has to be examined in the future (Appendix Fig. S4J,K).

Collectively, these results suggest that the coculture promotes efficient Double Strand Break (DSB) repair, specifically homologous recombination and plasticity in the tumor cells upon IR, thereby enhancing their radioresistance. In turn, the tumor cells impact the FRC phenotype through TGFβ signaling; upon irradiation, FRC numbers and activation increase, enforcing the formation of an IS-TME. TNC is a driving force of this intercellular communication, as TNC-depleted FRCs fail to respond to IR and to trigger the induction of radioresistance and plasticity in the tumor cells.

TNC expressing FRCs generate an IS-TME and promote OSCC13 tumor growth

To determine whether FRCs play a role in tumor growth and associated IR responses, we engrafted OSCC13 cells together with

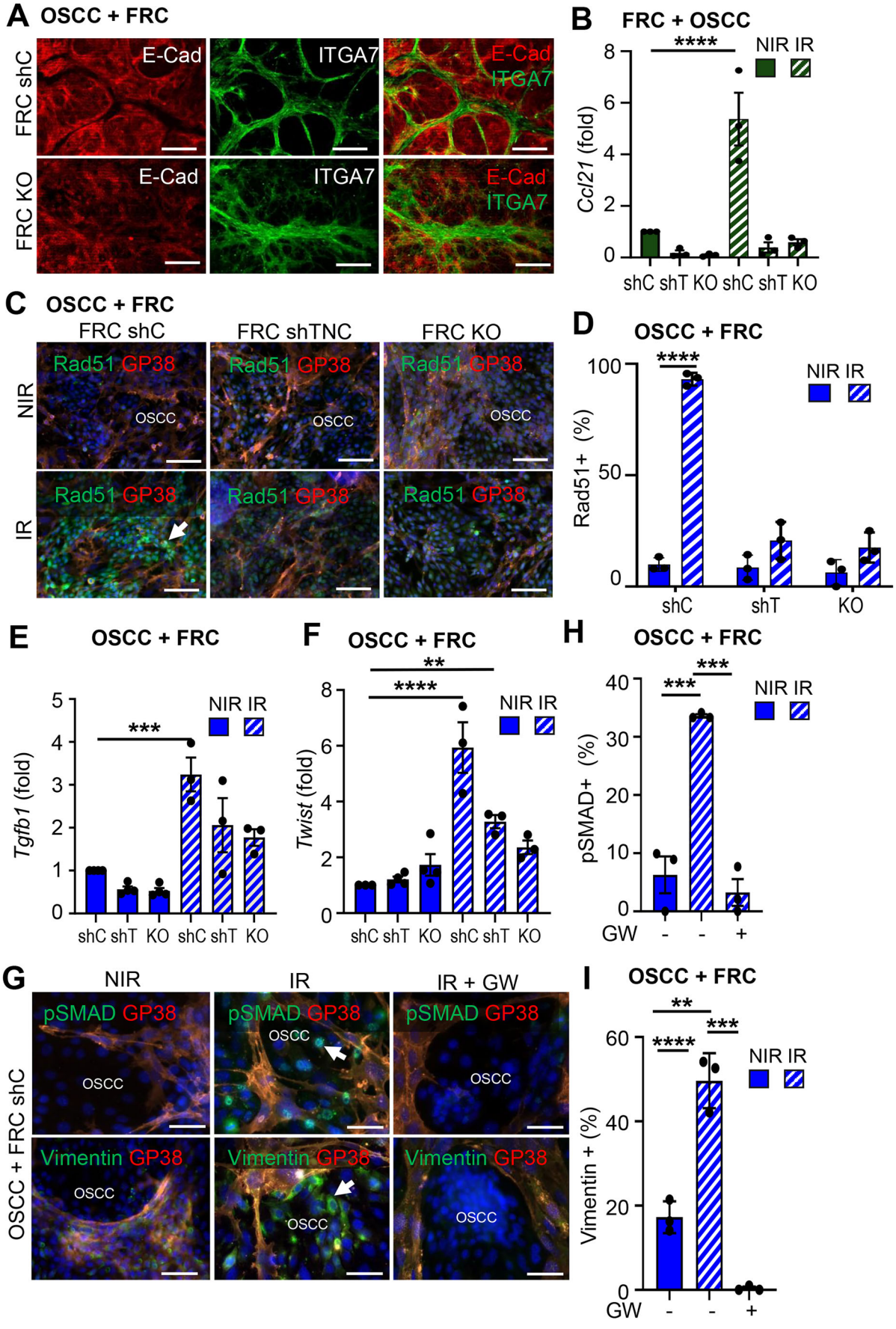
A
OSCC + FRC
FRC shC
FRC KO
E-Cad
ITGA7
E-Cad ITGA7
B
FRC + OSCC
****
NIR IR
Ccl21 (fold)
shC shT KO shC shT KO
C
OSCC + FRC
FRC shC
FRC shTNC
FRC KO
NIR
IR
Rad51 GP38
oscc
D
OSCC + FRC
****
NIR IR
Rad51+ (%)
shC
shT
KO
E
OSCC + FRC
***
NIR IR
Tgfb1 (fold)
shC shT KO shC shT KO
F
OSCC + FRC
**
****
NIR IR
Twist (fold)
shC shT KO shC shT KO
H
OSCC + FRC
***
***
NIR IR
pSMAD+ (%)
GW - - +
G
NIR
IR
IR + GW
OSCC + FRC shC
pSMAD GP38
Vimentin GP38
oscc
I
OSCC + FRC
**
***
****
NIR IR
Vimentin + (%)
GW - - +

Figure 4. The FRC-OSCC crosstalk impacts irradiation responses in a TNC-dependent manner.

(**A**) immunofluorescence images of OSCC13 (OSCC) and FRC (WT, shC, TNCKO) after coculture in a 2:1 ratio. Scale bar, 200 µm. (**B**) Gene expression (qRTPCR) analysis of Ccl21 expression in the cocultured FRCs after MACS, before or 2 days after exposure to 10 Gy IR. (**C**, **D**) GP38 and Rad51 immunofluorescence images of the cocultured OSCC and FRC (shC, shTNC,TNCKO) cells before or 2 days after exposure to 10 Gy IR (**C**) and quantification (%) of Rad51 positive OSCC cells (**D**). Arrows indicate the OSCC cells expressing Rad51. Scale bar, 200 µm. (**E**, **F**) qRTPCR analysis of *Tgfb1* (**E**) and *Twist* (**F**), in the cocultured OSCCs before or 2 days after exposure to 10 Gy IR. (**G**) Immunofluorescence images of OSCCs and FRCs, cocultured in a 2:1 ratio for a total of 4 days, 2 days prior to and 2 days after exposure to 10 Gy IR, under GW treatment for the indicated molecules. Arrows indicate the OSCC cells that undergo EMT. (**H**, **I**) Signal quantification in the OSCC cells expressed as % of all tumor cells. Scale bar, 50 µm, $N = 3$ experiments; Error bars represent mean ± STDEV; ordinary one-way ANOVA test, $^{**}P < 0.01$. $^{***}P < 0.005$. $^{****}P < 0.0001$. The exact *P* values are listed on Appendix Table S5. Source data are available online for this figure.

the FRCs. Single tumor cell engraftments showed a very heterogeneous tumor latency or no engraftment in the given 15-week time frame. In contrast, co-engraftment with the FRCs reduced the tumor latency, resulting in consistent tumor growth across engraftments (Fig. 5A). Tissue staining and qRTPCR analysis revealed more abundant FRCs in the coengrafted tumors (Figs. 5B,C and EV5A). However, also in the single OSCC grafted tumors, ERTR7+ FRCs were present, suggesting that host-derived FRCs have infiltrated the tumors. We further demonstrated that in the co-engrafted OSCC13/FRCs tumors TMTs were enforced characterized by prominent expression and alignments of collagen VI (ColVI, ERTR7), laminin (LM) and TNC (Figs. 5B and EV5A; Appendix Fig. S5A). This was associated with recruitment of leukocytes into the stromal compartment (imaged by CD45 staining) and the establishment of an IS-TME, as evidenced by an increased expression of *Col1a2, Tnc, Acta2, Ccr7*, *Ccl21*, *Tgfb1, Il10*, and *Il17* (Fig. 5C). To address whether TNC expressed by the FRCs plays a role in shaping the TME, we compared co-engraftments of tumor cells with either WT FRCs or TNCKO FRCs. Indeed, tumors with WT FRCs showed faster growth during the first 18 days than their TNCKO counterparts as well as the tumor cells engrafted alone (Figs. 5D and EV5B). After this initial delay in tumor growth, TNCKO FRC-engrafted tumors started to catch up, which could be explained by substantial host FRC infiltration highly expressing TNC. This can be seen by the presence of host-derived GP38+ cells expressing TNC, next to the engrafted TNCKO FRCs (only GP38 +) (Fig. EV5C; Appendix Fig. S5B). Nevertheless, at the endpoint, the WT FRC-engrafted tumors revealed clearly established TMTs and higher TNC expression levels, confirming major TNC-instructed differences implemented by the FRCs (Figs. 5E and EV5D; Appendix Fig. S5B,C).

In summary, FRCs co-engraftment promotes a TME in the neck with similarities to those seen in HNSCC, exemplified by enforced TNC and *Ccl21* expression, TMT formation and an IS-TME. Our findings indicate that TNC plays a key role in supporting the ability of FRCs to build an IS-TME and, to generate a functional milieu in the TdLNs, in particular relevant upon IR.

Targeting TNC with MAREMO peptide MP5 reduces tumor cell proliferation and plasticity upon IR

Having established that TNC expressing FRCs promote an IS-TME, we wanted to know whether tumor targeting of TNC would impact IR responses. For that, we used 3D cocultures of OSCC13 cells grown together with FRCs, forming spheroids (Fig. 6A; Appendix Fig. S6A,B). Irradiation of these spheroids with 10 Gy IR led to a decrease of cell numbers with a similar tendency upon 5 ×2 Gy IR (Fig. 6B; Appendix Fig. S6C). This effect was even further pronounced by the addition of MP5 post-IR for 3 days, indicating reduced proliferation by MP5 in the given time frame (Fig. 6B). To confirm the delivery of MP5 inside the spheroids, we used its labeled surrogate Cy5-MP5, that we have already shown to colocalize with TNC in other tumors (Li et al, 2024). Consistently, Cy5-MP5 also colocalized with TNC-rich regions in the spheroids (Fig. 6A; Appendix Fig. S6A,B) and was similarly active in reducing DC retention as the untagged peptide (Fig. EV6A). Both peptides also impaired binding of the fibronectin type III (FNIII) 4-6 (FN4-6) molecule to the TNC FNIII 1-5 (TN1-5) molecule in a dose-dependent manner as demonstrated by a competitive ELISA with an IC50 of 3 µM (Cy5-MP5) and 5 µM (MP5), respectively (Fig. EV6B). A similar effect on reducing cell numbers upon IR in combination with MP5 was also seen in human CAL33 spheroids cocultured with human immortalized fibroblasts (TIF) where Cy5-MP5 also colocalized with TNC (Fig. 6C,D).

By staining, we observed enhanced Vim expression upon 10 Gy IR (and 5 × 2 Gy), indicative of EMT in the OSCC13 spheroids, which was blocked by Cy5-MP5 addition, revealing a similar effect on plasticity as previously reported for MP5 (Fig. 6E,F; Appendix Fig. S6B,D,E (Li et al, 2024).

Next, we addressed the TNC specificity of MP5 using two approaches. First, TNC-depleted mixed OSCC13 (shTNC)/FRC (TNCKO) spheroids were exposed to IR and MP5 as described and showed no reduction in cell numbers, unlike TNC-expressing spheroids (Fig. 6B; Appendix Fig. S6F). Second, we compared gene-expression profiles from the NT193 breast cancer cells exhibiting low TNC expression with those obtained upon MP5 treatment (Murdamoothoo et al, 2021; Li et al, 2024). Principal component analysis (PCA) revealed that MP5-treated cells cluster with shTNC cells, whereas PBS-treated controls cluster with shC cells (Fig. EV6C). This pattern indicates that MP5 induces a transcriptional shift that partially phenocopies TNC depletion. In line with this observation, MP5-treated tumor cells displayed transcriptional patterns more similar to shTNC than to control cells (Fig. EV6D). Importantly, several immune-related pathways were consistently enriched in both conditions. Gene Ontology categories linked to "adaptive immune response," "antigen presentation," and "cytokine response" were similarly upregulated following TNC knockdown and MP5 exposure (Fig. EV6E; Appendix Fig. S6G,H), suggesting that MP5 triggers downstream immune-regulatory programs typically suppressed by TNC.

In summary, our results suggest that targeting TNC with the MAREMO peptide MP5 after IR can enforce a reduction in cell numbers and reduce plasticity, two key events towards an improved

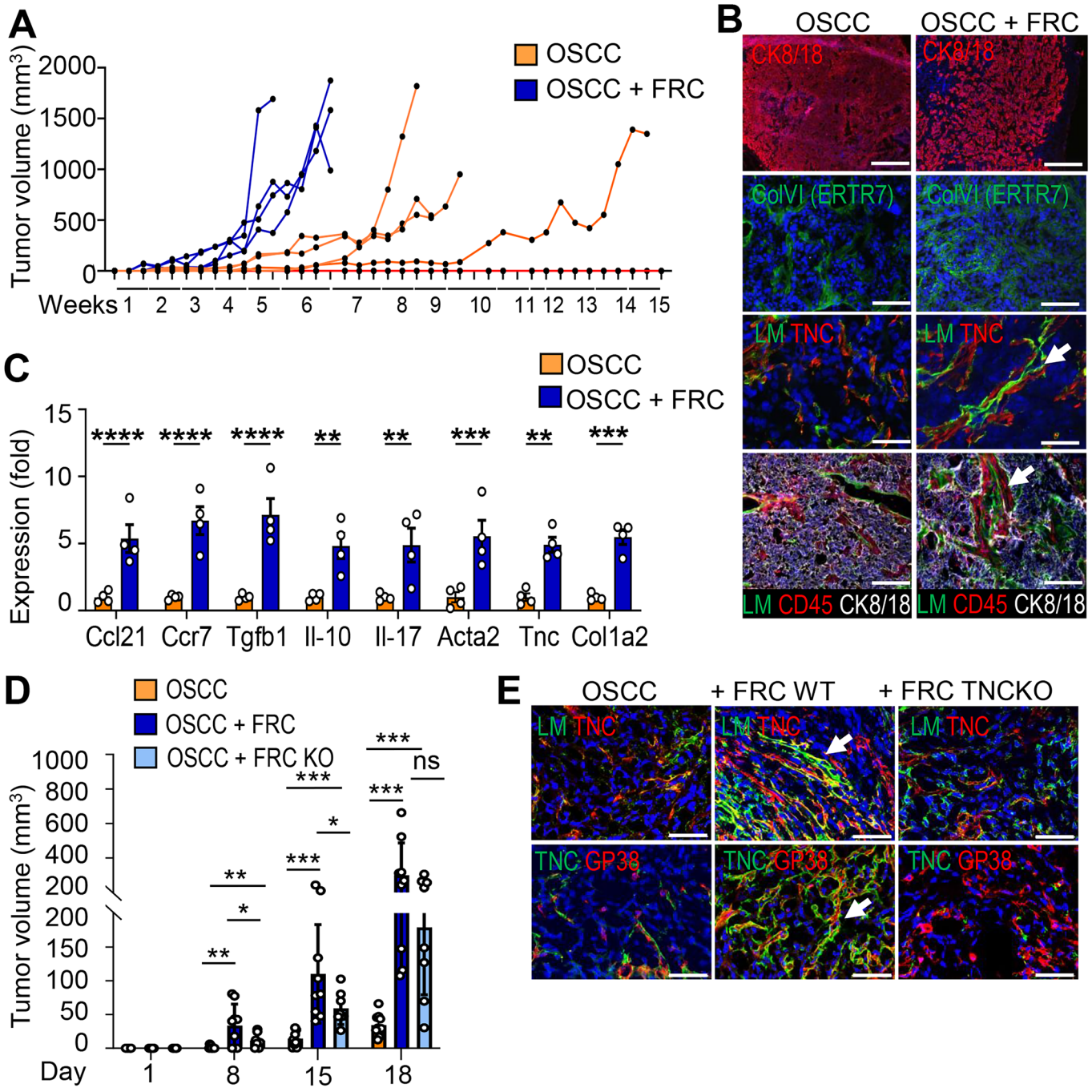

Figure 5. Coengraftment of FRCs promotes OSCC tumorigenesis and an immunosuppressive TME.

(**A**) Monitoring of tumor volumes upon engraftment of 3×10^6 OSCC13 (OSCC) cells alone (orange, $N = 5$ mice) or OSCC cells combined with WT FRC cells (blue, $N = 4$ mice), in a 5:1 ratio into the neck of C57Bl6 mice during the indicated time frame (1 to 15 weeks). (**B**) Representative immunofluorescence images for CK8/18, ERTR7 (Col VI), pan-laminin (LM), TNC, and CD45 in the neck coengrafted OSCC/FRC tumors or OSCC tumors. Arrows indicate the tumor matrix tracks (TMTs). The CK8/18 IF images shown are also presented with their corresponding H&E staining in Appendix Fig. S5A. The LM/TNC co-stained panel in OSCC/FRC tumors represents a cropped region of the image shown uncropped in Fig EV5A, tumor #6. Scale bar, 200 µm. (**C**) Gene expression analysis (qRTPCR) for the indicated genes in the engrafted tumors displayed in (**A**). Mean ± SEM; Kruskal–Wallis test, $^*P < 0.05$. (**D**) Monitoring of tumor volume upon engraftment of OSCC cells (3 ×106) alone (orange, $N = 10$ mice) or OSCC cells combined with WT FRC cells (dark blue, $N = 10$ mice), or OSCC cells combined with FRC TNCKO cells (light blue, $N = 10$ mice), in a 5:1 ratio into the neck of C57Bl6 mice during the indicated time frame (days 1–18). Mean ± STDEV. Ordinary one-way ANOVA with $^*P < 0.05$, $^{**}P < 0.01$, $^{***}P < 0.005$. (**E**) Representative IF images for LN/TNC and GP38/TNC in the engrafted tumors displayed in (**D**). Arrows indicate the tumor matrix tracks (TMTs). Scale bars, 50 µm. The exact *P* values are listed in Appendix Table S5. Source data are available online for this figure.

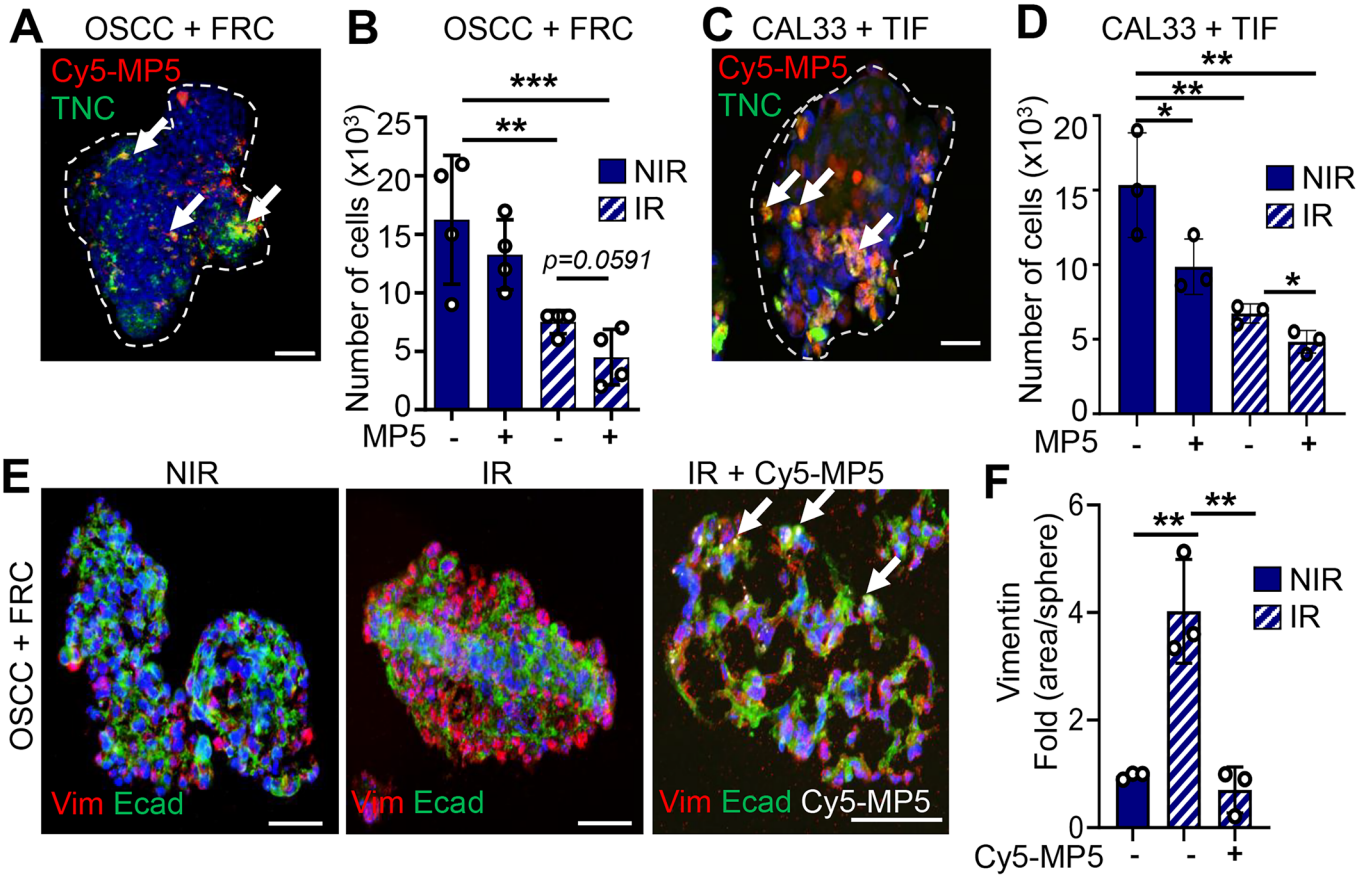

Figure 6. Targeting TNC with MAREMO peptide MP5 reduces tumor cell proliferation and plasticity upon IR.

After 7 days OSCC13 (OSCC)/FRC spheroid cocultures (2:1 ratio) (**A**, **B**, **E**, **F**) and CAL33/TIF spheroid cocultures (1:1 ratio) (**C**, **D**) cells were exposed to 10 Gy and subsequently MP5 (**B**, **D**) or Cy5-MP5 at 50 µg/ml each for another 3 days (**E**, **F**) before IF imaging for the indicated molecules (**A**, **C**, **E**), quantification of cells (**B**, **D**) and quantification of vimentin expression (**E**). Representative IF images ($N = 3$ experiments with 5–10 spheroids per condition) are shown for the indicated molecules. The white dotted line indicates the spheroid border. Arrows indicate colocalization of Cy5-MP5 with TNC. Individual fluorescence channels of (**A**) and the IR+Cy5-MP5 condition in (**E**) are shown separately in Appendix Fig. S6A,B. Scale bars, 50 µm. Ordinary one-way ANOVA test with $^*P < 0.05$, $^{**}P < 0.01$, $^{***}P < 0.005$. The exact *P* values are listed in Appendix Table S5. Source data are available online for this figure.

tumor remission by IR. Moreover, the MP5 effect is TNC-dependent.

Patients with irradiated HNSCC have a shorter survival when having FRCs highly expressing TNC

Since FRCs became more abundant following IR and played a critical role in promoting tumor proliferation, we hypothesized that they may serve as promising biomarkers for predicting survival in HNSCC patients. By using publicly available expression and survival data, we determined whether expression of a 9-gene signature comprising *CCL19*, *CCL21*, *TNC*, *VCAM1*, *PDPD*, *COL6A1*, *COL1A1*, *ACTA2*, and *LTBR* (Fletcher et al, 2015; Ferreira et al, 2021; Förster and Moschovakis, 2013; Spenlé et al, 2021), and downregulated in FRCs lacking TNC (Fig. 2C), is correlated with patients' overall survival (OS) in a total of 267 TCGA-HNSCC patients who had undergone radiotherapy. Individual gene expression did not correlate with survival. Given the key role of TNC in regulating FRCs, patients were initially stratified into TNC-high and TNC-low groups based on the median TNC expression. Each group was then further subdivided based on the median FRC signature expression into signature-high and signature-low subgroups. Kaplan–Meier survival analysis demonstrated a significantly lower median overall survival (OS) in the TNC-high group (P = 0.039, Fig. 7A). In contrast, the prognostic value of the FRC signature was reduced in patients with lower TNC expression ($P = 0.8$, Fig. 7B). In addition, Univariate Cox regression analysis identified T stage, N stage, and FRC signature expression as factors associated with OS, which were subsequently included in a multivariate Cox regression analysis. The Cox model revealed that higher FRC signature expression was an independent adverse factor for OS (HR = 1.863, 95% CI: 1.022–3.395, $P = 0.042$, Appendix Table S4). In summary, these findings suggest that an increased FRC signature expression is associated with a poorer prognosis in HNSCC patients who received RT, suggesting that tumor FRCs highly expressing TNC may represent a promising target to improve tumor eradication by radiotherapy.

In summary, our data demonstrate that while IR induces cell death in the majority of the tumor cells, it also increases the abundance of FCRs following an initial reduction in cell numbers.

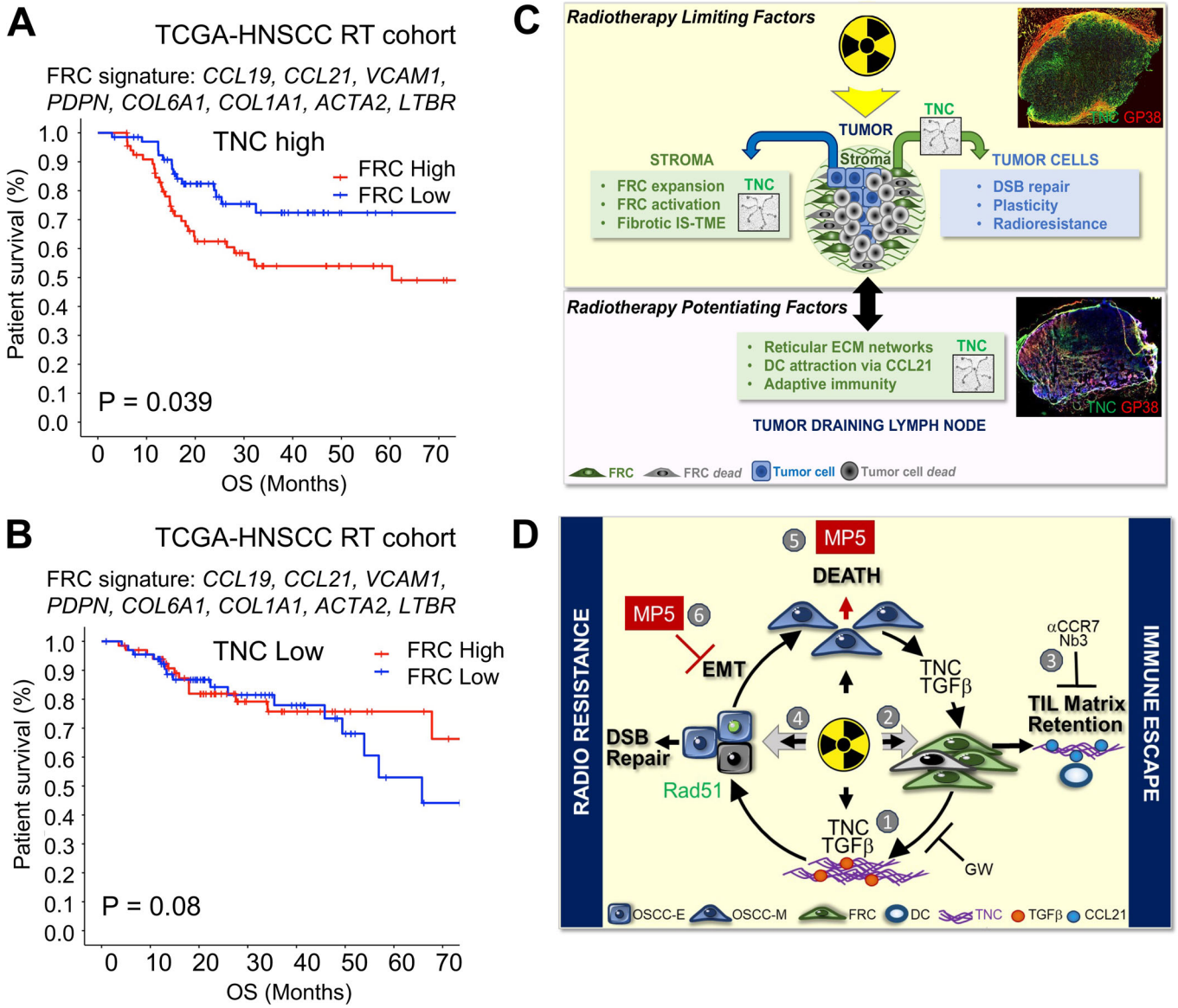

Crosstalk with tumor cells promotes FRC expansion and activation upon IR, leading to increased secretion of TNC, CCL21, and other molecules, thereby reinforcing an IS-TME that potentially protects the tumor cells from immune-mediated cell death. In parallel, crosstalk with the FRCs enforces plasticity and radioresistance in the surviving tumor cells (Fig. 7C). TNC plays a critical role in the tumors by facilitating EMT in the tumor cells and determines the FRC phenotype, which involves TGFβ signaling. While TNCKO FRCs demonstrate enhanced cellular radioresistance, this FRC survival does not seem directly to translate into tumor radioresistance. Instead, TNC-depleted FRCs fail to establish an IS-TME and to maintain functional TdLN-mediated adaptive immunity, thereby likely contributing to radioresistance. Last, FRCs generate TNC-containing reticular fibers and ECM networks and conduits regulating adaptive immunity (Song et al, 2023), and most importantly, express CCL21, as we have shown, involving TGFβ signaling induced by the irradiated tumor cells (Fig. 7D).

Discussion

This study identifies TNC as a central and context-dependent determinant of radiosensitivity in HNSCC, exerting distinct and even opposing effects in the tumor and in the TdLNs. Our findings reveal a dual and compartmentalized role: first, in the TdLNs, TNC provides essential baseline structural and immunoregulatory functions that are required for efficient IR-induced tumor regression, yet these functions seem independent of irradiation itself. Second, within the tumor, TNC instead contributes to the establishment of an IS-TME that undermines the therapeutic benefit of IR. In both settings, fibroblastic reticular cells (FRCs) emerge as key mediators of TNC biology. This duality reflects the compartmentalized nature of TNC and FRC functions. In the TdLNs, TNC supports the integrity of the reticular network, presumably allowing the spatial organization necessary for dendritic cell (DC)–T cell interactions and optimal priming. Such

Figure 7. HNSCC patient survival is correlated with high TNC and expression of the FRC signature.

(**A**, **B**) Kaplan–Meier analysis of a nine-gene FRC signature in tumors with levels of TNC above (**A**) or below the median (**B**). $N = 268$ patients with $n = 134$ TNC high and $n = 134$ TNC low levels. Kaplan–Meier survival curves were plotted by using R function. Multivariate Cox regression analysis is provided in Appendix Table S4. (**C**) Roles of TNC in modulating radiosensitvity: TNC plays a compartmentalized and dual role in regulating tumor radiosensitivity in HNSCC with distinct functions in the tumor (yellow background shading) opposed to the tumor-draining lymph nodes, TdLNs (purple background shading). In the tumor, ionizing irradiation (IR) induces massive cell death which launches an adaptive immune response involving the TdLNs, with activates immune cells returning into the tumor as indicated by a two-sided arrow. In HNSCC, the multiple tumor islets are surrounded by TNC-rich stroma where FRCs are a major producer of TNC (central cartoon showing one stroma-islet unit, image of a tumor stained for TNC (green) and GP38 (red) (upper right), original image in Appendix Fig. 5C)). In the tumor and TdLN compartments, FRCs (green box) are important, and their function is regulated by TNC. Surviving FRCs expand in the tumor stroma, which is linked to a cell-cell crosstalk (indicated by the blue arrow), where tumor cells activate FRCs to increase production of CCL21 and TNC. This amplifies the immunosuppressive tumor microenvironment (IS-TME) where TNC contributes to the generation of stromal tumor matrix tracks, TMT. In addition, the interaction with FRCs (indicated by the green arrow) promotes tumor cell survival and resistance involving DSB repair and plasticity/EMT, which is TNC-dependent (blue box). Conversely, in the TdLNs, FRCs organize the reticular ECM networks that regulate adaptive immunity, where TNC is important (image of a TdLN stained for TNC (green) and GP38 (red) (upper right), original image in Appendix Fig. 1Q). Here, FRC-derived CCL21 attracts DCs and immature CD8 + T cells, generally supporting anti-tumor immunity. Critically, our RNA profiling, flow cytometry, staining and quantification results suggest a role of TNC in the organization of the TdLNs, and in the regulation of the numbers of T and B cells and, DC and T-cell function. Altogether, an altered TdLN function may contribute to an impaired adaptive anti-tumor response and reduced radiotherapy efficacy in TNCKO mice. This dual role of TNC, detrimental in the tumor stroma (TNC expressed in TMTs) but essential in TdLNs (TNC expressed in the reticular networks), determines the overall radiotherapy outcome. Representative microscopy images previously shown in Appendix Figs. S1Q and S5B are used in this summary cartoon. (**D**) Impact of targeting TNC with a MAREMO peptide: cellular and molecular responses within the tumor compartment (yellow background) are illustrated in the presence of the MAREMO peptide MP5. In addition to blocking the tumor-promoting functions of TNC and counteracting immune evasion (Li et al, 2024), MP5 further enhances radiosensitivity, as demonstrated in this study. However, whether and how MP5 directly influences the TdLNs remains to be investigated. Whereas IR induces cell death in the majority of tumor cells and FRCs (gray shading), here we focus on the surviving FRCs, where IR triggers TNC and TGFβ expression, which form complexes known to potentiate TGFβ activity (Sun et al, 2019; Loustau et al, 2022) (1). This mechanism contributes to establishing an IS-TME that favors tumor regrowth. Crosstalk between surviving tumor cells and FRCs (two-sided gray arrow) promotes FRC activation through TGFβ signaling, resulting in increased secretion of TNC and CCL21. Collectively, these events reinforce an IS-TME where DCs become entrapped and functionally impaired by TNC (Loustau et al, 2022; Spenlé et al, 2020) (2). Analogous to CCR7 inhibition (Spenlé et al, 2020), blockade of TNC function in DCs using the TNC-specific nanobody Nb3 (Dhaouadi et al, 2021) abolishes the immunosuppressive DC-matrix-chemoretention effect enhanced by irradiation, further highlighting the central role of TNC (3). As described in Fig. 7C, TNC also regulates the interplay between OSCC tumor cells and FRCs, increasing tumor cell survival and radioresistance through induction of EMT (via TGFβ) and Rad51, in a TNC-dependent manner (4). Targeting TNC with the MAREMO peptide MP5 enhances tumor radio-responsiveness by promoting tumor cell death (5) and inhibiting irradiation-induced EMT (5). Together, these findings substantiate a pivotal role of TNC in radioresistance and identify its therapeutic targeting as a promising strategy to improve radiotherapy efficacy. Source data are available online for this figure.

roles align with a proposed evolutionary function of TNC in adaptive immunity and in the formation of immune-regulating stromal networks in the TdLNs, an idea supported by prior work (Orend and Tucker 2021; Spenlé et al, 2015; Panocha et al, 2025). In contrast, within the tumor, the same TNC–CCL21 axis presumed to promote immune cell positioning in lymphoid tissue is co-opted to retain CCR7+ immune populations in the stromal matrix, limiting their infiltration into tumor islets as already shown in OSCC tumors (Spenlé et al, 2020). A similar mechanism applies to CD8 + T cells, which are detained in TNC-rich stroma through a TNC–CXCL12 interaction (Loustau et al, 2022; Murdamoothoo et al, 2021) thereby reducing their cytotoxic impact. The net therapeutic outcome of IR therefore likely depends on the balance between TNC's immune-supporting functions in the TdLNs and its immune-restrictive activity in the TME, where IR enhances TGFβ, TNC, and CCL21 expression within the tumor, reinforcing a "sticky" IS-TME for DCs and T cells.

Several IR-activated pathways can mediate the IS-TME. Among them, TGFβ signaling is one of the most prominent regulators of radioresponse (reviewed in Farhood et al, 2020). As shown in this study, TGFβ signaling activation also occurs in the irradiated OSCC cells and FRCs. TGFβ signaling plays a key role as it activates and triggers the secretion of CCL21 in the irradiated FRCs and induces EMT in the OSCC. Our results also indicate that TGFβ signaling is regulated by TNC, playing multiple roles in the observed IR phenotype (Fig. 7D). We demonstrate that TGFβ signaling is specifically activated in TNC-expressing (but not TNC-depleted) FRCs and tumor cells upon IR, and that pharmacological inhibition of TGFβRI attenuates downstream responses. While the structural basis for this TNC-dependent TGFβ activation remains unclear, previous studies suggest that TNC may facilitate TGFβ signaling through direct binding within the FNIII domains (Loustau et al, 2022) and/or recruitment of latent TGFβ binding protein (Aubert et al, 2021), two mechanisms worthy of further investigation in the HNSCC context. Moreover, TNC-expressing FRCs promote EMT markers through TGFβ, which may also contribute to radioresistance (this study and Theys et al, 2011; Sun et al, 2019; Zhou et al, 2020).

High intratumoral CCL21 expression in TNC-expressing tumors upon IR may disrupt the normal chemokine gradient toward the TdLNs. As previously proposed (Spenlé et al, 2020), this local enrichment of CCL21 could impair the migration of primed APCs from the tumor to the TdLNs, thereby reducing the effectiveness of adaptive anti-tumor immunity. This mechanism may explain the observed paradox of increased leukocyte accumulation in the tumor yet reduced infiltration into the tumor islets. This mechanism also seems to apply upon IR, as evidenced by an increased accumulation of immature CCR7 + CD4 + T and Treg cells in the tumors of irradiated WT mice, an effect not observed in the TNCKO mice (Fig. 7C,D).

IR is well known to induce immunogenic cell death (ICD), which is important for tumor eradication (Golden and Apetoh, 2015; Lhuillier et al, 2019). IR-induced tumor regression in TNC-expressing hosts was accompanied by increased accumulation of CCR7+ leukocytes, including DCs, macrophages, and CD4 + T cells, though infiltration into tumor islets paradoxically decreased. This compartment-specific immune retention suggests that TNC-mediated stromal sequestration of immune cells *via* CCL21 (and CD8 + T cells *via* CXCL12) may impair direct anti-tumor activity despite heightened systemic immune response. The

interplay between IR-induced ICD, TGFβ-driven stromal remodeling, and TNC-mediated immune immobilization likely shapes this outcome, but the relative contributions of each remain to be fully dissected (Fig. 7C).

The minimal alteration in proliferation, gene, and protein expression which is in contrast to the TNC-expressing tumors that showed a strong reduction in proliferation upon IR and a high induction of an IR-response gene and protein expression signature further supports radioresistance of the TNC-depleted tumors. As FRCs are generating reticular fibers and conduits in the TdLNs and are impaired in producing several ECM and chemoattracting molecules in the absence of TNC, it is conceivable that this may impact the TdLN functions and contribute to the radioresistance phenotype in the TNCKO mice. Indeed, our gene expression data, tissue staining, and quantification of T and B cells suggest a strongly deregulated organization and immunity of the TNC-depleted TdLNs.

We discovered that the identified FRC signature correlates with shorter HNSCC patient survival, in particular when TNC levels are high, suggesting an important role of TNC-expressing FRCs in HNSCC. Although TNC-high FRCs represent a minority of cells within the tumor, their immunosuppressive effects are relevant, suggesting that tumor FRCs might be a promising target for anti-cancer therapy as recently proposed (Onder et al, 2024). However, direct FRCs and carcinoma-associated fibroblasts targeting has not yielded consistent benefits (reviewed in Zhang et al, 2023; Chen, McAndrews, and Kalluri, 2021, Onder et al, 2024), suggesting that some fibroblasts may possess anti-tumor functions that should be preserved. We propose that this also applies to the lymph node-derived FRCs that may remain in the HNSCC. We hypothesize that these FRCs initially fulfill an anti-tumor function, similar to what was seen in lung cancer, where FRCs generated a protective T-cell environment (Onder et al, 2024), but may undergo transformation into pro-tumorigenic cells, where high TNC expression contributes to the phenotype. Supporting this view, our co-engraftment experiments show that LN-derived FRCs markedly enforce IS-TME formation, and FRCs lacking TNC are significantly less capable of promoting tumor growth. We suggest that the depletion of pro-tumorigenic FRCs may reduce immune suppression and enforce IR-induced tumor eradication. Targeting TNC, which is highly expressed by the tumor FRCs, could be a promising therapeutic strategy. Supporting this hypothesis, we have recently demonstrated that targeting TNC with the MAREMO mimetic peptide MP5 (Loustau et al, 2022) induces depletion of FRCs among other fibroblasts and restores anti-tumor immunity (Li et al, 2024). Here, we show that MP5 combined with IR further reduces cell numbers and tumor cell plasticity, hallmarks of improved therapy response. Our study has limitations that should be acknowledged. While the 4NQO mouse model and human coculture systems provide mechanistic insights, validation in patient-derived xenografts, organoids, experimental tumors, and prospective clinical studies is required to fully establish the relevance of targeting TNC-dependent radioresistance in human HNSCC, also including HPV+ tumors. In addition, although TCGA analyses support a link between TNC-high FRCs and poor survival, causality must be confirmed experimentally. Finally, although we provide evidence that immunity in the TdLNs of TNC-depleted tumor mice is deregulated, which likely contributes to radioresistance, the underlying mechanism has to be worked out.

Collectively, our findings shed light on our understanding of the interactions between the tumor and its IR-modulated microenvironment, reveal compartmentalized roles of FRCs and TNC in the tumor and TdLN, and suggest the targeting of TNC in particular in tumor FRCs as a potential strategy to improve radioresistance overcomes in HNSCC, which may warrant investigation in other cancers.

Methods

Reagents and tools table

Reagent/resource	Reference or source	Identifier or catalog number
Experimental models		
C57BL/6J wild-type (WT) mice	Charles River	C57BL/6J
TNCKO mice on C57BL/6J background	Spenlé et al, 2020	N/A
OSCC13 cell line (4NQO-induced mouse tongue tumor)	Spenlé et al, 2021	N/A
Fibroblast reticular cells (FRCs) from mouse lymph nodes	This study and Spenlé et al, 2021	N/A
CAL33	Bozek et al, 2006	N/A
TIF	Gift from Dr J. Norman (Beatson Institute, Glasgow, UK)	N/A
DC2.4 dendritic cell line (mouse)	Merck	SCC142
TCGA-HNSC patient cohort	TCGA	TCGA-HNSC
Clinical data for TCGA-HNSC	UCSC Xena	xenabrowser.net
Recombinant DNA		
Lentiviral shRNA vector targeting TNC (shTNC)	Sigma	shTNC: CCGGGCATCAA-CACAACCAGTC-TAACTCGAGT-TAGACTGGTTG-TGTTGATGCTT-TTTG
Non-targeting shRNA lentiviral control (shC)	Sigma	SHC202V
Recombinant his-tagged human TNC FNIII 4–5 (TN 4-5)	Dr. Manuel Koch	N/A
Recombinant strep-tagged human fibronectin FNIII 4–6 (FN4-6)	Loustau et al, 2022	N/A
Antibodies		
Tenascin-C (TNC), mAb mTNC12 (1:100)	Homemade	N/A
Tenascin-C (TNC) (IF 1:200, WB 1:1000)	Merck/Millipore	AB19011
Ki67	Thermo Fisher	MA5-14520
Collagen VI/ERTR7 (1:200)	Santa Cruz	sc73355
CD11c	BD Biosciences	550275
Laminin Ln6 7 s (1:200)	Simo et al, 1992	N/A
CK8/18	Progen	GP11
CD31	BD Pharmingen	AB_39666

Reagent/resource	Reference or source	Identifier or catalog number
Podoplanin (gp38) (1:200)	Invitrogen	MA5-16113
CCL21	R&D Systems	AF457
Collagen XII (ColXII), clone Kr33	Dr M. Koch	N/A
Fibronectin	Sigma	F3648
Collagen IV, α2	Dr Arcangelis 1996	Col IV 2a
VCAM1	Merck/Millipore	CBL1300
Vimentin (1:50)	Santa Cruz	sc3260
E-cadherin (1:300)	Cell Signaling Technology	24E10, #3195
Integrin α7 (ITGA7) (1:100)	Bio-Techne	MAB3518
pSMAD3 (Ser423/Ser425) (1:200)	Rockland Immunochemicals	600-401-919S
Rad51 (1:100)	Calbiochem	PC130
CD3e (1:200)	BD Biosciences	550275
B220 (1:200)	Invitrogen	14-0452-82
GAPDH (1:2000)	Cell Signaling Technology	14C10, #2118
Anti-strep-tag antibody	Abcam	ab184224
Biotinylated secondary antibody	Vector Laboratories	PK-4001
ABC detection kit	Vector Laboratories	ABC system (used with PK-4001)
CD45-FITC	eBioscience/ Thermo Fisher	11-0454-85
CD11c-PE	eBioscience/ Thermo Fisher	12-0114-81
MHCII-APC-eFluor 780	eBioscience/ Thermo Fisher	47-5321-80
CCR7-PerCP-Cy5.5	eBioscience/ Thermo Fisher	45-1971-82
CK10-Alexa Fluor 700	Novus Biologicals	NBP2-34752AF700
CD31-FITC	eBioscience/ Thermo Fisher	11-0311-81
Podoplanin (gp38)-PE	eBioscience/ Thermo Fisher	12-5381-80
CD11b-Alexa Fluor 700	eBioscience/ Thermo Fisher	56-0112-80
F4/80-APC-eFluor 780	eBioscience/ Thermo Fisher	47-4801-82
CD3-PE	eBioscience/ Thermo Fisher	12-0031-81
CD4-APC-eFluor 780	eBioscience/ Thermo Fisher	47-0041-80
Foxp3-PE-Cy7	eBioscience/ Thermo Fisher	25-5773-80
CD80-Alexa Fluor 700	eBioscience/ Thermo Fisher	56-0801-82
CD86-PE-Cy7	eBioscience/ Thermo Fisher	25-0862-80
CD25-Alexa Fluor 700	eBioscience/ Thermo Fisher	56-0251-80
CCR7-neutralizing antibody	R&D Systems	MAB3477
GP38 (for MACS 1 µg/sample)	BioLegend	156202
Oligonucleotides and other sequence-based reagents		
MP5	Loustau et al, 2022	N/A
Cy5-MP5	Li et al, 2024	N/A
RT qPCR primers	Forward	Reverse
Ccl21	TCCAAGGGCTG-CAAGAGA	TGAAGTTCGTG-GGGGATCT
TGF beta	TGACGTCACTG-GAGTTGTACGG	GGTTCATGT-CATG-GATGGTGC
Cadh1	CAGCCTTCTTTT-CGGAAGACT	GGTAGA-CAGCTCCCTAT-GACTG
Vimentin	CCAACCTTTTCT-TCCCTGAAC	TTGAGTGGGTG-TCAACCAGA
Twist	AGTGTTTGG-CAGGGGACA	CCCATCCCCTG-GGTATCT
Tenascin-C (murine)	CAGGGATA-GACTGCTCT-GAGG	CATTGTCC-CATGCCA-GATTT
Acta2	TCCTATGTGGGT-GACGAGGC	TACATGGCTGG-GGTGTTGAA
Gp38	ACAACCA-CAGGTGC-TACTGGAG	GTTGCTGAGGT-GGACAGTTCCT
Col1a2	TTCTGTGGGTC-CTGCTGGGAAA	TTGTCACCTCG-GATGCCTTGAG
Ki67	GAGGA-GAAACGCCAAC-CAAGAG	TTTGTCCTCGG-TGGCGTTATCC
Itga7	TCTGTCAGAG-CAACCTCCAGCT	CTAT-GAACGGCTGCC-CACTCAA
Rad51	TGGAGGCTGTT-GCTTATGCACC	GCTGGTGAAA-CTCAGTTGCCG-T
Ccr7	CTCCTTGTCATT-TTCCAGGTG	TGGTATTCTCG-CCGATGTAGT
Il10	ATC-GATTTCTCCCCT-GTGAA	TGTCAAATT-CATT-CATGGCCT
Il17	Taqman probe: Mm00439618_m1, Thermofisher	
Chemicals, enzymes, and other reagents		
4-NQO	Sigma-Aldrich	N8141
Isoflurane (2%)	Minerve system	N/A
Ocrygel	Zooplus	N/A
RPMI-1640 medium	Dutcher	RPMI-1640
Dispase	Roche	04942078001
Collagenase P	Roche	11213857001

Reagent/resource	Reference or source	Identifier or catalog number
DNase I	Invitrogen	18068015
Fetal bovine serum (FBS)	Dutscher	S00AC3000C
DMEM high-glucose	Dutscher	L0102-500
DMEM/F12 (4.5 g/L glucose)	ThermoFisher	10565018
Penicillin-Streptomycin (PenStrep)	Dutscher	P06-07100
Gentamicin	ThermoFisher Scientific	15750060
Puromycin	ThermoFisher	J67236
Hydrocortisone	Sigma	H0888
Trypsin-EDTA	PanBiotech	P10-023100
Recombinant mouse TGFβ1	Bio-Techne	7666-MB
TGFβR inhibitor GW788388	Selleckchem	GW788388
TRIzol reagent	Invitrogen	12044977
MultiScribe reverse transcriptase	Applied Biosystems	10117254
Sybr Green Master Mix	ThermoFisher Scientific	4344463
Fast TaqMan Mix	ThermoFisher Scientific	4444557
Gapdh and Rpl19 TaqMan assays	Life Technologies	433764 T
Phosphatase inhibitor cocktail	Santa Cruz Biotechnology	sc-45045
Protease inhibitor cocktail	Roche	05892970001
Bradford assay	Bio-Rad	5000001
Laemmli buffer	Bio-Rad	1610737
Precast 4–20% SDS-PAGE gels	Bio-Rad	4561096
Nitrocellulose membranes	Bio-Rad	1620113
Blocking-Grade Blocker	Bio-Rad	1706404
Amersham ECL Western Blotting Detection Reagent	GE Healthcare	RPN2106
SuperSignal West Femto substrate	ThermoFisher Scientific	34095
6-Ckine (CCL21) ELISA kit	ThermoFisher Scientific	EMCCL21A
High-binding 96-well ELISA plates	SARSTEDT	82.1581.200
Carbonate buffer pH 10	Thermo Scientific	258605000
TMB ELISA substrate	SERVA Electrophoresis	37068.01
Stop reagent for TMB substrate	Sigma	S5814
PolyHEMA	Sigma	192066
B27 supplement	ThermoFisher	17504044
EGF	Biotechne	236-EG
DAPI	Sigma	D9542
Ascorbic acid	Sigma	APO456787373
hTNC-specific nanobody Nb3	Dhaouadi et al, 2021	N/A
Dynabeads	Invitrogen	11035
Accutase	Gibco	A111-5-1

Reagent/resource	Reference or source	Identifier or catalog number
DNase I (CDM)	Roche	4716728001
Eukitt mounting medium	EMS/Sigma	EMS Cat#15320; Eukitt solution
Software		
FlowJo	BD	FlowJo
ImageJ	NIH	ImageJ
Axiovision	Zeiss	Axiovision
SpectroFlo 3.1	Cytek Biosciences	SpectroFlo v3.1
FastQC	Babraham Institute	FastQC
STAR aligner	Dobin et al	STAR
Bowtie2	Langmead & Salzberg	Bowtie2
HTseq-count	HTSeq Python package	HTSeq
DESeq2	Bioconductor	DESeq2
PANTHER (v11)	PANTHER	PANTHER v11
REACTOME	REACTOME	REACTOME
MaxQuant (v1.6.14.0)	Max Planck Institute	MaxQuant v1.6.14.0
Andromeda search engine	MaxQuant package	Andromeda
Prostar (v1.18.6)	Wieczorek et al, 2017	Prostar v1.18.6
R (v4.4.1)	R Foundation	R 4.4.1
GSVA package	Bioconductor	GSVA
survival package	R/Bioconductor	survival
survminer package	R	survminer
GraphPad Prism (v9.1.1)	GraphPad Software	Prism 9.1.1
IBM SPSS Statistics (v30.0)	IBM	SPSS 30.0
Other		
X-ray irradiator	Siemens	Primus, 6 MeV
Gallios flow cytometer	Beckman Coulter	Gallios
MultiSkan EX plate reader	ThermoFisher	MultiSkan EX
Varioskan Lux microplate reader	ThermoFisher Scientific	Varioskan Lux
Zeiss Axio Imager Z2 microscope	Zeiss	Axio Imager Z2
AxioCam MRm camera	Zeiss	AxioCam MRm
Philips/FEI XL 30 FESEM	Philips/FEI	XL 30
Philips EM-410 electron microscope	Philips	EM-410
Leica ultramicrotome	Leica Biosystems	Ultramicrotome
AFM instrument ART-1	ARTIDIS AG	ART-1
Rectangular cantilevers	MikroMasch	HQ:CSC38 B
TPP culture dishes (34 mm)	TPP Techno Plastic Products AG	TPP 93040
Lab-Tek coverslips	ThermoScientific NUNC	154534

Reagent/resource	Reference or source	Identifier or catalog number
Ultra-low attachment plates	Various	Ultra-low attachment plates for spheroids
Polycarbonate transwells, 5 µm	Corning Costar	3421
SpectroFlo QC beads	Cytek Biosciences	QC beads
NextSeq500 system	Illumina	NextSeq 500/550 High Output Kit v2
Q-Exactive Plus Orbitrap mass spectrometer	Thermo Fisher Scientific	Q-Exactive Plus
nanoAcquity UPLC system	Waters	nanoAcquity
ACQUITY UPLC Peptide BEH C18 column	Waters	Peptide BEH C18
Symmetry C18 trap column	Waters	Symmetry C18

The 4NQO model and irradiation treatment of tumor-bearing mice

Sex as a biological variable was not considered, as mice of both sexes were used, and no differences between males and females were noticed. 4-NQO (Sigma-Aldrich, catalog number N8141) was administered to 8-week-old WT and TNCKO mice, which had been backcrossed with C57BL/6J mice (Charles River) for over 10 generations as previously described (Spenlé et al, 2020). The compound was delivered through drinking water at a final concentration of 100 µg/ml for 16 weeks (stock solution: 5 mg/ml in propylene glycol) (Spenlé et al, 2020). Following this treatment, the mice received a single 2 Gy dose of photon irradiation under anesthesia (isoflurane 2%, Minerve system). Irradiation was delivered using X-rays (Primus, 6 MeV, Siemens) at a dose rate of 200 UM/min. During the procedure, the mice having Ocrygel (Zooplus) protection on the eyes were positioned on a heated mat and beneath a lead shield (Xraystore), with only the tumor region (head) being exposed to the radiation. After irradiation, the animals were provided with regular water for 6 weeks prior to sacrifice. At the time of euthanasia, tongue and mandibular lymph nodes (TdLNs) were harvested for Fluorescence-Activated Cell Sorting (FACS) analysis, cryosectioning, and mRNA or protein extraction, as described below. Tumor incidence and organ appearance were evaluated during tissue collection. All procedures adhered to the ethical guidelines of INSERM and the ethical committee (Cremeas) and the French Ministries of Research and Agriculture (APAFIS#16463), complying with Directive 2010/63/EU for the protection of animals used in scientific research. Mice were housed in a conventional animal facility under a 12 h light/12 h dark cycle, at controlled temperature (22 ± 2 °C) and humidity (50–60%), with ad libitum access to food and water. Environmental enrichment was provided in the form of cotton nesting material, tunnels, and shelters. All animal protocols comply with the ARRIVE guidelines.

Orthotopic grafting of OSCC13 and FRC cells in the neck of C57BL/6 J mice

WT mice (male, 8 weeks of age) were grafted on the back of the neck with 1.5×10^6 OSCC13 cells also derived from a male mouse (Spenlé et al, 2021) alone or in combination with 0.3×10^6 WT FRCs in 150 µL PBS using an U-100 insulin syringe (BD Micro-Fine) with an endpoint of 15 weeks post engraftment. In a second series of engraftment 3×10^6 OSCC13 cells were grafted alone or together with 0.6×10^6 FRCs (WT or TNC KO) with an endpoint of 41 days. Tumors were detectable by palpation and tumor size measurement with a caliper was started 1 or 2 weeks upon engraftment. Mice were sacrificed for analysis when the ethical weight limit was reached, when the tumor length passed 1.5 cm or at the final date of the protocol. At the time of euthanasia, tumors were collected for cryosectioning and mRNA extraction, as described below.

Isolation of lymph node fibroblast reticular cells (FRC)

FRCs were isolated from the lymph nodes of male WT and TNCKO mice as previously published (Fletcher et al, 2015; Spenlé et al, 2020). Cervical, mandibular, brachial, axillary, popliteal, and inguinal lymph nodes from two WT and two TNCKO (10 weeks old) mice were dissected and placed in 5 mL of Roswell Park Memorial Institute Medium (RPMI-1640) (per isolate) on ice. After all lymph nodes were collected, RPMI-1640 was removed and replaced with 2 mL of freshly made enzyme mix composed of RPMI-1640 containing 0.8 mg/mL dispase (Roche), and 0.2 mg/mL collagenase P (Roche) and 0.1 mg/mL DNase I (Invitrogen). Tubes were incubated at 37 °C and 200 rpm shaking for 30 min. Under sterile condition, lymph nodes were very gently aspirated and expirated using a 1 mL pipette. The mixture was placed again at 37 °C and 200 rpm shaking for 10 min, and then centrifuged (300× *g*, 4 min, 4 °C). The supernatant (containing the enzyme mixture) was removed, and cell pellets were resuspended in ice-cold fresh isolation buffer (2% fetal bovine serum (FBS), 5 mM EDTA in sterile PBS). The resulting cell suspensions were filtered through a 70-µm and 40-µm cell strainer and then placed in 6 cm culture dishes containing complete Dulbecco's Modified Eagle's Medium (DMEM) (10% FBS, 1% PenStrep) for 24 h. The day after, floating cells corresponding to dead cells and leukocytes were removed by replacing the culture medium with fresh complete DMEM. The clearance of endothelial cells in the culture dish occurred over the following two weeks with culture of the cells in DMEM supplemented medium. The exclusive presence of fibroblasts was verified by immunofluorescent staining of the cells in LabTek slides as described below for podoplanin (gp38), collagen VI (ERTR7), and CD31.

Hematoxylin–eosin staining (HE)

Tissue sections (8 µm thick) embedded in OCT were first incubated in ddH_2O and then stained with hematoxylin (Surgipath) and eosin (Harris) following a standard protocol (Cardiff et al, 2014). After staining, sections were mounted using the Eukitt solution (Sigma).

Immunohistochemistry on OCT sections

Cryosections were rehydrated in 1× PBS for 10 min after encircling the tissue with a DakoPen. Endogenous peroxidase activity was blocked using 0.5% H_2O_2 in methanol (freshly prepared) for 30 min at room temperature (RT), followed by a 5-min wash in distilled water. Antigen retrieval was performed with ice-cold acetone for

30 min, then slides were equilibrated in distilled water and permeabilized with 0.1% Triton X-100 in PBS for 10 min. Sections were blocked with 5% normal goat serum (NGS) in PBS for 1 h at RT, followed by overnight incubation at 4 °C with anti-tenascin-C (TNC) antibody (Millipore, 1:100 in 5% NGS-PBS). The next day, slides were washed in PBS and incubated with a biotinylated secondary antibody (PK-4001, Vector Laboratories) for 1 h at RT. An avidin-biotin complex (ABC) solution was applied for 1 h, followed by DAB substrate (SK-4100, Vector Laboratories) for up to 10 min. Slides were then washed, counterstained with hematoxylin (30 s), rinsed, and dehydrated through graded ethanol and toluene. Coverslips were mounted with Eukitt (EMS, Cat#15320) and dried overnight.

Flow cytometry

Tongue tumors and cervical lymph nodes were finely chopped with a scalpel and digested in a solution containing 1 mg/mL collagenase D (Roche, catalog number 50-100-3282), 0.2 mg/mL DNase I (Roche, catalog number 4716728001), and 2% heat-inactivated FBS in RPMI medium. The digestion was performed at 37 °C for 2 h. After digestion, 92 µL of 54 mM EDTA was added, and the samples were vortexed at maximum speed for 30 s. Cell suspensions were filtered sequentially through 70-µm and 40-µm cell strainers and treated with flow cytometry buffer (PBS, 2% FBS, 1 mM EDTA). Cell counts were performed, and aliquots of 2×10^6 cells per lymph node sample or 1×10^6 cells per tumor sample were stained with Dead Viability Dye-eFluor 450 (Thermo Fisher, catalog number 65-0863-18) following the manufacturer's instructions. The cells were then incubated in a blocking solution containing 2% FcBlock CD16/CD32 (Thermo Fisher, catalog number 14-0161-85) in flow cytometry buffer for 15 min at 4 °C, followed by a 30-min incubation at 4 °C with a standard immunophenotyping antibody panel with solution 1: anti-CD45-FITC, anti-CD11c-PE, anti-B220-APC, anti-CD80-APC EF780, anti-CD86- PE Cy7 and anti-CCR7-Percp Cy5; solution 2: anti-CD45-FITC, anti-CD3e-PE, anti-C8a-APC, anti-CD4-APC EF780, anti-Foxp3-PE Cy7, anti-CCR7-Percp Cy5 and anti-CD25-AF700; solution 3: anti-CD45-FITC, anti-Gp38-PE, anti-CD31-APC, anti-F4/80-APC EF780, anti-CCR7-Percp Cy5 and anti-CD11b-AF700 (Reagents and Tools table). Data acquisition was performed using a Beckman Coulter Gallios flow cytometer, and subsequent adjustments and analyses were carried out with the FlowJo software.

RNA extraction and real-time quantitative PCR (qRTPCR)

Frozen tongue and neck tumors and cultured cells were lysed in TRIzol reagent (Invitrogen, catalog number 12044977) to extract total RNA. RNA quality was verified by measuring optical density at 260 nm (OD 260 nm). Complementary DNA (cDNA) was synthesized from 1000 µg of total RNA using random primers and Moloney murine leukemia virus reverse transcriptase (MultiScribe, Applied Biosystems, catalog number 10117254). The cDNA was then subjected to qRTPCR using an Mx3005P Real-Time PCR System (ThermoFisher Scientific). Reactions were performed in duplicate for all conditions using either Sybr Green Master Mix (ThermoFisher Scientific, catalog number 4344463) or Fast Taq-Man Mix (ThermoFisher Scientific, catalog number 4444557). Expression of Gapdh and Rpl19 mRNA (Life Technology, catalog number 433764T) was used as endogenous controls, and the comparative cycle threshold method (2^-ΔΔCt) was employed for analysis. Primer sequences are detailed in the Reagents and Tools Table.

Analysis of protein expression

Tissues or cell lysates were prepared in a lysis buffer containing 50 mM Tris-HCl (pH 7.6), 150 mM NaCl, 1% NP-40, 0.5% sodium deoxycholate, and 0.1% SDS, supplemented with a phosphatase inhibitor cocktail (Santa Cruz, catalog number sc-45045) and protease inhibitors (Roche, catalog number 05892970001). Protein concentration from tissue samples and conditioned media was measured using the Bradford assay (Bio-Rad, catalog number 5000001) following the manufacturer's protocol.

For protein separation, 30 µg of lysate was mixed with Laemmli buffer (Bio-Rad, catalog number 1610737) and loaded onto pre-casted 4–20% gradient gels (Bio-Rad, catalog number 4561096) for SDS-PAGE. Proteins were then transferred to nitrocellulose membranes (Bio-Rad, catalog number 1620113) using the Trans-Blot Turbo Transfer system (Bio-Rad). Membranes were blocked with 5% Blocking-Grade Blocker (Bio-Rad, catalog number 1706404) in PBS with 0.1% Tween20 and incubated with primary antibodies overnight at 4 °C, followed by secondary antibodies for 1 h at room temperature in 1.5% Blocking-Grade Blocker in 0.05% Tween20 PBS. Antibodies used are detailed in the Reagents and Tools table. Protein bands were visualized using Amersham ECL Western Blotting Detection Reagent (GE Healthcare, catalog number RPN2106) or SuperSignal West Femto Substrate (Thermo-Fisher, catalog number 34095). Expression levels of CCL21 were quantified using the 6-Ckine ELISA kit (ThermoFisher Scientific, catalog number EMCCL21A), following the manufacturer's instructions. Absorbance readings for samples and standards were obtained using a MultiSkan EX plate reader (ThermoFisher).

Cell culture, coculture, and exposure to irradiation

FRCs were cultured in DMEM high-glucose (Dutscher, L0102-500) supplemented with Fetal bovine serum (FBS, Dutcher) 10%, 100 U/mL penicillin, 100 µg/mL streptomycin (PenStrep, Dutscher), 40 U/mL Gentamicin (ThermoFisher Scientific). TNC silencing in FRCs was achieved using short hairpin RNA (shRNA)-mediated gene knockdown. Lentiviral particles carrying shRNA vectors targeting TNC (shTNC: CCGGGCATCAACACAACCAGTCTAACTC-GAGTTAGACTGGTTGTGTTGATGCTTTTTG) were obtained from Sigma and used for transduction. Lentiviral particles encoding a non-targeting shRNA vector (SHC202V, Sigma) served as a control. Transduced cells were selected using the standard culture medium supplemented with 10 µg/mL puromycin (ThermoFisher, J67236). The selection pressure was maintained throughout all in vitro experiments by the addition of puromycin. The OSCC13 cell line, derived from a primary 4NQO-induced tongue tumor of a male WT mouse (Spenlé et al, 2021), was cultured in DMEM-F12 containing 4.5 g/L glucose, FBS 10%, Penstrep, gentamicin, and 50 µg/mL hydrocortisone (Sigma). Cell identity was verified by marker expression and morphology. DC-like DC2.4 cells were obtained from Merck (SCC142) and maintained in DMEM high-glucose complemented with 10% FBS, PenStrep, Gentamicin, and

1× HEPES. DC2.4 cells were authenticated by the supplier. The human HNSCC CAL33 cells were established in the Antoine Lacassagne Cancer Centre (Bozec et al, 2006) and maintained in DMEM high glucose complemented with 10% FBS and PenStrep. Normal human skin fibroblasts (TIFs) immortalized with the telomerase reverse transcriptase (hTERT) gene were provided by J. Norman (Beatson Institute, Glasgow, UK) and maintained in DMEM high glucose, complemented with 20% FBS, 20 mM HEPES, and PenStrep, as previously reported (Gopal et al, 2017). Cells were routinely tested for mycoplasma (Venor GeM OneStep kit by Minerva Biolabs). All cell lines were cultured at 37 °C in a humidified atmosphere with 5% CO_2. Culture media were replenished every 2–3 days, and cells were subcultured at 80–90% confluency using trypsin-EDTA (PanBiotech, P10-023100). Prior to treatment or irradiation, cells were serum-starved overnight in medium containing 1% FBS. Cells received a single 2 Gy dose of photon irradiation. Cells were treated with 10 ng/mL recombinant mouse TGFβ1 (Biotechne, 7666-MB) for 24 h and 10 μM of TGFβR inhibitor (GW788388, Selleckchem) for 1 h or 24 h. Upon starvation, the conditioned medium (CM) of OSCC13 cells was collected, filtered at 0.22 μm, and stored at −80 °C for future use. FRCs were treated 24 h with filtered CM from OSCC13 and with purified mouse TNC (10 μg/mL) diluted with DMEM medium complemented with 1% FBS, penstrep, and gentamicin. Purified strep-tagged mouse TNC was obtained as previously described (Spenlé et al, 2020). For the establishment of the FACS/MACS sorting protocol, OSCC13 and FRCs were cocultivated at a ratio of 1:1 for 24 h in full medium. Cells were detached mechanically, concentrated by centrifugation, and separated by FACS sorting using the 5 Laser Aurora Full Spectrum Cell sorter (Cytek Biosciences) and the following antibody panel: anti-Gp38-PE, anti-CD29-PE Cy7, anti-ITGA7-APC, anti-FAP-PE CF594, anti-140b-APC EF780. Data were acquired with Sectroflo 3.1. Quality control measures were performed using SpectroFlo QC beads (Cytek Biosciences) prior to acquiring samples. For the irradiation coculture experiments, OSCC13 and FRC cells (shC, shTNC, or TNCKO) were cocultured in a 2:1 ratio in medium containing 50% OSCC13 medium without hydrocortisone and 50% FRC medium without puromycin, for 48 h. Then the cells were irradiated with 2 Gy or 10 Gy, and 48 h later the cells were collected and separated by the magnetic cell sorting (MACS) method.

Magnetic cell sorting (MACS)

Dynabeads (Invitrogen #11035) at 25 μl per condition were washed two times in isolation buffer (PBS, 0.1% BSA, 2 mM EDTA, pH 7.4). After the washes, the beads were resuspended in isolation buffer at the same initial volume of the Dynabeads and coated with 1.5 μg of antibodies against integrin α7β1 and GP38 per 25 μl of beads (Reagents and Tools table). The coated beads were incubated for 1 h at 4 °C with tilting and rotation. The cocultured cells were harvested using Accutase (GIBCO #A111-5-1), and the cell pellets were resuspended in 1 mL isolation buffer. The coated beads were washed three times with isolation buffer and after the final wash the cells were resuspended in 1 mL isolation buffer/25 μl initial volume. In all, 1 mL of beads was added to the cell suspensions and they were incubated for 2 h at 4 °C with tilting and rotation. After placing the tubes in the magnet for 5 min, the supernatant was collected, containing the OSCC13 cells (negative for integrin α7β1 and GP38). The remaining bead-bound cells were washed two times with isolation buffer and then collected in 2 mL isolation buffer. The cells were then pelleted and resuspended in Trizol reagent for RNA isolation.

3D (spheroid) cocultures and peptide treatments

OSCC13 and FRCs were cocultured at a 2:1 ratio and CAL33 with TIF at a 1:1 ratio in DMEM/F12 supplemented with B27 and EGF (20 ng/mL) for 7 days in ultra-low attachment plates pre-coated with polyHEMA (poly(2-hydroxyethyl methacrylate, Sigma #192066), as reported in (Shaw et al, 2012). PolyHEMA was prepared by dissolving 2 g of powder in 166 mL of 95% ethanol, followed by filtration. Plates were coated with the solution and dried in an incubator at 37 °C for 48 h prior to use. On day 7, spheroids were irradiated with 10 Gy. The following day, spheroids were treated with either MP5 peptide (50 μg/mL) or Cy5-MP5 (50 μg/mL) for 72 h. After treatment, MP5-treated spheroids were mechanically dissociated with a syringe for cell counting, while Cy5-MP5-treated spheroids were fixed in 4% paraformaldehyde for whole-mount immunofluorescence analysis. For the fractionated irradiation experiments, the OSCC/FRC spheroids were subjected to 5 consecutive days of 2 Gy irradiation, before fixation and immunofluorescence analysis.

Competitive ELISA

High-binding 96-well ELISA plates (SARSTEDT, Cat. No. 82.1581.200) were coated overnight at 4 °C, with 1 μg/ml of recombinant His-tagged TNC FNIII 4-5 (TN4-5) molecule (Loustau et al, 2022) in carbonate buffer pH 10 (Cat No: 258605000, Thermo Scientific). The non-coated surface was blocked with 5% skim milk in PBS for 1 h at 37 °C. Peptides MP5 or Cy5-MP5 at different concentrations (0–250 μg/mL) were added to the TN4-5 coated plate, which was immediately followed by the addition of the purified recombinant strep-tagged fibronectin FNIII 4-6 (FN4-6) molecule at 0.5 μg/ml in PBS/1%BSA/0.3% Tween20 and, incubated at 37 °C for 2 h. After 4 times washing with 1× PBS/0.05% Tween20 100 μl of an anti-strep-tag antibody (Abcam, ab184224) in a dilution of 1:2,000 (PBS/1%BSA/0.3% Tween20) was added to each well for 2 h at 37 °C. Wells were washed 4 times with 1× PBS/0.05% Tween20, and horseradish peroxidase (HRP)-conjugated secondary antibody (anti-mouse, 1:5000 dilution in PBS/1%BSA/0.3% Tween20) was added. After incubation for 1 h at 37 °C and washing in 1× PBS/0.05% Tween20, the bound HRP conjugate was detected by adding 100 μl of TMB ready-to-use ELISA substrate (SERVA electrophoresis, Ref 37068.01). The peroxidase reaction was stopped after 5 min by the addition of 50 μl stop solution 50 μl/well (Sigma, Stop reagent for TMB substrate, Ref S5814). Optical densities were measured at 450 nm using a microplate reader (Varioskan Lux Microplate reader, Thermo Fisher Scientific).

Chemoretention assay

Boyden chamber migration assays with DC2.4 cells were performed in 5 μm pore-sized polycarbonate membrane transwells (Corning Costar Co, catalog number 3421). The lower surface of the transwells were coated with purified TN1-5 (dissolved in 0.01%

Tween20 PBS at a final concentration of 1 µg/cm² and peptides MP5 or Cy5-MP5 (25 µM in PBS) were added and incubated overnight at 4 °C. The bottom chambers of the transwells were filled with 1% FBS RPMI containing mouse CCL21 (200 ng/ml 366-6C-025/CF, R&D Systems). Murine DC2.4 dendritic cells (Merck, SCC142) (5×10^4) cells in 1% FBS RPMI were placed on the top of the transwell chamber for 24 h at 37 °C in 5% CO_2. Cells on the lower side of the insert were fixed with 4% paraformaldehyde (PFA) and stained with 4',6-Diamidino-2-phenylindole (DAPI) before cell counting. Images were captured and analyzed using ImageJ software. Between 15 and 20 randomly taken images were analyzed per well.

Generation of cell-derived matrix (CDM)

CDM of FRCs was done as described for other cells (Rupp et al, 2016). Briefly, Lab-tek coverslips (ThermoScientific NUNC #154534), six-well or 24-well plates were coated with 1% gelatin for 60 min at 37 °C, followed by crosslinking with 1% glutaraldehyde for 20 min at room temperature. Next, the crosslinker was quenched with 1 M glycine for 30 min and gelatin-coated surfaces were incubated with DMEM complete medium before seeding 25,000 FRCs per cm². On day 2 and during the next 9 days, medium was changed every second day and replaced by medium supplemented with 50 µg/mL of ascorbic acid. On day 10, matrices were decellularized in 20 mM NH4OH, 0.5% Triton X-100 in PBS followed by 10 µM DNase I treatment (Roche, 4716728001).

Modified chemoretention assay on CDM

Boyden chamber assays with DC2.4 cells were performed using 5-µm pore-sized polycarbonate membrane transwells (Corning Costar Co, 3421). The surface of the lower chamber was pre-coated with CDM deposited by WT and TNCKO FRCs over 10 days as described above. Then the lower chamber was filled with DMEM containing mouse CCL21 (200 ng/ml, R&D Systems, 457-6C-025) either alone or supplemented with 500 nM of hTNC-specific nanobody Nb3, as previously described (Dhaouadi et al, 2021). To block DC2.4 chemotaxis toward CCL21, cells were pre-incubated for 6 h with a CCR7 neutralizing antibody (10 µg/mL, R&D Systems, MAB3477) diluted in 1% FBS complemented DMEM. DC2.4 (50,000 cells) suspended in 150 µl of 1% FBS complemented DMEM were placed into the upper chamber of the transwell system. After 5 h of migration, the surface of the lower chambers was fixed with 4% PFA, and cells were stained with DAPI and ECM for the indicated molecules. Images were captured and analyzed using ImageJ software. Between 12 and 16, randomly taken images were analyzed per well.

Immunofluorescence (IF)

Frozen tissue sections (8 µm, unfixed), CDM, or cells fixed with 4% paraformaldehyde were incubated at room temperature for 1 h with blocking serum (5% normal goat or donkey serum in PBS; Jackson ImmunoResearch, 005-000-121 and 017-000-121, respectively). Primary antibodies (detailed in the Reagents and Tools table) were then applied overnight. Bound antibodies were detected using secondary antibodies conjugated to Alexa 488, Cy3, or Cy5 specific for goat, rabbit, guinea pig, hamster, or rat primary antibodies. DAPI (Sigma, D9542) was used for nuclear staining. Sections were embedded in FluorSave Reagent (Calbiochem, 345789) and analyzed using a Zeiss Axio Imager Z2 microscope. Images were captured with an AxioCam MRm camera (Zeiss) and Axiovision software. Control sections were processed identically, except for the omission of the primary antibodies. Image acquisition settings (microscope, magnification, light intensity, and exposure time) were maintained constant within and across experiments. Immune cell quantification and positive Ki67 cells or P-Smad3 nuclei were analyzed using ImageJ software. At least three sections from four different tumors or mice were analyzed per condition. The number of immune cells was normalized to the total number of DAPI-positive nuclei.

Scanning electron microscopy

The cell ultrastructure of both non-irradiated and irradiated cell culture samples was analyzed by high-resolution SEM. Cell samples were treated as described above, then fixed with 2.5% glutaraldehyde in cacodylate buffer. Then cells were washed with cacodylate buffer and dehydrated with an ascending ethanol series. Carbon dioxide was used for critical point drying of the specimens, and absolute ethanol was used as an intermediate solvent. Samples were mounted on aluminum holders, sputtered with 30 nm palladium/gold, and examined in a Philips/FEI XL 30 field emission scanning electron microscope (FESEM) operated at 5 kV accelerating voltage.

Electron microscopy of tumor tissue

Frozen and cryopreserved tissue samples were first thawed and washed with distilled water. Tissue was then fixed in a solution containing 2% formaldehyde (v/v) and 0.25% glutaraldehyde (v/v) in 100 mM cacodylate buffer, pH 7.4, at 4 °C overnight. Following fixation, the samples were rinsed with PBS, dehydrated in ethanol up to 70%, and embedded in LR White embedding medium (London Resin Company, UK), and polymerized under UV light. Ultrathin sections were prepared using an ultramicrotome (Leica Biosystems), collected on copper grids, and stained negatively with 2% uranyl acetate (Sigma-Aldrich) for 15 min. Electron micrographs were captured at 60 kV using a Phillips EM-410 electron microscope and imaging plates (Ditabis, Pforzheim, Germany).

Atomic force microscopy

Frozen microscopy slides with 14 µm OSCC tumor tissue sections were prepared by using a glass cutter to fit into a 34-mm culture dish (TPP Techno Plastic Products AG, Trasadingen, Switzerland, TPP 93040). The selected sample slides were then affixed to the bottom of the dish using a two-component epoxy adhesive. The dish was filled with degassed and filtered PBS (pH 7.4, Gibco), and left in Custodiol (Dr. Franz Köhler Chemie GmbH, Bensheim, Germany) for 30 min at room temperature to thaw. Samples were gently washed to remove non-adherent cells and debris and refilled with degassed and filtered Custodiol. Rectangular Cantilevers (HQ:CSC38 B, MikroMasch) were used to map the stiffness of the OSCC sections. Each cantilever's spring constant was determined using the thermal tuning method and was $k = 0.05–0.1\ \mathrm{Nm}^{-1}$ (Sader et al, 1995). Deflection sensitivity was

measured in degassed and filtered Custodiol on an empty TPP culture dish to ensure accurate force measurements during AFM analysis (Plodinec et al, 2012). Measurements were performed using the ART-1 machine (ARTIDIS AG, Switzerland). OSCC sample dishes were mounted on the sample tray, and force-displacement curves were recorded to assess cell stiffness (elastic modulus, E) and cell-surface adhesion. A total of 30–40 maps were acquired, each containing 400 force curves within a 20 × 20 µm area, using a relative trigger force of 1.8 nN and an indentation speed of 16 µm/s. Maps were selected based on the device's built-in optical microscopy and compared with previously recorded confocal microscopy images of adjacent frozen sections to ensure accurate targeting of tumor regions. Forward and backward elastic moduli were calculated from force-displacement curves using the Oliver-Pharr model (Oliver and Pharr, 1992). Maps with more than 30% irregular force curves were excluded from the analysis. Force curves influenced by the underlying coverslip were distinguishable from those generated by the sample. Maps with over 30% of these stiff force curves were also excluded. For the remaining maps, a Gaussian function was fitted to determine the distribution values (mean forward elastic modulus [kPa] ± standard deviation). Overall means and standard deviations were then reported, summarizing all maps.

Gene expression analysis

RNA from WT and TNCKO FRCs (derived from two mice per group) or from the NIR or IR TdLNs of the 4NQO WT and TNC KO mice was extracted (in duplicate from different passages) using the RNeasy Mini Kit (Qiagen), and RNA integrity was assessed on an Agilent Bioanalyzer 2100 (Pico Kit, Agilent Technologies). RNA Sequencing libraries were constructed using the SMARTer® Stranded Total RNA-Seq Kit v2 - Pico Input Mammalian (TaKaRa) following the manufacturer's protocol. Libraries were pooled and sequenced in paired-end mode (2×75 bp) on a NextSeq500 system with the NextSeq 500/550 High Output Kit v2 (Illumina). Quality control for each sample was performed using the FastQC tool from the NGS Core Tools suite. Sequence reads were aligned to the reference genome using STAR and Bowtie2 aligners, with results output in BAM (Binary Alignment Map) format for subsequent raw read count extraction. Read counts were determined with HTseq-count, part of the HTSeq Python package, using default parameters to generate an abundance matrix. Differential expression analysis was conducted using the DESeq2 package within the Bioconductor framework. Genes were considered significantly upregulated or downregulated based on an adjusted *P* value threshold of <0.10 and a fold-change cutoff of >±0.8 (detailed in Appendix Table S2). Further functional analysis of deregulated genes was performed using the PANTHER version 11 and REACTOME software tools. To assess which FRC subclusters were represented in the model established in this study, the corresponding gene signatures of each cluster were used to evaluate enrichment through gene set variation analysis (GSVA). Specifically, based on the droplet-based single-cell RNA sequencing by (Rodda et al, 2018), there are nine peripheral stromal cell (SC) clusters in the lymph node, several of which were classified as FRC subclusters. Included are Ccl19 T-zone reticular cells (TRCs), marginal reticular cells, follicular dendritic cells (FDCs), and perivascular cells. The expression level of each gene set was normalized by z-score, and the Wilcox test was used to estimate the difference between the WT and TNC KO groups. Differential expression analysis of the TdLNs was performed on 12 samples using the limma package. Differentially expressed genes (DEGs) between non-irradiated TNCKO and WT samples were identified using a threshold of $|\log2FC| = 2.5$ and an adjusted *P* value = 0.05. Heatmaps and volcano plots of the DEGs were generated using the ggplot2 and ComplexHeatmap packages, respectively. Subsequently, the most significant enrichment pathways and biological processes of DEGs were investigated using the Gene Ontology (GO) analyses using the R software "clusterProfiler" package. See Appendix Table S1 for details.

Total RNA from MP5 and control NT193M cells, as well as from NT193 shC and shTNC cells, was extracted following the same procedure used for qRT-PCR and subsequently processed for RNA-seq, as previously described (Li et al, 2024 Murdamoothoo et al, 2021). Differential gene expression analyses were carried out using the DESeq2 package within the Bioconductor framework, applying internal normalization and shrinkage estimation for dispersion and fold-change calculations. Genes with nominal *P* values < 0.05 and false discovery rate (FDR) < 0.10 were considered significantly regulated. Principal component analysis (PCA) was performed on variance-stabilized read counts generated by DESeq2. For this analysis, we selected 7000 genes with the highest variance across all samples and detectable expression in every dataset, ensuring robust comparative clustering. The overall transcriptomic patterns referenced here correspond to datasets published in (Li et al, 2024) and Murdamoothoo et al (2021). Heatmaps illustrating gene expression patterns were generated using the Heatmapper online platform (https://heatmapper.ca/), applying default hierarchical clustering parameters.

NanoLC-MS/MS analysis

WT and TNCKO FRCs ($n = 5$ per genotype) were extracted in Laemmli-like buffer. Protein concentration was determined using the DC protein assay (Bio-Rad) following the manufacturer's protocol. For each sample, 15 µg of protein lysate was heated at 95 °C for 5 min. Proteins were loaded onto a 5% acrylamide SDS-PAGE stacking gel prepared in-house. Gel bands were reduced, alkylated, and digested overnight at 37 °C with modified porcine trypsin (Promega, Madison, USA) at an enzyme-to-protein ratio of 1:50. Extracted peptides were analyzed by nanoLC-MS/MS using a nanoAcquity UPLC system coupled to a Q-Exactive Plus Orbitrap mass spectrometer with a Nanospray Flex™ ion source. Peptides were separated on an ACQUITY UPLC® Peptide BEH C18 analytical column and a Symmetry® C18 trap column. A total of 800 ng of peptides was loaded onto the trap column and eluted with a gradient of acetonitrile in 0.1% formic acid at 400 nL/minute. The mass spectrometer was operated in Data-Dependent Acquisition (DDA) mode with automatic switching between MS and MS/MS. The ten most abundant ions with a charge state ≥2 were selected on each MS spectrum for further isolation and higher energy collision dissociation (HCD) fragmentation, excluding unassigned and monocharged ions. The dynamic exclusion time was set to 60 s. To avoid contamination between two successive samples, a "blank" sample without peptide was injected between each sample. NanoLC-MS/MS data were interpreted to do label-free extracted

ion chromatogram-based differential analysis using MaxQuant (version 1.6.14.0, Tyanova et al, 2016). Peaks were assigned with the Andromeda search engine against a custom mouse protein database (UniProtKB-SwissProt, Taxonomy ID: 10,090; 19-10-2020). MaxQuant parameters were set as follows: Maximum number of missed cleavages set to 1, Carbamidomethyl (C) set as fixed modification, Acetyl (Protein N-term) and Oxidation (M) set as variable modifications. False discovery rates (FDR) were estimated based on the number of hits after searching a reverse database and were set to 1% for both peptide spectrum matches and proteins. Protein quantification was performed using the LFQ intensities without "Match between runs". All other MaxQuant parameters were set as default. Differential analysis of normalized LFQ intensities was conducted using Prostar software (v1.18.6) applying a Limma *t* test (Wieczorek et al, 2017). The complete proteomics dataset has been deposited into the ProteomeXchange Consortium via the PRIDE partner repository with the dataset identifier PXD060164 (Perez-Riverol et al, 2022). Deregulated proteins (adjusted *P* value threshold of <0.05) were further analyzed via PANTHER and REACTOME. See Appendix Table S3 for details.

Patient survival analysis

Sex as a biological variable was not considered, as both men and women were included. Patient data were retrieved from the TCGA public database (TCGA-HNSC), and clinical data were obtained from the University of California Santa Cruz (UCSC) Xena platform (https://xenabrowser.net/) and analyzed using the R language. The cohort was stratified into "High" and "Low" expression groups based on the median expression level of the corresponding gene. Survival analysis was conducted specifically for HNSCC patients who had undergone radiotherapy (RT). Cox regression analysis was performed using the patient cohort TCGA-HNSCC. Analyses were performed using R version 4.4.1. The GSVA package was utilized to calculate the enrichment scores for each patient based on the FRC signature expression, which were then used to classify patients into high-FRC and low-FRC groups. Survival and Survminer packages were used to perform the Kaplan–Meier analysis. Cox regression analysis was conducted using IBM SPSS Statistics version 30.0. (Appendix Table S4).

Statistical analysis

For all datasets, the Gaussian distribution was assessed using the Shapiro-Wilk normality test. If the data followed a Gaussian distribution, statistical differences were evaluated using an unpaired *t* test (with Welch's correction for unequal variances), and one- or two-way ANOVA followed by Tukey's post-test. For non-Gaussian distributions, the Mann–Whitney test or Kruskal–Wallis with Dunn's post-test was employed to determine statistical significance. All analyses were conducted using GraphPad Prism software (version 9.1.1), and results are expressed as mean ± SEM or mean ± STDEV. Statistical significance was set at $P < 0.05$, with levels denoted as $^{*}P < 0.05$, $^{**}P < 0.01$, $^{***}P < 0.001$, $^{****}P < 0.0001$. The exact *P* values are listed on Appendix Table S5. No statistical methods were used to predetermine sample size. Sample sizes were chosen based on prior experience with similar experimental models and are reported in the figure legends. Animals and samples were allocated to experimental groups based on genotype and treatment; no additional randomization was applied. Investigators were blinded to group allocation during experiments or outcome assessment. No data were excluded from the analyses unless predefined technical issues occurred.

The paper explained

Problem

Ionizing radiation is the standard treatment for head and neck tumors and effectively reduces tumor burden. However, it simultaneously induces an immunosuppressive tumor microenvironment, particularly marked by increased expression of the tumor-promoting extracellular matrix glycoprotein tenascin-C (TNC). In this study, we sought to determine the specific contribution of TNC to tumor response following irradiation, using models with genetic or functional loss of TNC.

Results

Our work reveals that tenascin-C plays multiple regulatory roles in tumor radiosensitivity. In addition to directly influencing tumor cells, irradiation profoundly alters the phenotype of fibroblastic reticular cells (FRCs), a major source of TNC both within the tumor and in tumor-draining lymph nodes (TdLNs). Irradiation-surviving FRCs expand and acquire enhanced immunosuppressive properties, thereby promoting tumor progression. We demonstrate that physical interactions between tumor cells and FRCs drive FRC expansion and activation, increased tumor-cell survival and radioresistance, all in a TNC-dependent manner. Irradiation also remodels the TdLNs, where FRCs maintain the structural and functional networks required for adaptive immunity. In TNC-deficient tumor-bearing mice, TdLN immunity is deregulated, which likely contributes to the observed radioresistance.

Impact

TNC supports tumor regrowth after irradiation, in contrast to its protective role within the TdLNs, where TNC maintains immune-supportive functions. Our findings indicate that the balance between these opposing roles critically shapes radiotherapy outcomes. This identifies both FRCs and TNC as promising targets to enhance radiotherapeutic efficacy. Importantly, a high intratumoral abundance of highly TNC-expressing FRCs correlates with reduced survival in irradiated head and neck cancer patients. Finally, we demonstrate that therapeutic targeting of TNC using the MAREMO peptide increases tumor radiosensitivity, underscoring its clinical potential.

Data availability

Raw RNA-seq data are deposited at the EMBL-EBI ArrayExrpress archive (accession no E-MTAB-14801 and E-MTAB-16360. The complete proteomics dataset has been deposited into the ProteomeXchange Consortium via the PRIDE partner repository with the dataset identifier PXD060164. All other data are available in the main text or the supplementary information. The engineered cells are available upon request.

The source data of this paper are collected in the following database record: biostudies:S-SCDT-10_1038-S44321-026-00406-8.

Expanded view data, supplementary information, appendices are available for this paper at https://doi.org/10.1038/s44321-026-00406-8.

Peer review information

A peer review file is available at https://doi.org/10.1038/s44321-026-00406-8

References

Aubert A, Mercier-Gouy P, Aguero S, Berthier L, Liot S, Prigent L, Alcaraz LB, Verrier B, Terreux R, Moali C et al (2021) Latent TGF-β activation is a hallmark of the tenascin family. Front Immunol 12:613438

Batasheva S, Kotova S, Frolova A, Fakhrullin R (2024) Atomic force microscopy for characterization of decellularized extracellular matrix (dECM) based materials. Sci Technol Adv Mater 25:2421739

Bozec A, Lassalle S, Gugenheim J, Fischel J-L, Formento P, Hofman P, Milano G (2006) Enhanced tumour antiangiogenic effects when combining gefitinib with the antivascular agent ZD6126. Br J Cancer 95(6):722–728

Buchwald ZS, Nasti TH, Lee J, Eberhardt CS, Wieland A, Im SJ, Lawson D, Curran W, Ahmed R, Khan MK (2020) Tumor-draining lymph node is important for a robust abscopal effect stimulated by radiotherapy. J Immunother Cancer 8:e000867

Cardiff RD, Miller CH, Munn RJ (2014) Manual hematoxylin and eosin staining of mouse tissue sections. Cold Spring Harb Protoc 2014:655–658

Chen Y, McAndrews KM, Kalluri R (2021) Clinical and therapeutic relevance of cancer-associated fibroblasts. Nat Rev Clin Oncol 18:792–804

Chinn SB, Myers JN (2015) Oral cavity carcinoma: current management, controversies, and future directions. J Clin Oncol 33:3269–3276

Combs SE, Gutwein S, Thilmann Ch, Huber P, Debus J, Schulz-Ertner D (2005) Stereotactically guided fractionated re-irradiation in recurrent glioblastoma multiforme. J Neurooncol 74:167–171

Deligne C, Murdamoothoo D, Gammage AN, Gschwandtner M, Erne W, Loustau T, Marzeda AM, Carapito R, Paul N, Velázquez-Quesada I et al (2020) Matrix-targeting immunotherapy controls tumor growth and spread by switching macrophage phenotype. Cancer Immunol Res 8:368–382

Dhaouadi S, Ben Abderrazek R, Loustau T, Abou-Faycal C, Ksouri A, Erne W, Murdamoothoo D, Mörgelin M, Kungl A, Jung A et al (2021) Novel human tenascin-C function-blocking camel single domain nanobodies. Front Immunol 12:635166

Drumea-Mirancea M, Wessels JT, Müller CA, Essl M, Eble JA, Tolosa E, Koch M, Reinhardt DP, Sixt M, Sorokin L et al (2006) Characterization of a conduit system containing laminin-5 in the human thymus: a potential transport system for small molecules. J Cell Sci 119:1396–1405

Farhood B, Ashrafizadeh M, Khodamoradi E, Hoseini-Ghahfarokhi M, Afrashi S, Musa AE, Najafi M (2020) Targeting of cellular redox metabolism for mitigation of radiation injury. Life Sci 250:117570

Ferreira BO, Gamarra LF, Nucci MP, Oliveira FA, Rego GNA, Marti L (2021) LN-derived fibroblastic reticular cells and their impact on T cell response—a systematic review. Cells 10:1150

Fletcher AL, Acton SE, Knoblich K (2015) Lymph node fibroblastic reticular cells in health and disease. Nat Rev Immunol 15:350–361

Fonta CM, Loustau T, Li C, Poilil Surendran S, Hansen U, Murdamoothoo D, Benn MC, Velazquez-Quesada I, Carapito R, Orend G et al (2023) Infiltrating CD8+ T cells and M2 macrophages are retained in tumor matrix tracks enriched in low tension fibronectin fibers. Matrix Biol J Int Soc Matrix Biol 116:1–27

Förster R, Moschovakis GL (2013) Orchestrating the organizers: lymphotoxin-β receptor conducts fibroblastic reticular cell maturation. Immunity 38:851–853

Golden EB, Apetoh L (2015) Radiotherapy and immunogenic cell death. Semin Radiat Oncol 25:11–17

Gopal S, Veracini L, Grall D, Butori C, Schaub S, Audebert S, Camoin L, Baudelet E, Radwanska A, Beghelli-de La Forest Divonne S et al (2017) Fibronectin-guided migration of carcinoma collectives. Nat Commun 8:14105

Guo S, Yao Y, Tang Y, Xin Z, Wu D, Ni C, Huang J, Wei Q, Zhang T (2023) Radiation-induced tumor immune microenvironments and potential targets for combination therapy. Signal Transduct Target Ther 8:1–22

Huang Y, Mao K, Chen X, Sun M, Kawabe T, Li W, Usher N, Zhu J, Urban JF, Paul WE et al (2018) S1P-dependent interorgan trafficking of group 2 innate lymphoid cells supports host defense. Science 359:114–119

Jachetti E, Caputo S, Mazzoleni S, Brambillasca CS, Parigi SM, Grioni M, Piras IS, Restuccia U, Calcinotto A, Freschi M et al (2015) Tenascin-C protects cancer stem-like cells from immune surveillance by arresting T-cell activation. Cancer Res 75:2095–2108

Koukourakis MI, Giatromanolaki A (2022) Tumor draining lymph nodes, immune response, and radiotherapy: towards a revisal of therapeutic principles. Biochim Biophys Acta BBA - Rev Cancer 1877:188704

Lhuillier C, Rudqvist N-P, Elemento O, Formenti SC, Demaria S (2019) Radiation therapy and anti-tumor immunity: exposing immunogenic mutations to the immune system. Genome Med 11:40

Li C, Kaur A, Pavlidaki A, Spenlé C, Rajnpreht I, Donnadieu E, Salomé N, Molitor A, Carapito R, Wack F et al (2024) Targeting the MAtrix REgulating MOtif abolishes several hallmarks of cancer, triggering antitumor immunity. Proc Natl Acad Sci USA 121:e2404485121

Liu J, Burkin DJ, Kaufman SJ (2008) Increasing alpha 7 beta 1-integrin promotes muscle cell proliferation, adhesion, and resistance to apoptosis without changing gene expression. Am J Physiol Cell Physiol 294:C627–C640

Loustau T, Abou-Faycal C, Erne W, zur Wiesch PA, Ksouri A, Imhof T, Mörgelin M, Li C, Mathieu M, Salomé N et al (2022) Modulating tenascin-C functions by targeting the MAtrix REgulating MOtif, "MAREMO". Matrix Biol 108:20–38

Lüönd F, Sugiyama N, Bill R, Bornes L, Hager C, Tang F, Santacroce N, Beisel C, Ivanek R, Bürglin T et al (2021) Distinct contributions of partial and full EMT to breast cancer malignancy. Dev Cell 56:3203–3221.e11

Marsland BJ, Bättig P, Bauer M, Ruedl C, Lässing U, Beerli RR, Dietmeier K, Ivanova L, Pfister T, Vogt L et al (2005) CCL19 and CCL21 induce a potent proinflammatory differentiation program in licensed dendritic cells. Immunity 22:493–505

Massagué J (2008) TGFβ in cancer. Cell 134:215–230

Menon H, Ramapriyan R, Cushman TR, Verma V, Kim HH, Schoenhals JE, Atalar C, Selek U, Chun SG, Chang JY et al (2019) Role of radiation therapy in modulation of the tumor stroma and microenvironment. Front Immunol 10:193

Mottareale R, Frascogna C, La Verde G, Arrichiello C, Muto P, Netti PA, Fusco S, Panzetta V, Pugliese M (2024) Impact of ionizing radiation on cell-ECM mechanical crosstalk in breast cancer. Front Bioeng Biotechnol 12:1408789

Murdamoothoo D, Sun Z, Yilmaz A, Riegel G, Abou-Faycal C, Deligne C, Velazquez-Quesada I, Erne W, Nascimento M, Mörgelin M et al (2021) Tenascin-C immobilizes infiltrating T lymphocytes through CXCL12 promoting breast cancer progression. EMBO Mol Med 13:e13270

Nagira M, Imai T, Hieshima K, Kusuda J, Ridanpää M, Takagi S, Nishimura M, Kakizaki M, Nomiyama H, Yoshie O (1997) Molecular cloning of a novel human CC chemokine secondary lymphoid-tissue chemokine that is a potent chemoattractant for lymphocytes and mapped to chromosome 9p13. J Biol Chem 272:19518–19524

Nantajit D, Lin D, Li JJ (2015) The network of epithelial-mesenchymal transition: potential new targets for tumor resistance. J Cancer Res Clin Oncol 141:1697–1713

Oliver WC, Pharr GM (1992) An improved technique for determining hardness and elastic modulus using load and displacement sensing indentation experiments. J Mater Res 7:1564–1583

Omori K, Takada A, Toyomasu Y, Tawara I, Shintoku C, Imanaka-Yoshida K, Sakuma H, Nomoto Y (2024) Expression of tenascin-C is upregulated in the early stages of radiation pneumonitis/fibrosis in a novel mouse model. Curr Issues Mol Biol 46:9674–9685

Onder L, Papadopoulou C, Lütge A, Cheng H-W, Lütge M, Perez-Shibayama C, Gil-Cruz C, Martin AD, Kurz L, Cadosch N et al (2024) Fibroblastic reticular cells generate protective intratumoral T cell environments in lung cancer. Cell 188:430–446

Orend G, Tucker RP (2021) Did tenascin-C co-evolve with the general immune system of vertebrates?. Front Immunol 12:663902

Panocha D, Roet JEG, Kuipers JE, De Winde CM, Mebius RE (2025) Lymph node fibroblast-produced extracellular matrix shapes immune function. Trends Immunol 46:229–243

Perez-Riverol Y, Bai J, Bandla C, García-Seisdedos D, Hewapathirana S, Kamatchinathan S, Kundu DJ, Prakash A, Frericks-Zipper A, Eisenacher M et al (2022) The PRIDE database resources in 2022: a hub for mass spectrometry-based proteomics evidences. Nucleic Acids Res 50:D543–D552

Plodinec M, Loparic M, Monnier CA, Obermann EC, Zanetti-Dallenbach R, Oertle P, Hyotyla JT, Aebi U, Bentires-Alj M, Lim RYH et al (2012) The nanomechanical signature of breast cancer. Nat Nanotechnol 7:757–765

Rodda LB, Lu E, Bennett ML, Sokol CL, Wang X, Luther SA, Barres BA, Luster AD, Ye CJ, Cyster JG (2018) Single-cell RNA sequencing of lymph node stromal cells reveals niche-associated heterogeneity. Immunity 48:1014–1028.e6

Rupp T, Langlois B, Koczorowska MM, Radwanska A, Sun Z, Hussenet T, Lefebvre O, Murdamoothoo D, Arnold C, Klein A et al (2016) Tenascin-C orchestrates glioblastoma angiogenesis by modulation of pro- and anti-angiogenic signaling. Cell Rep 17:2607–2619

Sader JE, Larson I, Mulvaney P, White LR (1995) Method for the calibration of atomic force microscope cantilevers. Rev Sci Instrum 66:3789–3798

Shaw FL, Harrison H, Spence K, Ablett MP, Simões BM, Farnie G, Clarke RB (2012) A detailed mammosphere assay protocol for the quantification of breast stem cell activity. J Mammary Gland Biol Neoplasia 17:111–117

Shinohara A, Ogawa H, Ogawa T (1992) Rad51 protein involved in repair and recombination in *S. cerevisiae* is a RecA-like protein. Cell 69:457–470

Simo P, Bouziges F, Lissitzky J-C, Sorokin L, Kedinger M, Simon-Assmann P (1992) Dual and asynchronous deposition of laminin chains at the epithelial-mesenchymal interface in the gut. Gastroenterology 102(6):1835–1845

Song J, Deshpande T, Zhang X, Hannocks M-J, Lycke N, Cardell SL, Sorokin L (2023) The extracellular matrix of lymph node reticular fibers modulates follicle border interactions and germinal center formation. iScience 26:106753

Song WK, Wang W, Foster RF, Bielser DA, Kaufman SJ (1992) H36-alpha 7 is a novel integrin alpha chain that is developmentally regulated during skeletal myogenesis. J Cell Biol 117:643–657

Song WK, Wang W, Sato H, Bielser DA, Kaufman SJ (1993) Expression of α7 integrin cytoplasmic domains during skeletal muscle development: alternate forms, conformational change, and homologies with serine/threonine kinases and tyrosine phosphatases. J Cell Sci 106:1139–1152

Spenlé C, Gasser I, Saupe F, Janssen K-P, Arnold C, Klein A, van der Heyden M, Mutterer J, Neuville-Méchine A, Chenard M-P et al (2015) Spatial organization of the tenascin-C microenvironment in experimental and human cancer. Cell Adhes Migr 9:4–13

Spenlé C, Loustau T, Burckel H, Riegel G, Abou Faycal C, Li C, Yilmaz A, Petti L, Steinbach F, Ahowesso C et al (2021) Impact of tenascin-C on radiotherapy in a novel syngeneic oral squamous cell carcinoma model with spontaneous dissemination to the lymph nodes. Front Immunol 12:636108

Spenlé C, Loustau T, Murdamoothoo D, Erne W, Beghelli-de la Forest Divonne S, Veber R, Petti L, Bourdely P, Mörgelin M, Brauchle E-M et al (2020) Tenascin-C orchestrates an immune-suppressive tumor microenvironment in oral squamous cell carcinoma. Cancer Immunol Res 8:1122–1138

Sun Z, Velázquez-Quesada I, Murdamoothoo D, Ahowesso C, Yilmaz A, Spenlé C, Averous G, Erne W, Oberndorfer F, Oszwald A et al (2019) Tenascin-C increases lung metastasis by impacting blood vessel invasions. Matrix Biol J Int Soc Matrix Biol 83:26–47

Theys J, Jutten B, Habets R, Paesmans K, Groot AJ, Lambin P, Wouters BG, Lammering G, Vooijs M (2011) E-cadherin loss associated with EMT promotes radioresistance in human tumor cells. Radiother Oncol 99:392–397

Tomatis D, Echtermayer F, Schöber S, Balzac F, Retta SF, Silengo L, Tarone G (1999) The muscle-specific laminin receptor alpha7 beta1 integrin negatively regulates alpha5 beta1 fibronectin receptor function. Exp Cell Res 246:421–432

Toyomasu Y, Matsui K, Omori K, Takada A, Imanaka-Yoshida K, Tawara I, Shimamoto A, Takao M, Kobayashi H, Tomaru A et al (2022) Tenascin C in radiation-induced lung damage: pathological expression and serum level elevation. Thorac Cancer 13:2904–2907

Tyanova S, Temu T, Cox J (2016) The MaxQuant computational platform for mass spectrometry-based shotgun proteomics. Nat Protoc 11:2301–2319

Wang Z, Wu VH, Allevato MM, Gilardi M, He Y, Luis Callejas-Valera J, Vitale-Cross L, Martin D, Amornphimoltham P, Mcdermott J et al (2019) Syngeneic animal models of tobacco-associated oral cancer reveal the activity of in situ anti-CTLA-4. Nat Commun 10:5546

Wieczorek S, Combes F, Lazar C, Giai Gianetto Q, Gatto L, Dorffer A, Hesse A-M, Couté Y, Ferro M, Bruley C et al (2017) DAPAR & ProStaR: software to perform statistical analyses in quantitative discovery proteomics. Bioinformatics 33:135–136

Yilmaz A, Loustau T, Salomé N, Poilil Surendran S, Li C, Tucker RP, Izzi V, Lamba R, Koch M, Orend G (2022) Advances on the roles of tenascin-C in cancer. J Cell Sci 135:jcs260244

Zhang H, Yue X, Chen Z, Liu C, Wu W, Zhang N, Liu Z, Yang L, Jiang Q, Cheng Q et al (2023) Define cancer-associated fibroblasts (CAFs) in the tumor microenvironment: new opportunities in cancer immunotherapy and advances in clinical trials. Mol Cancer 22:159

Zhou S, Zhang M, Zhou C, Wang W, Yang H, Ye W (2020) The role of epithelial-mesenchymal transition in regulating radioresistance. Crit Rev Oncol Hematol 150:102961

Acknowledgements

We like to thank the staff of the animal facility and the staff of the GENOMAX facility for their assistance. Work in this article is supported by Worldwide Cancer Research (WCR) 24-0331/Association contre le cancer (ARC) (GN/HB and GO), Aviesan ITMO Cancer project Radio-3R (GN/HB and GO), INCa FITMANET (GN/HB and GO), and funding to GO: INSERM, INCa/Ligue contre le cancer LNCC ECMPACT, Ligue Régional contre le cancer Grand Est, and INCa PLBIO TENMAX.

Author contributions

Thomas Loustau: Conceptualization; Data curation; Formal analysis; Supervision; Investigation; Methodology; Writing—original draft; Writing—review and editing. **Ioanna Mitrentsi**: Conceptualization; Data curation; Formal analysis; Supervision; Investigation; Visualization; Methodology; Writing—original draft; Writing—review and editing. **Nuohan Wang**: Formal analysis; Investigation; Methodology. **Caroline Spenlé**: Conceptualization; Data curation; Formal analysis; Investigation; Visualization; Methodology. **Alexia Pavlidaki**: Data curation; Writing—review and editing. **Thibaud Tranchant**: Data curation; Formal analysis; Investigation; Methodology. **Gilles Riegel**: Formal analysis; Investigation; Methodology. **Akhil Venu**: Formal analysis; Investigation. **Rime Oueidat**: Investigation; Methodology. **Manuel Koch**: Resources. **Marion Dumas**: Formal analysis; Investigation; Methodology. **Fanny Wack**: Investigation. **Aurelie Hirschler**: Formal analysis; Investigation; Methodology. **Christine**

Carapito: Formal analysis; Supervision; Investigation. **Nicodème Paul**: Data curation; Formal analysis; Investigation; Methodology. **Raphael Carapito**: Supervision; Investigation; Methodology. **Matthias Mörgelin**: Formal analysis; Investigation; Methodology. **Uwe Hansen**: Formal analysis; Investigation. **Joyce Azzi**: Investigation; Methodology. **Lucie Aubergeon**: Investigation; Methodology. **Nathalie Salomé**: Supervision. **Sayda Dhaouadi**: Resources. **Pierre Grenot**: Investigation; Methodology. **Balkiss Bouhaouala-Zahar**: Resources; Supervision. **Simona La Cioppa**: Formal analysis; Investigation; Methodology. **Philipp Oertle**: Formal analysis; Supervision; Investigation; Methodology. **Valerio Izzi**: Data curation; Supervision. **Marija Plodinec**: Formal analysis; Supervision; Investigation; Methodology. **Georges Noel**: Supervision; Methodology. **Hélène Burckel**: Supervision; Methodology. **Gertraud Orend**: Conceptualization; Supervision; Funding acquisition; Writing—original draft; Project administration; Writing—review and editing.

Source data underlying figure panels in this paper may have individual authorship assigned. Where available, figure panel/source data authorship is listed in the following database record: biostudies:S-SCDT-10_1038-S44321-026-00406-8.

Disclosure and competing interests statement

Matthias Mörgelin is employed by Colzyx. Simona La Cioppa and Philippe Oertle are employed by Artidis. The remaining authors declare no competing interests.

Expanded View Figures

Figure EV1. Characterization of the 4NQO tumors and TdLNs after irradiation in WT and TNCKO mice.

(**A**) Cartoon summarizing the 4NQO protocol combined with a single dose of 2 Gy. (**B**) Quantification of tongue tumor number in NIR and IR WT and TNCKO mice, $N = 7$–10 mice per group. (**C**, **D**) Representative IF images (of at least 25) for the indicated molecules in IR 4NQO WT and TNCKO tumors (**C**) and NIR and IR WT and TNCKO tumors (**D**). White arrows indicate the CD11c+ cells either trapped in the stroma (**C**) or reaching the tumor nests (**D**). Scale bar, 50 μm (**C**), 200 μm (**D**). (**E**–**H**) FACS analysis in TdLNs (LN) of dendritic cells (**E**), CCR7 + DC (**F**) CD86/80 + DC (**G**), and Treg (**H**) in NIR and IR 4NQO-induced WT and TNCKO tumor mice. $N = 5$ mice per group. (**I**) Gene Ontology analysis of the most highly deregulated Biological Processes in the TdLNs of WT and TNCKO mice. Mean ± SEM; Kruskal–Wallis test and Dunn post-test, $^{*}P < 0.05$, $^{**}P < 0.01$, $^{***}P < 0.005$. The exact P values are listed in Appendix Table S5.

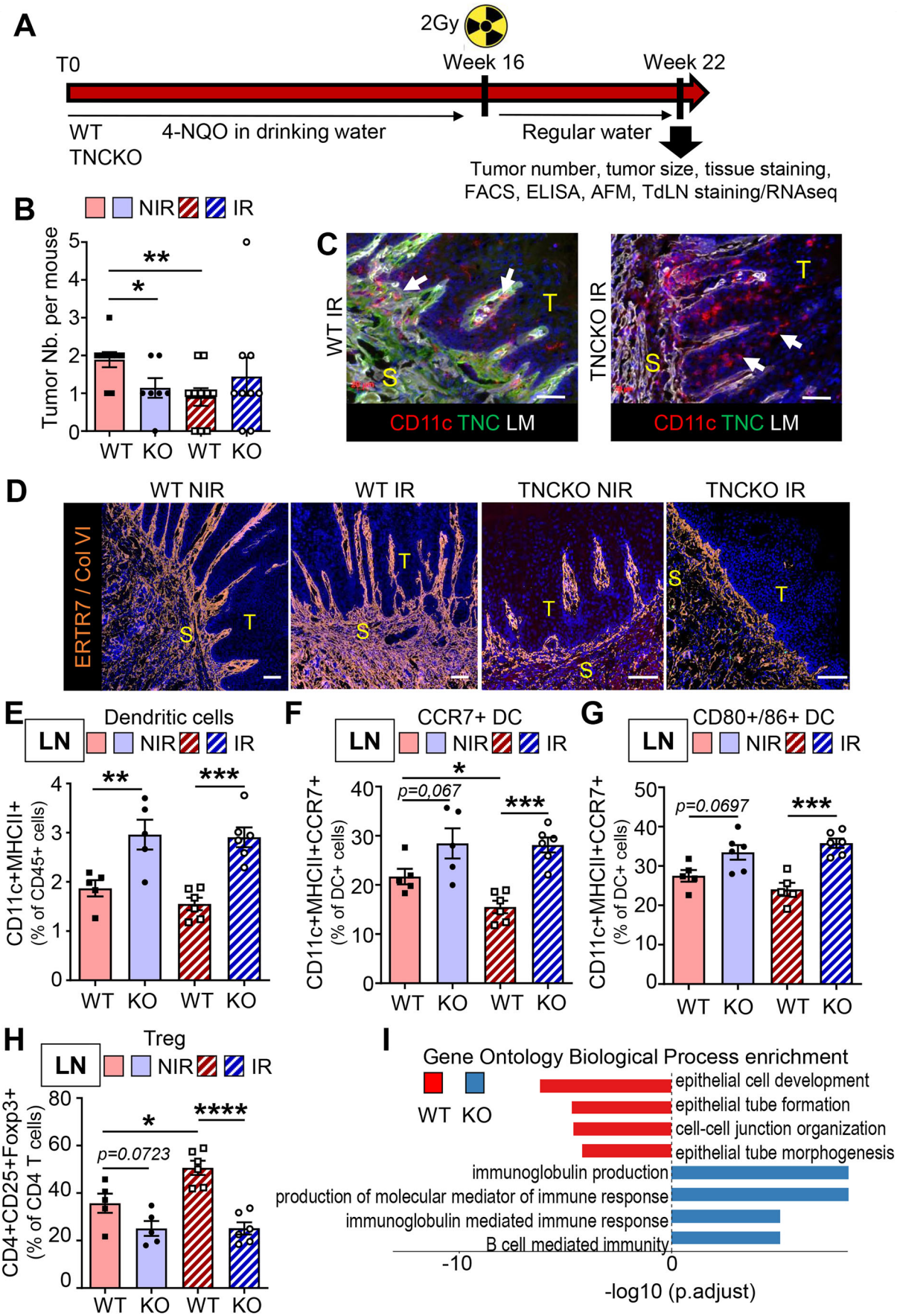
A
2Gy
T0
Week 16
Week 22
WT
TNCKO
4-NQO in drinking water
Regular water
Tumor number, tumor size, tissue staining,
FACS, ELISA, AFM, TdLN staining/RNAseq
B
NIR IR
Tumor Nb. per mouse
WT KO WT KO
C
WT IR
TNCKO IR
T
S
CD11c TNC LM
D
WT NIR
WT IR
TNCKO NIR
TNCKO IR
ERTR7 / Col VI
E
Dendritic cells
LN
CD11c+MHCII+
(% of CD45+ cells)
F
CCR7+ DC
CD11c+MHCII+CCR7+
(% of DC+ cells)
p=0,067
G
CD80+/86+ DC
p=0.0697
H
Treg
CD4+CD25+Foxp3+
(% of CD4 T cells)
p=0.0723
I
Gene Ontology Biological Process enrichment
epithelial cell development
epithelial tube formation
cell-cell junction organization
epithelial tube morphogenesis
immunoglobulin production
production of molecular mediator of immune response
immunoglobulin mediated immune response
B cell mediated immunity
-10
0
-log10 (p.adjust)

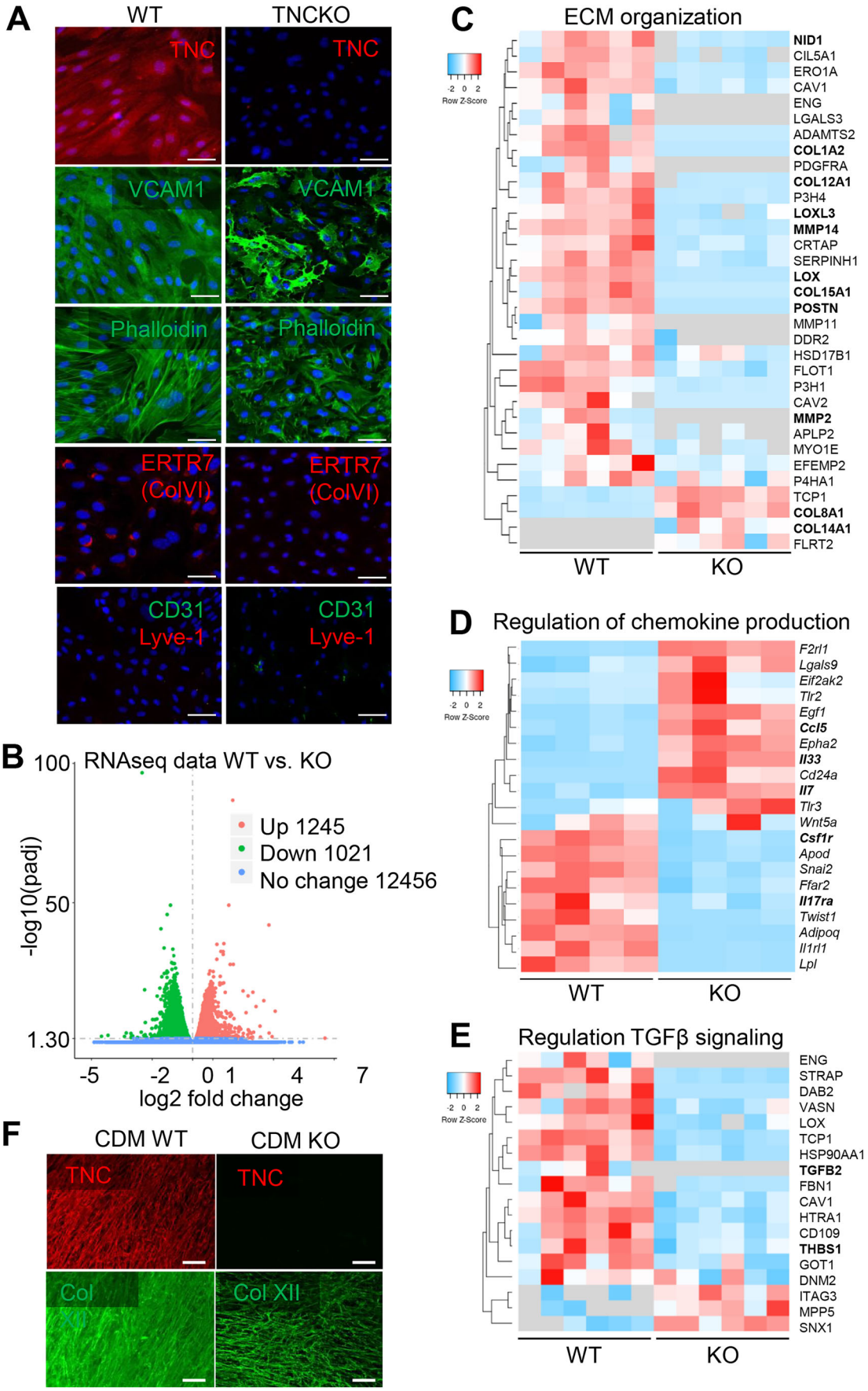
A
WT
TNCKO
TNC
VCAM1
Phalloidin
ERTR7 (ColVI)
CD31 Lyve-1
B
RNAseq data WT vs. KO
Up 1245
Down 1021
No change 12456
-log10(padj)
log2 fold change
C
ECM organization
Row Z-Score
NID1
CIL5A1
ERO1A
CAV1
ENG
LGALS3
ADAMTS2
COL1A2
PDGFRA
COL12A1
P3H4
LOXL3
MMP14
CRTAP
SERPINH1
LOX
COL15A1
POSTN
MMP11
DDR2
HSD17B1
FLOT1
P3H1
CAV2
MMP2
APLP2
MYO1E
EFEMP2
P4HA1
TCP1
COL8A1
COL14A1
FLRT2
WT
KO
D
Regulation of chemokine production
F2rl1
Lgals9
Eif2ak2
Tlr2
Egf1
Ccl5
Epha2
Il33
Cd24a
Il7
Tlr3
Wnt5a
Csf1r
Apod
Snai2
Ffar2
Il17ra
Twist1
Adipoq
Il1rl1
Lpl
E
Regulation TGFβ signaling
ENG
STRAP
DAB2
VASN
LOX
TCP1
HSP90AA1
TGFB2
FBN1
CAV1
HTRA1
CD109
THBS1
GOT1
DNM2
ITAG3
MPP5
SNX1
F
CDM WT
CDM KO
Col XII

◀ **Figure EV2. TNC expression plays a pivotal role in determining the FRC identity.**

(**A**) Representative IF images for TNC, VCAM-1, polymerized actin (phalloidin staining), collagen VI (ERTR7), CD31, and Lyve-1 in FRCs isolated from naïve lymph nodes of WT or TNCKO mice. For VCAM-1, the same microscopic field is shown that has been co-stained for GP38 in Fig. 2A. Scale bar, 50 μm. (**B**) Volcano plot of deregulated genes (DEGs) obtained after RNA sequencing of FRC WT and TNCKO cells. Volcano plot showing the fold change and the adjusted *P* value for the 14,722 genes expressed with overexpression (red dots) and downregulation (green dots) in FRC WT compared to TNCKO cells. (**C–E**) Proteomics data analysis represented as heatmaps for the most deregulated proteins that belong to ECM organization (**C**), Regulation of chemokine production (**D**), and regulation of the TGFβ signaling (**E**). Bold text indicates proteins with established roles in the respective categories that are discussed in the text. (**F**) Representative IF staining images of Col XII and TNC expression in the CDM obtained after 10 days of FRC WT and TNCKO cell cultures. Scale bar, 200 μm.

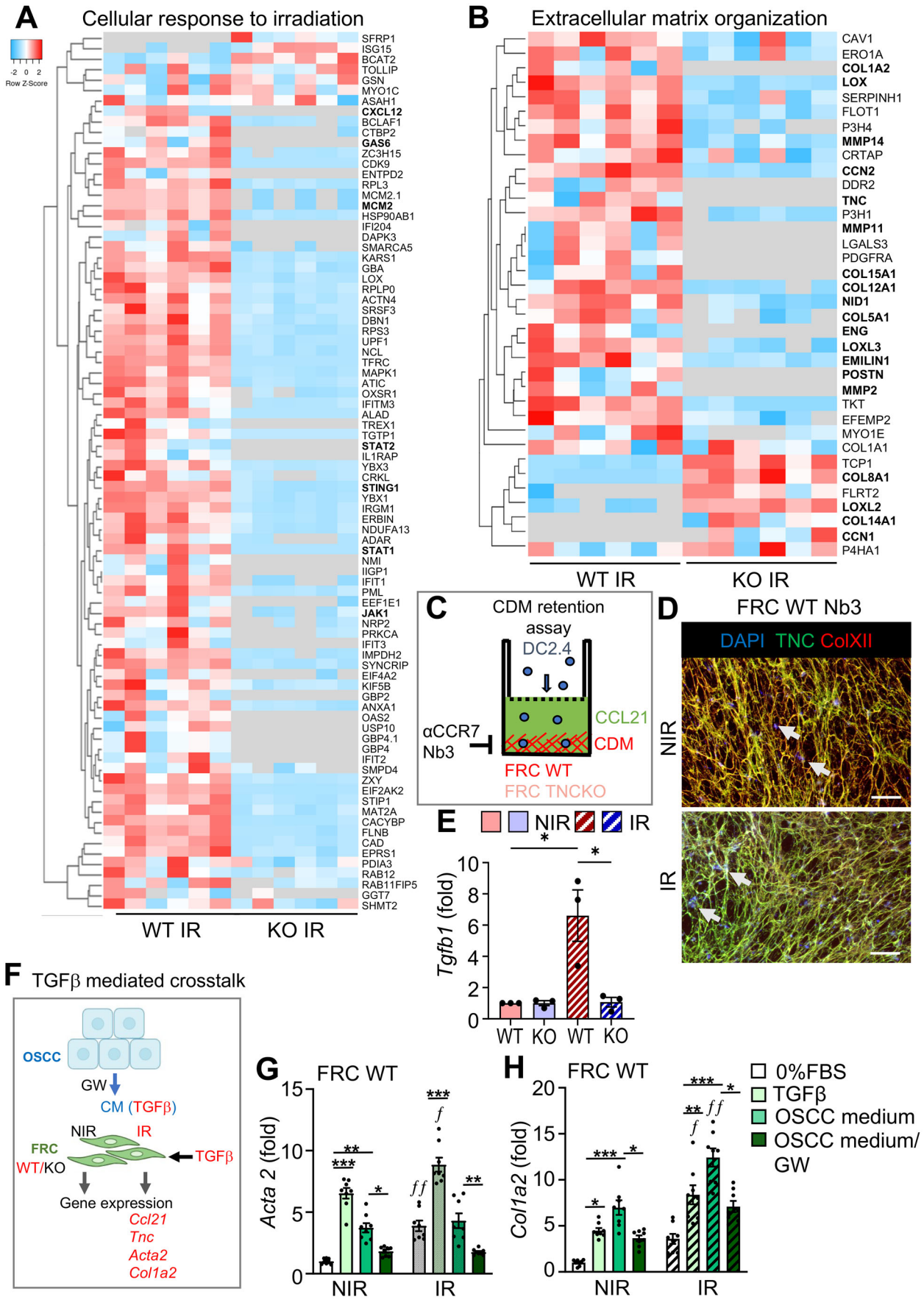
A
Cellular response to irradiation
Row Z-Score
SFRP1
ISG15
BCAT2
TOLLIP
GSN
MYO1C
ASAH1
CXCL12
BCLAF1
CTBP2
GAS6
ZC3H15
CDK9
ENTPD2
RPL3
MCM2.1
MCM2
HSP90AB1
IFI204
DAPK3
SMARCA5
KARS1
GBA
LOX
RPLP0
ACTN4
SRSF3
DBN1
RPS3
UPF1
NCL
TFRC
MAPK1
ATIC
OXSR1
IFITM3
ALAD
TREX1
TGTP1
STAT2
IL1RAP
YBX3
CRKL
STING1
YBX1
IRGM1
ERBIN
NDUFA13
ADAR
STAT1
NMI
IIGP1
IFIT1
PML
EEF1E1
JAK1
NRP2
PRKCA
IFIT3
IMPDH2
SYNCRIP
EIF4A2
KIF5B
GBP2
ANXA1
OAS2
USP10
GBP4.1
GBP4
IFIT2
SMPD4
ZXY
EIF2AK2
STIP1
MAT2A
CACYBP
FLNB
CAD
EPRS1
PDIA3
RAB12
RAB11FIP5
GGT7
SHMT2
WT IR
KO IR
B
Extracellular matrix organization
CAV1
ERO1A
COL1A2
LOX
SERPINH1
FLOT1
P3H4
MMP14
CRTAP
CCN2
DDR2
TNC
P3H1
MMP11
LGALS3
PDGFRA
COL15A1
COL12A1
NID1
COL5A1
ENG
LOXL3
EMILIN1
POSTN
MMP2
TKT
EFEMP2
MYO1E
COL1A1
TCP1
COL8A1
FLRT2
LOXL2
COL14A1
CCN1
P4HA1
WT IR
KO IR
C
CDM retention assay
DC2.4
CCL21
αCCR7 Nb3
CDM
FRC WT
FRC TNCKO
D
FRC WT Nb3
DAPI TNC ColXII
NIR
IR
E
NIR
IR
Tgfb1 (fold)
WT KO WT KO
F
TGFβ mediated crosstalk
OSCC
GW
CM (TGFβ)
NIR
IR
FRC WT/KO
TGFβ
Gene expression
Ccl21
Tnc
Acta2
Col1a2
G
FRC WT
Acta 2 (fold)
NIR
IR
H
FRC WT
Col1a2 (fold)
NIR
IR
0%FBS
TGFβ
OSCC medium
OSCC medium/ GW

◀ **Figure EV3. The FRC cell response to irradiation is determined by TNC expression.**

(**A**, **B**) Heatmap representation of the indicated proteome categories of irradiated FRCs (WT vs. TNCKO), represented as heatmaps for deregulated proteins involved in the cellular response to irradiation (**A**) and ECM organization (**B**). Bold text indicates proteins with established roles in the respective categories and/or that are discussed in the text. (**C**) Schematic representation of the DC retention assay with CCL21 (200 ng/ml) as chemoattractant and anti-CCR7 and Nb3 as TNC inhibitors. Note the less binding of cells to the CDM from TNCKO FRCs (light red) and upon inhibition of TNC. (**D**) Representative IF images of DC2.4 adherent on the CDM after the chemoretention assay in the presence of Nb3. Staining is as indicated. Arrows indicate the nuclei. Scale bar, 200 µm. (**E**) Gene expression (qRTPCR) of *Tgfb1* in WT and TNCKO FRCs, NIR or IR. $N = 3$. Mean ± SD, two-way ANOVA with $^{*}P < 0.05$. (**F**) Schematic representation of the experimental setup to assess a TGFβ-mediated cellular crosstalk between OSCC13 cells (OSCC) providing Conditioned Medium (CM) that was added to FRCs (WT, KO, NIR, IR) in the presence or absence of GW788388 (GW) in comparison to TGFβ (10 ng/ml). Gene expression of the indicated molecules was assessed by qRTPCR. Note a significant stimulating effect of the CM of the OSCC13 cells on irradiated WT FRCs in a TGFβ signaling depenndent manner (red). (**G**, **H**) Gene expression as determined by qRTPCR in FRC WT for *Acta2* and *Col1a2*. $N = 6$–9 per condition. Error bars represent mean ± SEM, two-way ANOVA with $^{*}P < 0.05$, $^{**}P < 0.01$, $^{***}P < 0.005$. The exact *P* values are listed in Appendix Table S5.

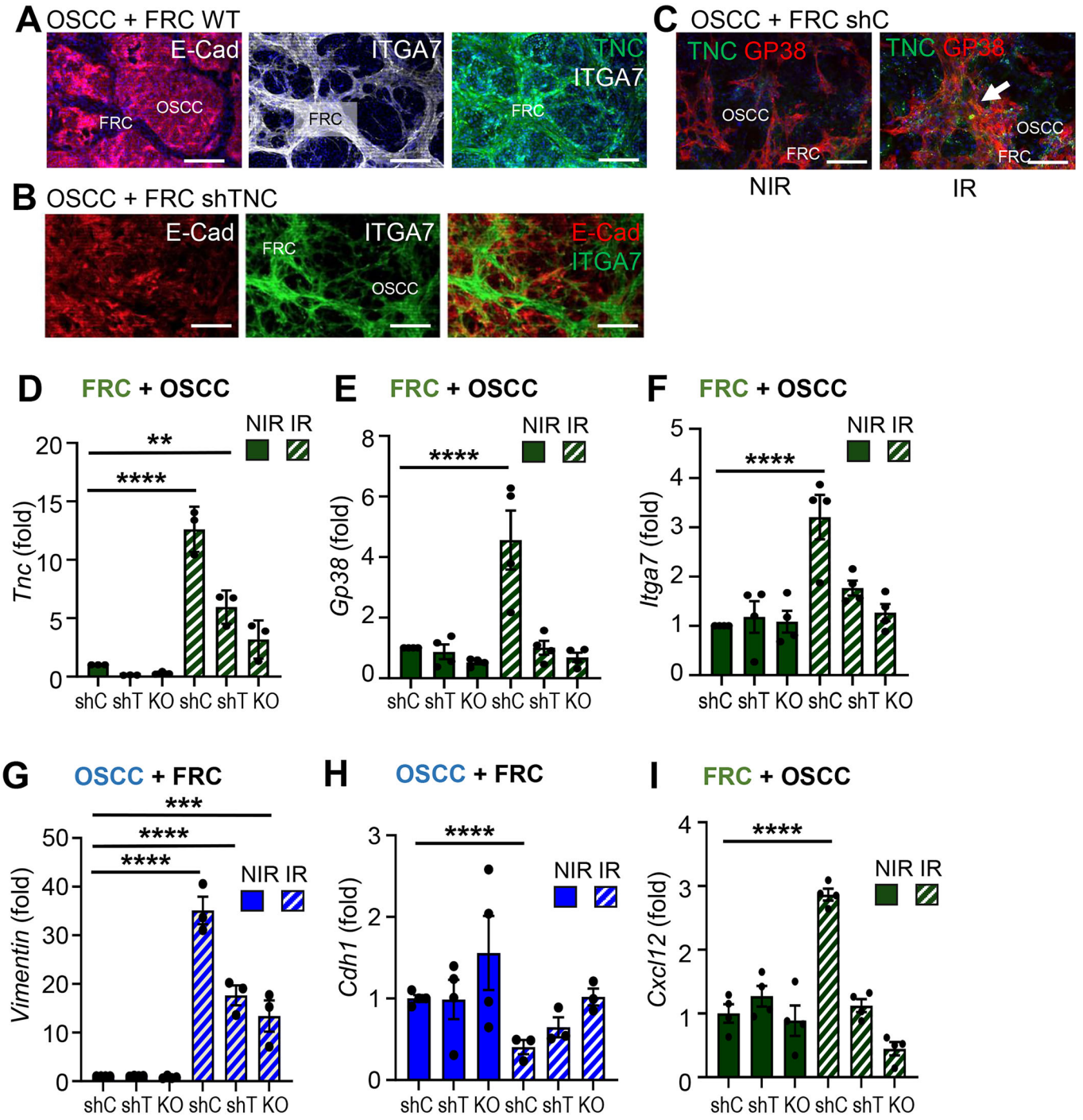

Figure EV4. TNC impact on the OSCC-FRC crosstalk upon irradiation.

(**A–C**) Immunofluorescence images after staining for the indicated molecules in cocultures of OSCC13 (OSCC) with FRCs at a 2.1 ratio for 4 days. FRCs and OSCC are labeled. Arrow points at increased GP38 and TNC levels in the IR condition (**C**). Scale bars, 200 µm. (**D–I**) Gene expression (qRTPCR) in FRCs (WT, shTNC (shT), TNCKO (KO)) (**D–F, I**) or OSCC13 (OSCC) (**G, H**) upon coculture, IR or NIR, and isolation by MACS for the indicated molecules. $N = 3$ experiments; Error bars represent mean ± SEM; ordinary one-way ANOVA test, ***$P < 0.005$. ****$P < 0.0001$. The exact P values are listed in Appendix Table S5.

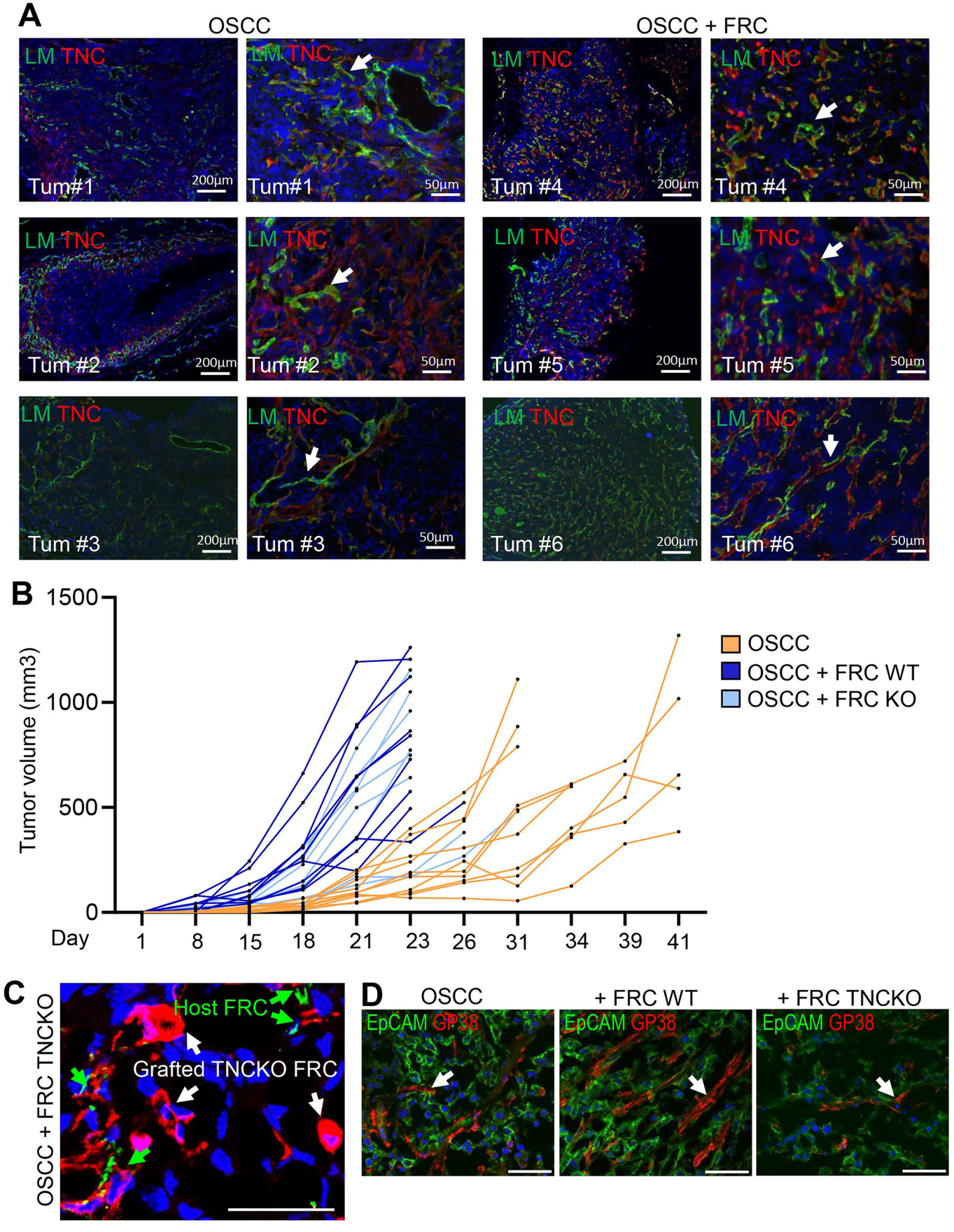
A
OSCC
OSCC + FRC
LM TNC
Tum#1
Tum #2
Tum #3
Tum #4
Tum #5
Tum #6
200µm
50µm
B
Tumor volume (mm3)
1500
1000
500
0
Day
1
8
15
18
21
23
26
31
34
39
41
OSCC
OSCC + FRC WT
OSCC + FRC KO
C
OSCC + FRC TNCKO
Host FRC
Grafted TNCKO FRC
D
OSCC
+ FRC WT
+ FRC TNCKO
EpCAM GP38

Figure EV5. Characterization of neck coengrafted tumors in C57Bl6 mice.

(**A**) Representative IF images of neck tumors displayed in Fig. 5A, obtained after OSCC grafting (3×10^6 cells) or OSCC/FRC (5:1 ratio) co-graftments in WT mice for the indicated markers. The LM/TNC costained panel of the OSCC/FRC tumor #6 represents an uncropped version of the image shown in Fig. 5B. Scale bar, 200 µm. (**B**) Monitoring of individual tumor growth (volume) of the engrafted OSCC13 (OSCC) cells alone (3×10^6 cells) (orange) or combined with WT FRC (dark blue), or FRC TNCKO cells (light blue), in a 5:1 ratio, into the neck of WT mice during the indicated time frame (up to 41 days). (**C**) Enlarged image showing FRCs (GP38 +) in a OSCC/TNCKO FRC-engrafted tumor where the engrafted FRCs are negative for TNC while the host FRCs are positive as indicated with the colored arrows. Scale bar, 50 µm. (**D**) Representative immunofluorescence images for EpCAM and GP38 in the tumors displayed in Fig. 5D derived from engraftments of the OSCC cells alone (3×10^6 cells) (orange) or in combination with WT FRC (dark blue), or FRC TNCKO cells (light blue), in a 5:1 ratio, into the neck of WT mice during the indicated time frame (up to 41 days). Scale bars, 50 µm. Arrow points at FRCs.

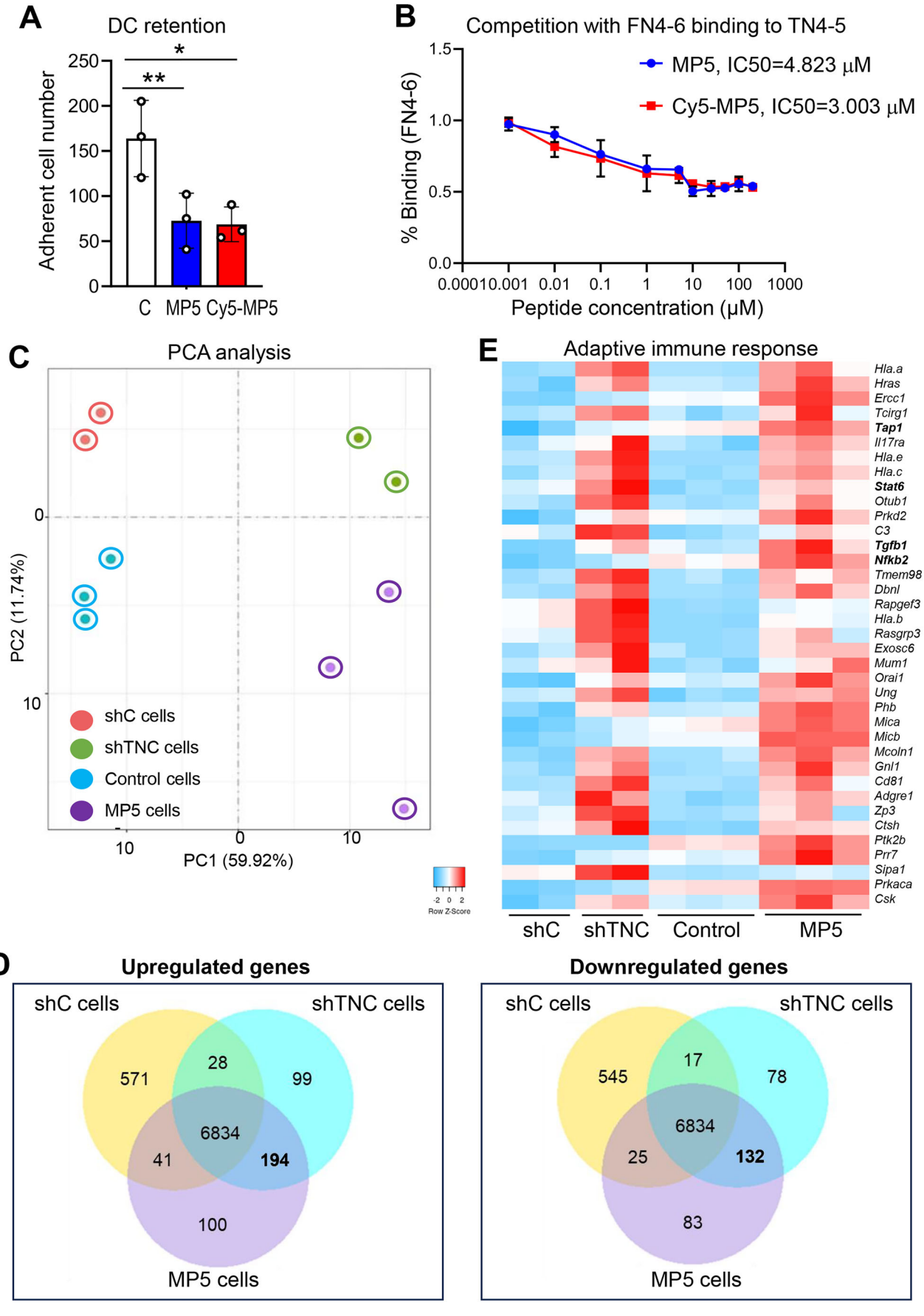
A
DC retention
Adherent cell number
250
200
150
100
50
0
*
**
C
MP5
Cy5-MP5
B
Competition with FN4-6 binding to TN4-5
MP5, IC50=4.823 µM
Cy5-MP5, IC50=3.003 µM
% Binding (FN4-6)
1.5
1.0
0.5
0.0
0.0001
0.001
0.01
0.1
1
10
100
1000
Peptide concentration (µM)
C
PCA analysis
PC2 (11.74%)
PC1 (59.92%)
shC cells
shTNC cells
Control cells
MP5 cells
Row Z-Score
E
Adaptive immune response
Hla.a
Hras
Ercc1
Tcirg1
Tap1
Il17ra
Hla.e
Hla.c
Stat6
Otub1
Prkd2
C3
Tgfb1
Nfkb2
Tmem98
Dbnl
Rapgef3
Hla.b
Rasgrp3
Exosc6
Mum1
Orai1
Ung
Phb
Mica
Micb
Mcoln1
Gnl1
Cd81
Adgre1
Zp3
Ctsh
Ptk2b
Prr7
Sipa1
Prkaca
Csk
shC
shTNC
Control
MP5
D
Upregulated genes
shC cells
shTNC cells
571
28
99
6834
41
194
100
MP5 cells
Downregulated genes
shC cells
shTNC cells
545
17
78
6834
25
132
83
MP5 cells

◀ **Figure EV6. Targeting TNC with MAREMO peptide MP5 reduces tumor cell proliferation and plasticity upon IR.**

(**A**) Chemoretention assay with DC2.4 cells measuring adhesion on the TNC-coated lower surface of the insert with 200 ng/mL CCL21 as chemoattractant. Note, both peptides (25 nM) cause release of the cells from TNC. $N = 3$ experiments; Mean ± SD; Ordinary one-way ANOVA test, $^*P < 0.05$. (**B**) Competitive ELISA measuring binding of FN4-6 to surface-adsorbed TN4-5 which is blocked in a dose-dependent manner by both MP5 and Cy5-MP5. Dose–response inhibition curves were fitted using nonlinear regression with a four-parameter logistic model. IC_{50} values were compared using an extra sum-of-squares F test. $N = 3$ experiments, Mean ± SD. (**C**) PCA analysis of the RNA sequencing data from NT193 breast cancer cells (shC, shTNC, Control (PBS-treated) and MP5-treated), indicating a similar distribution of the shTNC and MP5 samples. (**D**) RNA sequencing analysis of the upregulated and downregulated genes in NT193 breast cancer cells shC, shTNC or MP5-treated. In the centre, the commonly expressed genes between all categories are shown. 194 genes are commonly upregulated in the MP5 and shTNC conditions compared to the shC condition, and 132 genes are commonly downregulated in the MP5 and shTNC conditions compared to the shC condition. (**E**) Heatmap representation of gene expression data (derived from RNA sequencing) linked to adaptive immune response between groups ($P < 0.05$). The exact P values are listed in Appendix Table S5.

Appendix

Tenascin-C orchestrates radiotherapy-induced head and neck tumor regression

Thomas Loustau[1,2+]*, Ioanna Mitrentsi[1+], Nuohan Wang[1], Caroline Spenlé[1,3], Alexia Pavlidaki[1], Thibaud Tranchant[1], Gilles Riegel[1], Akhil Venu[1], Rime Oueidat[1], Manuel Koch[4], Marion Dumas[1], Fanny Wack[1], Aurelie Hirschler[5], Christine Carapito[5], Nicodème Paul[6], Raphael Carapito[6], Matthias Mörgelin[7], Uwe Hansen[8], Joyce Azzi[9,10], Lucie Aubergeon[11], Nathalie Salomé[1], Sayda Dhaouadi[12], Pierre Grenot[13], Balkiss Bouhaouala-Zahar[12], Simona La Cioppa[14], Philippe Oertle[14], Valerio Izzi[15], Marija Plodinec[14], Georges Noel[9,10], Hélène Burckel[9,10] and Gertraud Orend[1]*

Afiliations:

[1] INSERM U1109, The Tumor Microenvironment Laboratory, Hôpital Civil, Institut d'Hématologie et d'Immunologie, 67091 Strasbourg, France

[2] University of Strasbourg, UPR CNRS 9002, ARN, IUT Louis Pasteur, 1 allée d'Athènes, 67300 Schiltigheim, France

[3] University of Strasbourg, ESBS, INSERM-ERL1321, groupe Biothérapie peptidique, Pôle Api, Bâtiment D, 300 Boulevard Sébastien Brant, 67400 Illkirch, France

[4] University Cologne, Faculty of Medicine and University Hospital Cologne, Center for Dental, Oral and Maxillofacial Medicine (central facilities), Cologne, Germany

[5] Laboratoire de Spectrométrie de Masse BioOrganique, Institut Pluridisciplinaire Hubert Curien (IPHC), UMR 7178, Université de Strasbourg, CNRS, Infrastructure Nationale de Protéomique ProFi - UAR2048, 67000 Strasbourg, France.

[6] Laboratoire d'ImmunoRhumatologie Moléculaire, INSERM UMR_S 1109, Plateforme GENOMAX, ITI Médecine de Précision de Strasbourg, Transplantex NG, Faculté de Médecine, Fédération Hospitalo-Universitaire OMICARE, France

[7] Colzyx AB, Lund, Sweden

[8] Institute for Musculoskeletal Medicine (IMM), University Hospital Muenster, Muenster, Germany

[9] Institut de Cancérologie Strasbourg Europe (ICANS), UNICANCER, Radiobiology Laboratory, Paul Strauss Comprehensive, Cancer Center, 67000 Strasbourg, France.

[10] ICube, UMR7357, Equipe Imagerie Multimodale Intégrative en Santé, Université de Strasbourg, France

[11] University of Strasbourg, UPR CNRS 3572, I2CT, 2 allée Konrad Roentgen 67084 Strasbourg, France

[12] Pasteur Institute of Tunis, NanoBioMedika research Team, 13 Place Pasteur - B.P. 74 - 1002 Tunis, Tunisia.

[13] Laboratoire d'ImmunoRhumatologie Moléculaire, INSERM UMR_S 1109, Plateforme CYTOMAX, Institut d'Hématologie et d'Immunologie, 67091 Strasbourg, France.

[14] Artidis, Hochbergerstrasse 60c, 4057 Basel, Switzerland

[15] Faculty of Biochemistry and Molecular Medicine at University of Oulu, Oulu, Finland

+ Co-first authorship

* Corresponding authors:

Thomas Loustau, INSERM U1109, The Tumor Microenvironment laboratory,

thomas.loustau@unistra.fr

Gertraud Orend, INSERM U1109, The Tumor Microenvironment laboratory,

gertraud.orend@inserm.fr

Figure S1

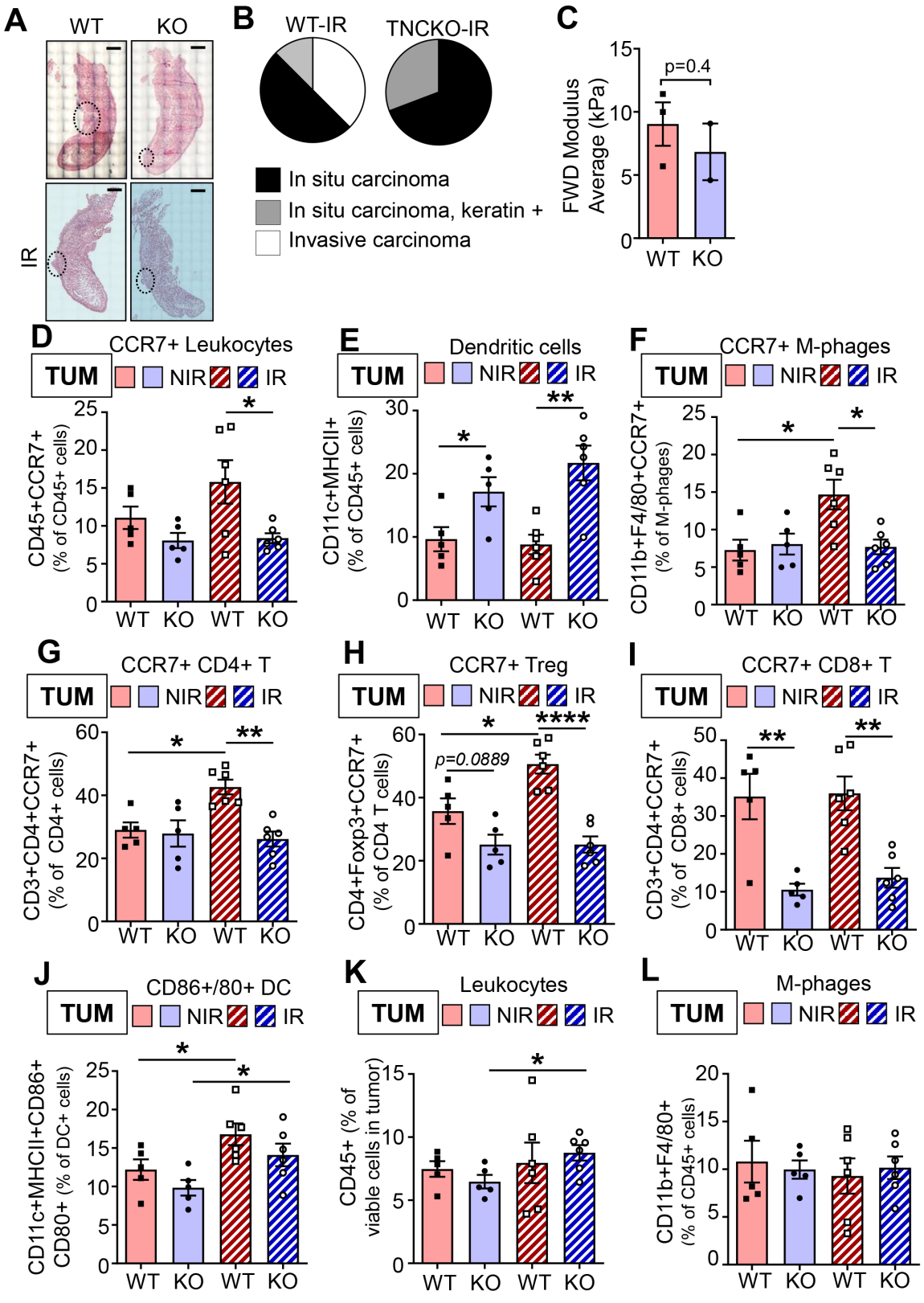
A
WT
KO
IR
B
WT-IR
TNCKO-IR
In situ carcinoma
In situ carcinoma, keratin +
Invasive carcinoma
C
FWD Modulus Average (kPa)
p=0.4
WT KO
D
CCR7+ Leukocytes
TUM
NIR
IR
CD45+CCR7+ (% of CD45+ cells)
WT KO WT KO
E
Dendritic cells
CD11c+MHCII+ (% of CD45+ cells)
F
CCR7+ M-phages
CD11b+F4/80+CCR7+ (% of M-phages)
G
CCR7+ CD4+ T
CD3+CD4+CCR7+ (% of CD4+ cells)
H
CCR7+ Treg
p=0.0889
CD4+Foxp3+CCR7+ (% of CD4 T cells)
I
CCR7+ CD8+ T
CD3+CD4+CCR7+ (% of CD8+ cells)
J
CD86+/80+ DC
CD11c+MHCII+CD86+ CD80+ (% of DC+ cells)
K
Leukocytes
CD45+ (% of viable cells in tumor)
L
M-phages
CD11b+F4/80+ (% of CD45+ cells)

Figure S1

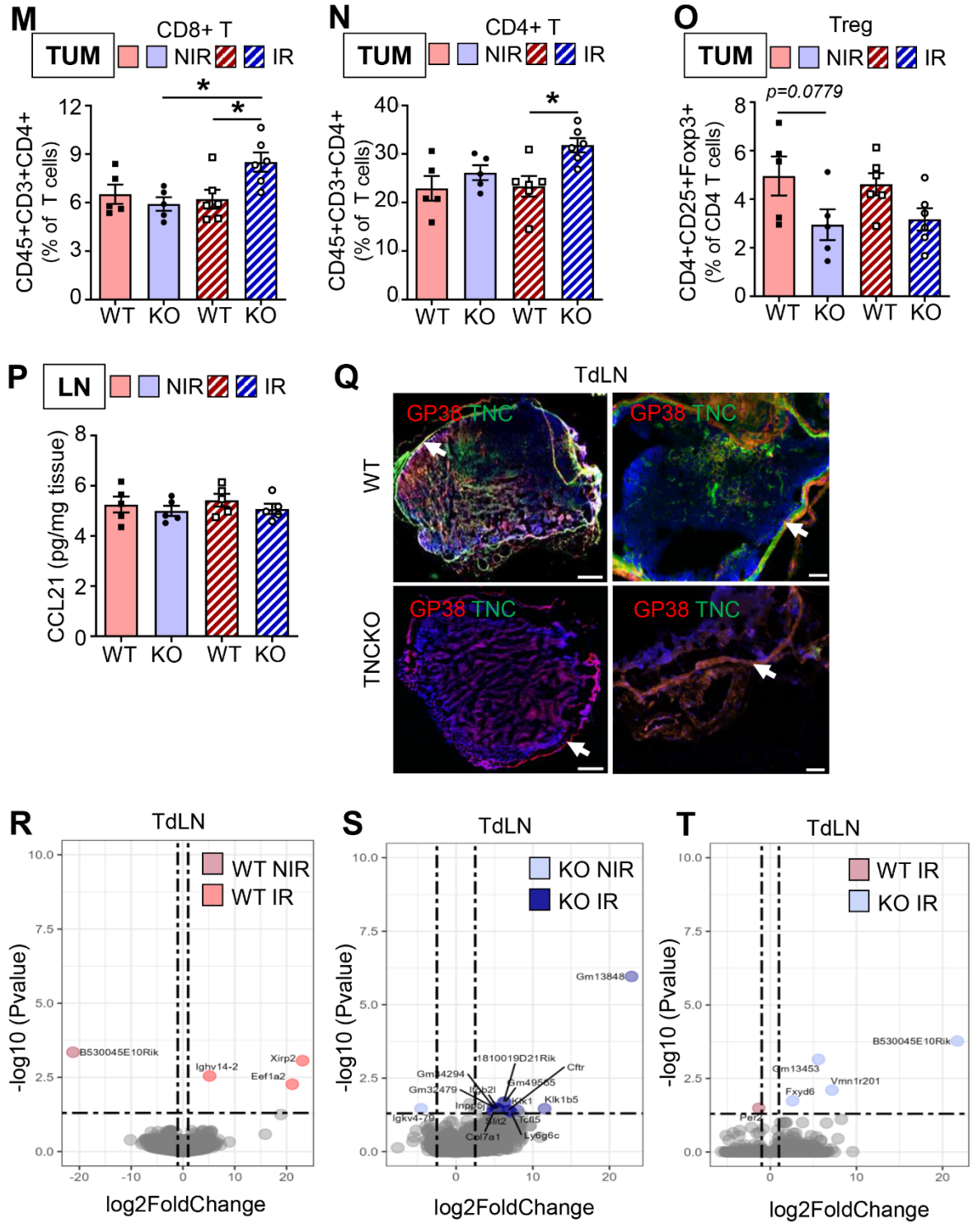
M
CD8+ T
TUM
NIR
IR
CD45+CD3+CD4+ (% of T cells)
WT KO WT KO
N
CD4+ T
TUM
NIR
IR
CD45+CD3+CD4+ (% of T cells)
WT KO WT KO
O
Treg
TUM
NIR
IR
p=0.0779
CD4+CD25+Foxp3+ (% of CD4 T cells)
WT KO WT KO
P
LN
NIR
IR
CCL21 (pg/mg tissue)
WT KO WT KO
Q
TdLN
WT
TNCKO
GP38 TNC
R
TdLN
WT NIR
WT IR
-log10 (Pvalue)
log2FoldChange
B530045E10Rik
Ighv14-2
Xirp2
Eef1a2
S
TdLN
KO NIR
KO IR
-log10 (Pvalue)
log2FoldChange
Gm13848
1810019D21Rik
Cftr
Gm49505
Klk1
Klk1b5
Tcfl5
Ly6g6c
Col7a1
Slit2
Igkv4-79
T
TdLN
WT IR
KO IR
-log10 (Pvalue)
log2FoldChange
B530045E10Rik
Gm13453
Vmn1r201
Fxyd6
Per2

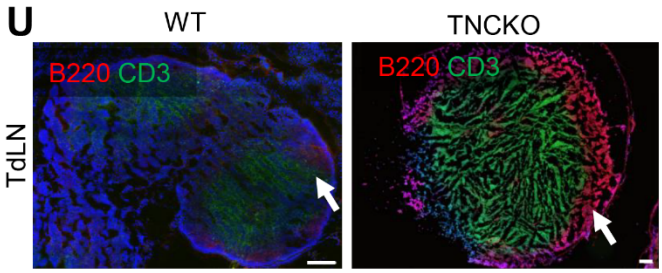
U
WT
TNCKO
TdLN
B220 CD3
B220 CD3

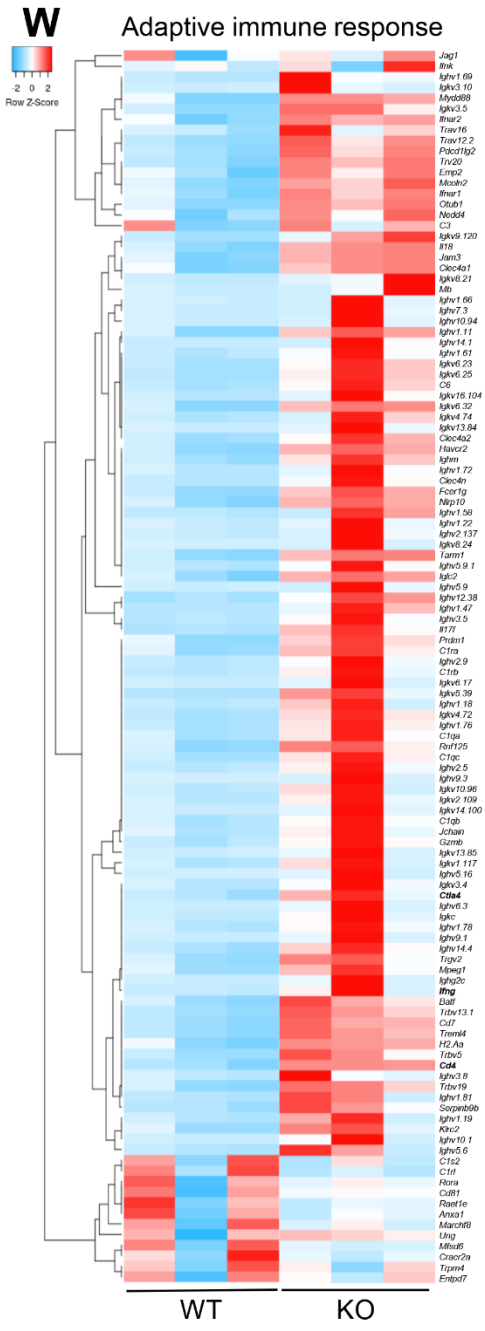
W
Adaptive immune response
-2 0 2
Row Z-Score
WT
KO

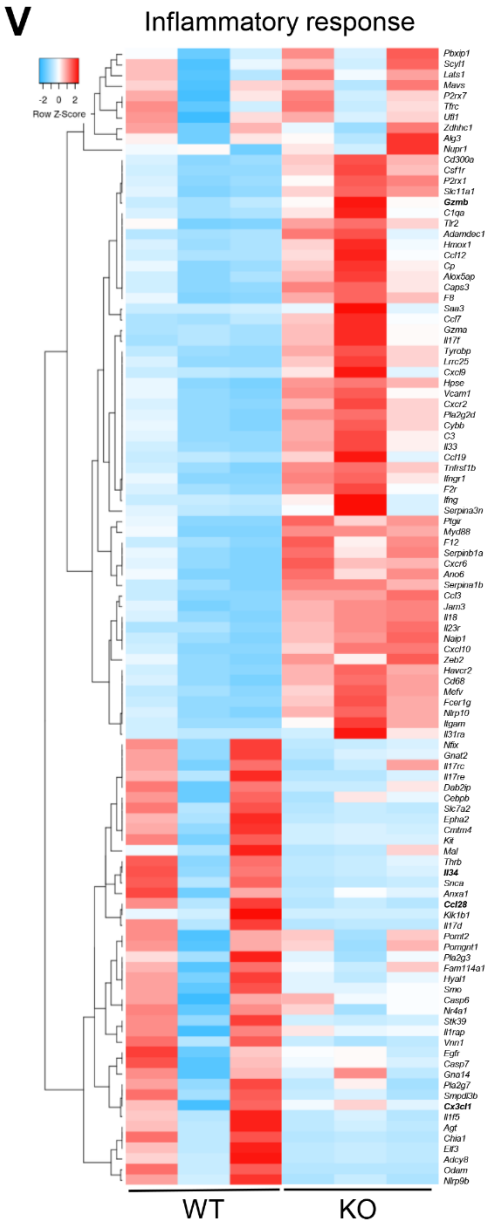
V
Inflammatory response
-2 0 2
Row Z-Score
WT
KO

Appendix Figure S1: Characterization and flow cytometry immunoprofiling of the 4NQO tumors and associated TdLNs after irradiation in WT and TNCKO mice (**A**) Representative composite images of hematoxylin and eosin-stained cross sections (n = 20) from tongues of 4NQO-treated WT and TNCKO mice non-irradiated (NIR) or irradiated (IR). The black circles indicate the tongue tumor. (**B**) Stage classification of radioresistant tongue tumors in WT and TNCKO mice upon IR. Lesions (n = 8 KO, 10 WT) were classified in differentiated squamous cell carcinoma (black), in situ carcinoma expressing keratin (gray) or invasive carcinoma (white). (**C**) Forward (FWD) E-Modulus average (kPA) of the corresponding Atomic Force Microscopy (AFM) measurements with passed quality check. Between 9 and 27 measurements were done per tumor sample. N = 2 or 3 tumors per condition. Mean ± SEM; Mann-Whitney test. (**D-O**) FACS analysis of NIR and IR 4NQO tumors (TUM) of WT and TNCKO mice for CCR7+ leukocytes (**D**), dendritic cells (**E**), CCR7+ macrophages (**F**), CCR7+ CD4+ T cells (**G**), CCR7+ Treg (**H**), CCR7+ CD8+ T cells (**I**), CD86/80+ DC (**J**), CD45+ leukocytes (**K**), macrophages (**L**), CD8+ T cells (**M**), CD4+ T cells (**N**) and T regulatory (Treg) cells (**O**). (**P**) ELISA for CCL21 in NIR and IR 4NQO TdLNs of 4NQO exposed WT and TNCKO mice. (**Q**) Representative IF images for GP38 and TNC in the TdLNs of WT and TNC KO mice in a lower (left panel) or higher (right panel) maginification. Scale bars, 50 μm. Arrows point at the reticular fibers. The IF image of the WT TdLN (upper left panel) is used in the summary cartoon of **Fig 7C.** N = 5 TdLNs per group. **(R-T)** Volcano plots of deregulated genes after RNA sequencing of the TdLNs of WT mice NIR or after 2Gy IR (**R**), TNC KO mice NIR or after 2Gy IR (**S**) and WT or TNC KO mice after 2Gy IR (**T**). n= 3 TdLNs per group. (**U**) Representative IF images for B220 and CD3 in the TdLNs of WT and TNCKO. n= 5 TdLNs per group. Scale bars, 50 μm. (**V, W**) Heatmap representation of gene expression data (derived from RNA seq analysis) of TdLNs from WT compared to TNCKO tumor mice. P <0.05. Mean ± SEM; Kruskal–Wallis test and Dunn post-test, *, P < 0.05, **, P < 0.01, ***, P<0.005. The exact p values are listed in **Appendix Table S5**.

Figure S2

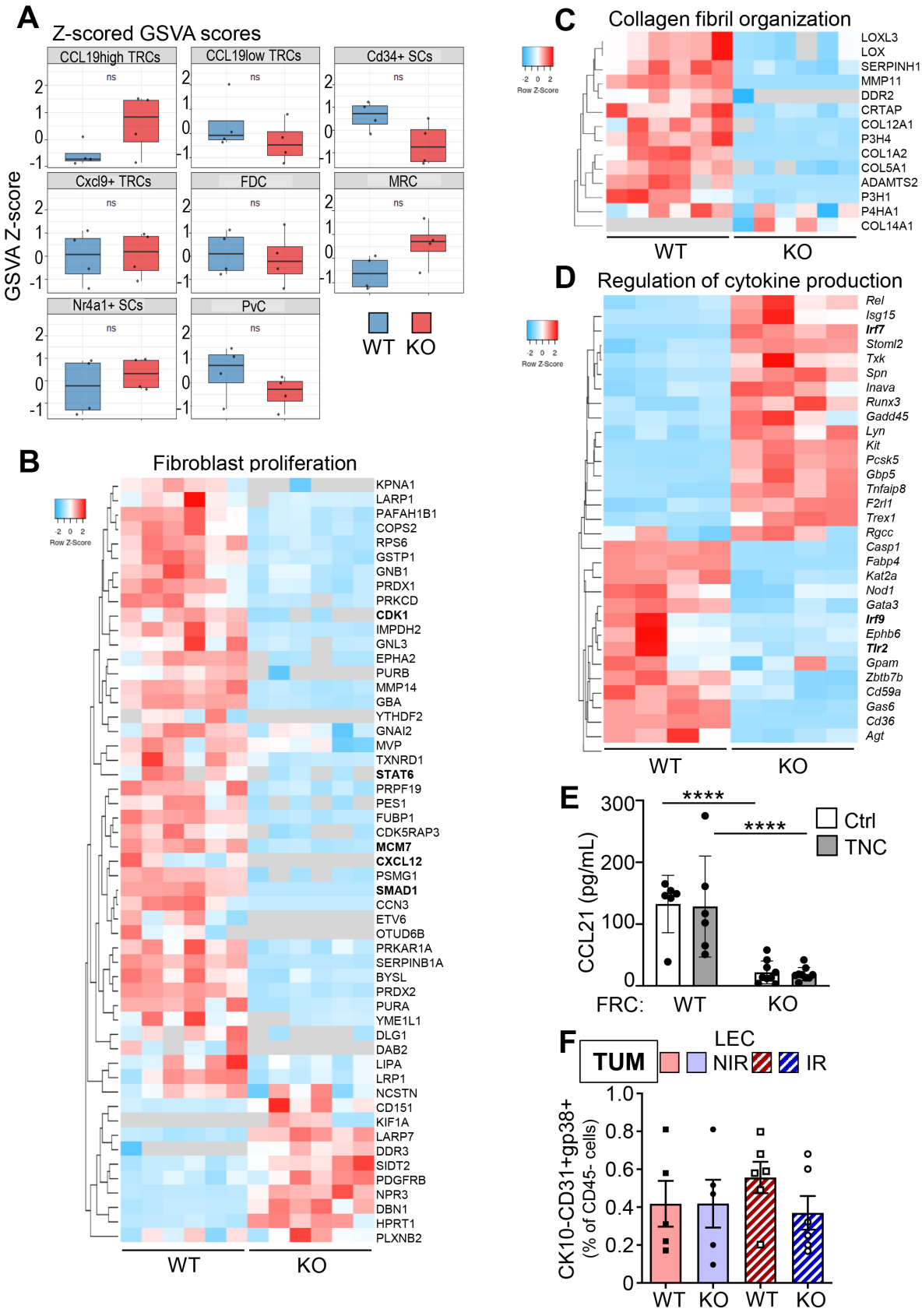
A
Z-scored GSVA scores
CCL19high TRCs
CCL19low TRCs
Cd34+ SCs
Cxcl9+ TRCs
FDC
MRC
Nr4a1+ SCs
PvC
ns
GSVA Z-score
WT KO
B
Fibroblast proliferation
Row Z-Score
KPNA1
LARP1
PAFAH1B1
COPS2
RPS6
GSTP1
GNB1
PRDX1
PRKCD
CDK1
IMPDH2
GNL3
EPHA2
PURB
MMP14
GBA
YTHDF2
GNAI2
MVP
TXNRD1
STAT6
PRPF19
PES1
FUBP1
CDK5RAP3
MCM7
CXCL12
PSMG1
SMAD1
CCN3
ETV6
OTUD6B
PRKAR1A
SERPINB1A
BYSL
PRDX2
PURA
YME1L1
DLG1
DAB2
LIPA
LRP1
NCSTN
CD151
KIF1A
LARP7
DDR3
SIDT2
PDGFRB
NPR3
DBN1
HPRT1
PLXNB2
WT KO
C
Collagen fibril organization
LOXL3
LOX
SERPINH1
MMP11
DDR2
CRTAP
COL12A1
P3H4
COL1A2
COL5A1
ADAMTS2
P3H1
P4HA1
COL14A1
WT KO
D
Regulation of cytokine production
Rel
Isg15
Irf7
Stoml2
Txk
Spn
Inava
Runx3
Gadd45
Lyn
Kit
Pcsk5
Gbp5
Tnfaip8
F2rl1
Trex1
Rgcc
Casp1
Fabp4
Kat2a
Nod1
Gata3
Irf9
Ephb6
Tlr2
Gpam
Zbtb7b
Cd59a
Gas6
Cd36
Agt
WT KO
E
CCL21 (pg/mL)
300
200
100
0
****
****
Ctrl
TNC
FRC: WT KO
F
TUM
LEC
NIR
IR
CK10-CD31+gp38+
(% of CD45- cells)
1.0
0.8
0.6
0.4
0.2
0
WT KO WT KO

Appendix Figure S2: TNC expression plays a pivotal role in determining the FRC identity (**A**) RNA sequencing Gene Set Variation Analysis (GSVA) for the different FRC subclusters in the WT and TNCKO FRCs. Proteomics data analysis (**B, C**) represented as heatmaps for the most deregulated proteins that belong to fibroblast proliferation (**B**) and collagen fibril organization (**C**). $P < 0.05$. (**D**) RNA seq gene expression analysis represented as heatmap for deregulated gene members of the regulation of cytokine production. Bold text indicates genes/proteins with established roles in the respective categories and/or that are discussed in the text. $P < 0.05$. (**E**) Quantification of CCL21 by ELISA in WT or TNCKO FRCs, either non-treated control (Ctrl) or treated with soluble TNC (10 µg/mL) for 24 hours. Mean ± SEM; Kruskal–Wallis test and Dunn posttest, *, $P < 0.05$. (**F**) FACS analysis of lymphatic endothelial cells in NIR and IR 4NQO tumors (Tum) of WT and TNCKO mice. Mean ± SEM; Kruskal–Wallis test and Dunn post-test. The exact p values are listed in **Appendix Table S5**.

Figure S3

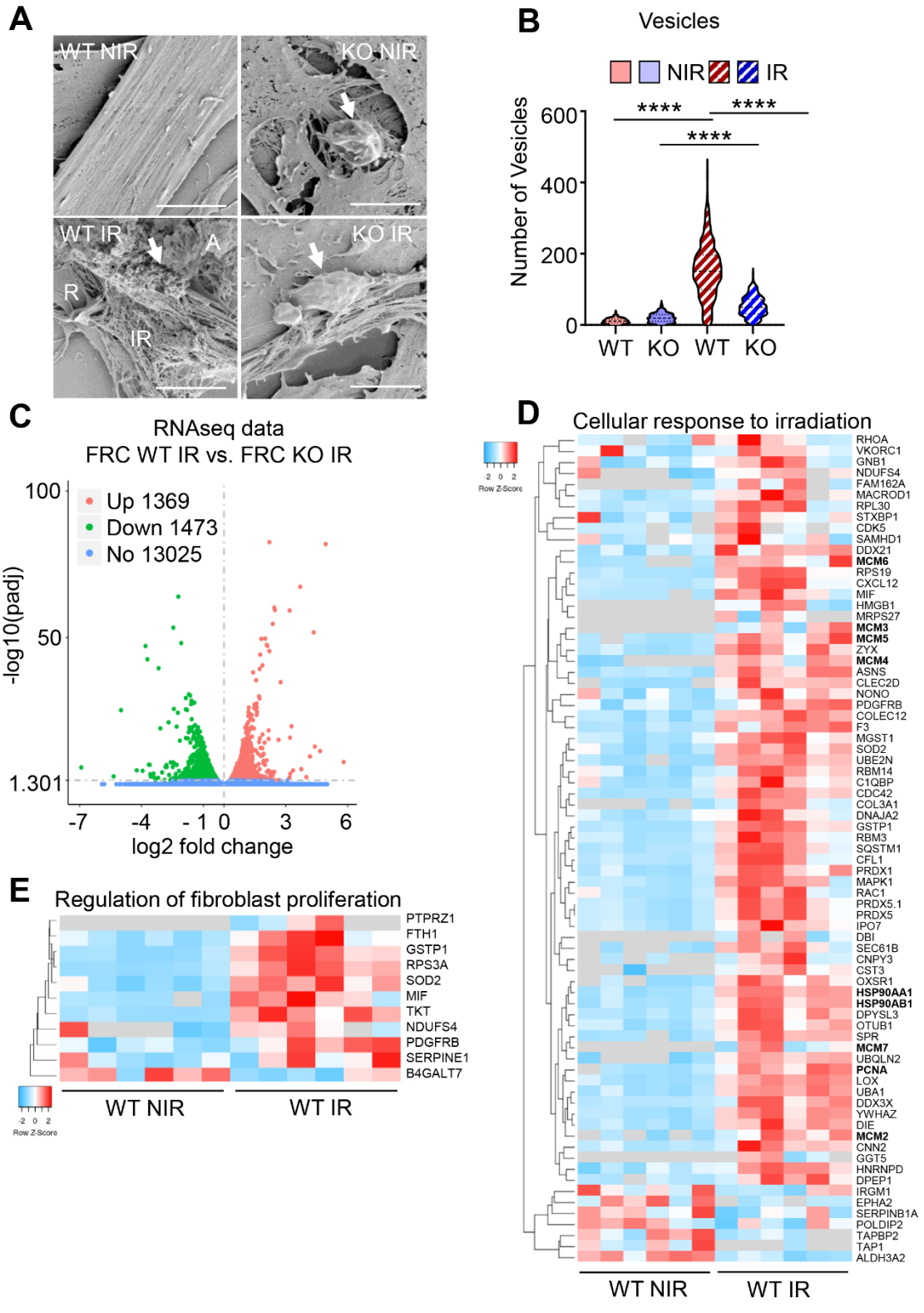
A
WT NIR
KO NIR
WT IR
KO IR
A
R
IR
B
Vesicles
NIR
IR
Number of Vesicles
600
400
200
0
****
****
****
WT
KO
WT
KO
C
RNAseq data
FRC WT IR vs. FRC KO IR
Up 1369
Down 1473
No 13025
-log10(padj)
100
50
1.301
-7
-4
- 1
0
3
6
log2 fold change
D
Cellular response to irradiation
Row Z-Score
RHOA
VKORC1
GNB1
NDUFS4
FAM162A
MACROD1
RPL30
STXBP1
CDK5
SAMHD1
DDX21
MCM6
RPS19
CXCL12
MIF
HMGB1
MRPS27
MCM3
MCM5
ZYX
MCM4
ASNS
CLEC2D
NONO
PDGFRB
COLEC12
F3
MGST1
SOD2
UBE2N
RBM14
C1QBP
CDC42
COL3A1
DNAJA2
GSTP1
RBM3
SQSTM1
CFL1
PRDX1
MAPK1
RAC1
PRDX5.1
PRDX5
IPO7
DBI
SEC61B
CNPY3
CST3
OXSR1
HSP90AA1
HSP90AB1
DPYSL3
OTUB1
SPR
MCM7
UBQLN2
PCNA
LOX
UBA1
DDX3X
YWHAZ
DIE
MCM2
CNN2
GGT5
HNRNPD
DPEP1
IRGM1
EPHA2
SERPINB1A
POLDIP2
TAPBP2
TAP1
ALDH3A2
WT NIR
WT IR
E
Regulation of fibroblast proliferation
PTPRZ1
FTH1
GSTP1
RPS3A
SOD2
MIF
TKT
NDUFS4
PDGFRB
SERPINE1
B4GALT7
Row Z-Score
WT NIR
WT IR

Figure S3

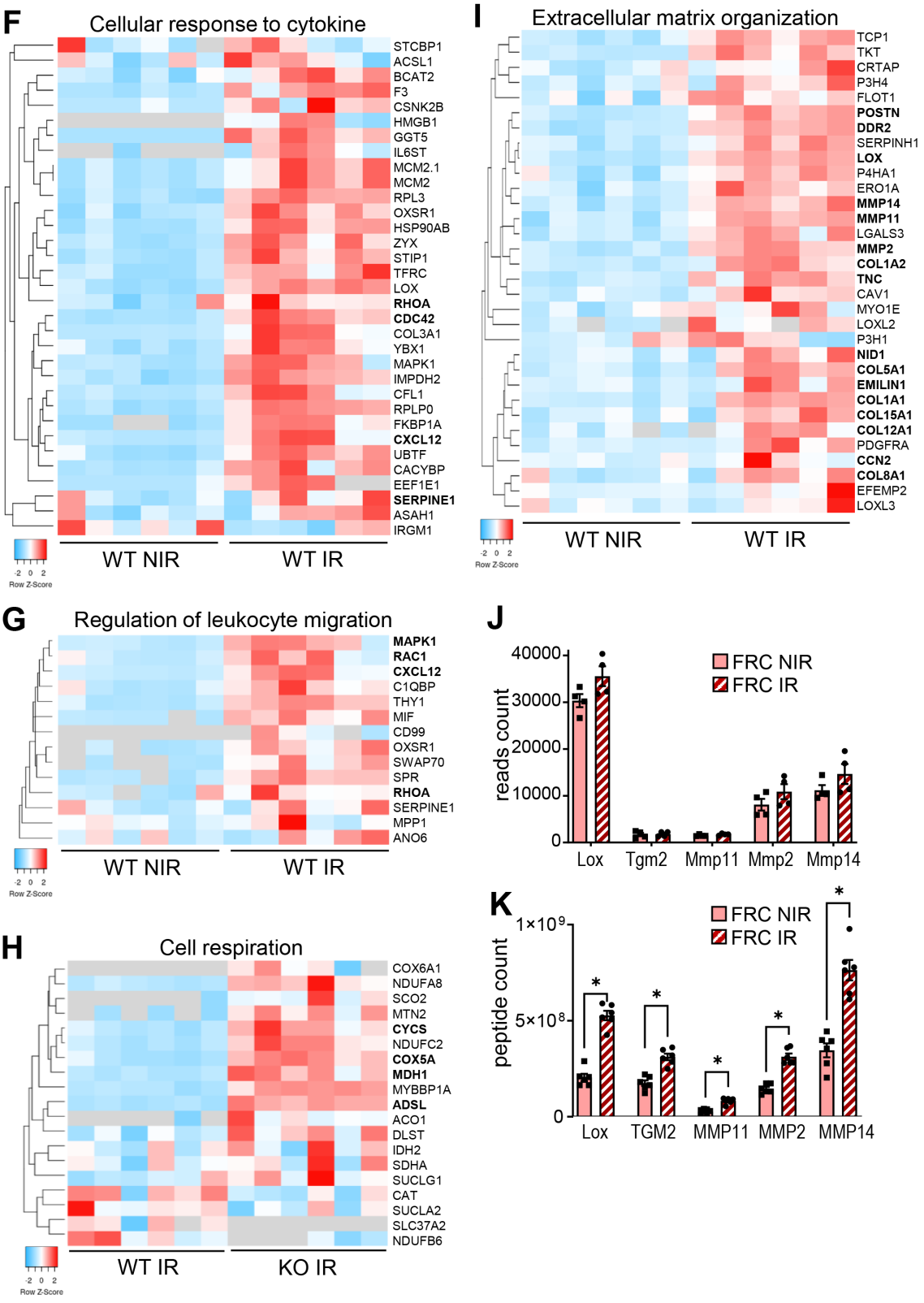
F
Cellular response to cytokine
STCBP1
ACSL1
BCAT2
F3
CSNK2B
HMGB1
GGT5
IL6ST
MCM2.1
MCM2
RPL3
OXSR1
HSP90AB
ZYX
STIP1
TFRC
LOX
RHOA
CDC42
COL3A1
YBX1
MAPK1
IMPDH2
CFL1
RPLP0
FKBP1A
CXCL12
UBTF
CACYBP
EEF1E1
SERPINE1
ASAH1
IRGM1
WT NIR
WT IR
Row Z-Score
I
Extracellular matrix organization
TCP1
TKT
CRTAP
P3H4
FLOT1
POSTN
DDR2
SERPINH1
LOX
P4HA1
ERO1A
MMP14
MMP11
LGALS3
MMP2
COL1A2
TNC
CAV1
MYO1E
LOXL2
P3H1
NID1
COL5A1
EMILIN1
COL1A1
COL15A1
COL12A1
PDGFRA
CCN2
COL8A1
EFEMP2
LOXL3
WT NIR
WT IR
Row Z-Score
G
Regulation of leukocyte migration
MAPK1
RAC1
CXCL12
C1QBP
THY1
MIF
CD99
OXSR1
SWAP70
SPR
RHOA
SERPINE1
MPP1
ANO6
WT NIR
WT IR
Row Z-Score
J
40000
30000
20000
10000
0
reads count
FRC NIR
FRC IR
Lox
Tgm2
Mmp11
Mmp2
Mmp14
H
Cell respiration
COX6A1
NDUFA8
SCO2
MTN2
CYCS
NDUFC2
COX5A
MDH1
MYBBP1A
ADSL
ACO1
DLST
IDH2
SDHA
SUCLG1
CAT
SUCLA2
SLC37A2
NDUFB6
WT IR
KO IR
Row Z-Score
K
1×10^9
5×10^8
0
peptide count
FRC NIR
FRC IR
Lox
TGM2
MMP11
MMP2
MMP14

Figure S3

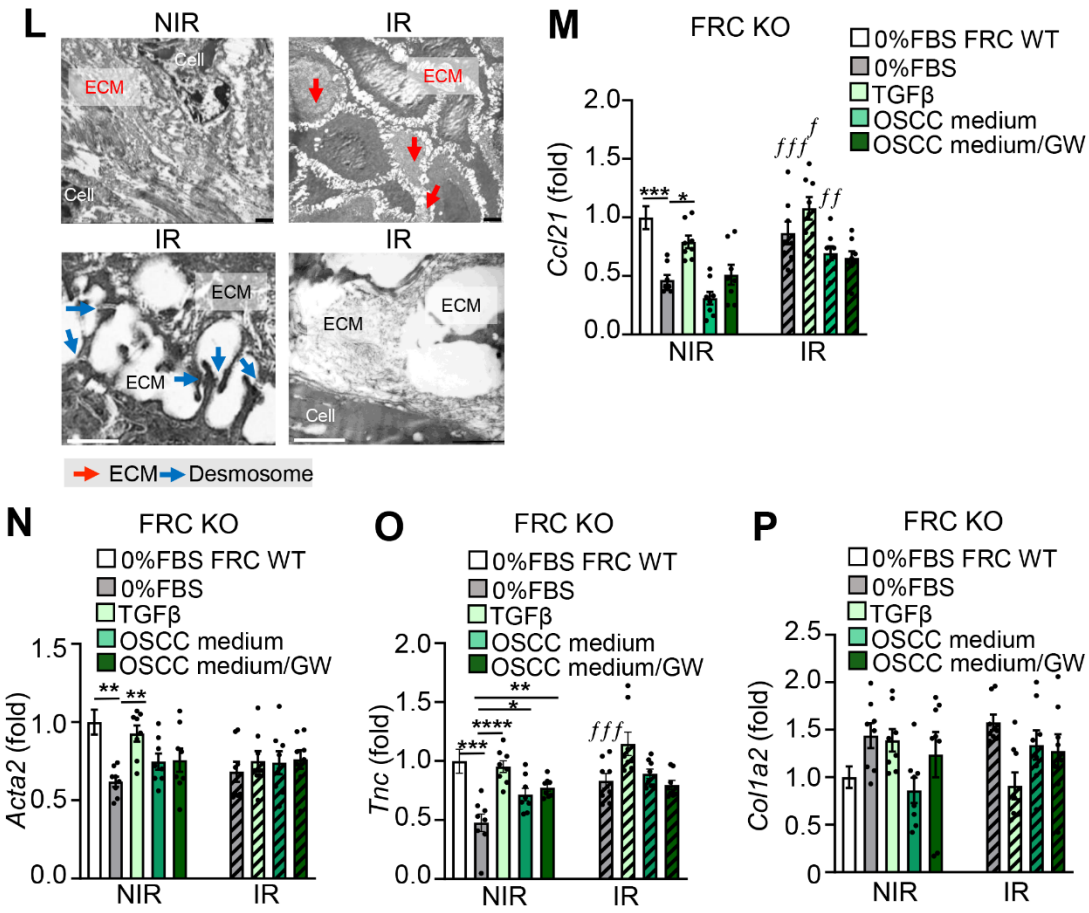

Appendix Figure S3: The FRC cell response to irradiation is determined by TNC expression (**A)** Representative SEM images of non-irradiated (NIR) or irradiated (IR) FRC WT and FRC TNCKO. Scale bar, 5µm. Images show regular (R), irregular (IR) and amorphous (A) fibril organization. (**B)** Cell vesicles quantification determined after the analysis of 300 SEM images of each cell condition. Mean ±SD; One way – ANOVA and Tukey's multiple comparisons post-test. (**C**) Volcano plot representation of deregulated genes (DEGs) obtained after RNA sequencing of irradiated FRC WT and TNCKO showing the fold change and the adjusted p-value for the 15 867 genes expressed. Red dots (1 369) represent genes significantly overexpressed in irradiated WT compared to TNCKO FRCs. Proteomic analysis of WT FRC in NIR vs. IR comparison, represented as heatmaps for deregulated proteins involved in the cellular response to irradiation (**D**), regulation of fibroblast proliferation (**E**), cellular response to cytokines (**F**), regulation of leukocyte migration (**G**) and ECM organization (**I**). $P < 0.05$. (**H**) Heatmaps representing deregulated proteins involved in cell respiration in irradiated WT vs. TNCKO FRCs. $P < 0.05$. (**J, K**) Gene reads counts (**J**) and peptide counts (**K**) of LOX, TGM2, MMP11, MMP2 and MMP14 in WT FRCs NIR vs IR. (**L**) EM images of NIR and IR tumors as indicated. Scale bar, 500 nm (upper panels), 1000 nm (lower panels). ECM (red) and desmosomes (blue) are indicated by

arrows. (**M-P)** Gene expression as determined by qRTPCR in FRC TNCKO for *Ccl21*, *Acta2*, *Tnc* and *Col1a2* after incubation with the indicated conditions. One-way ordinary ANOVA with * $P < 0.05$, ** $P < 0.01$, *** $P < 0.005$. The exact p values are listed in **Appendix Table S5**.

Figure S4

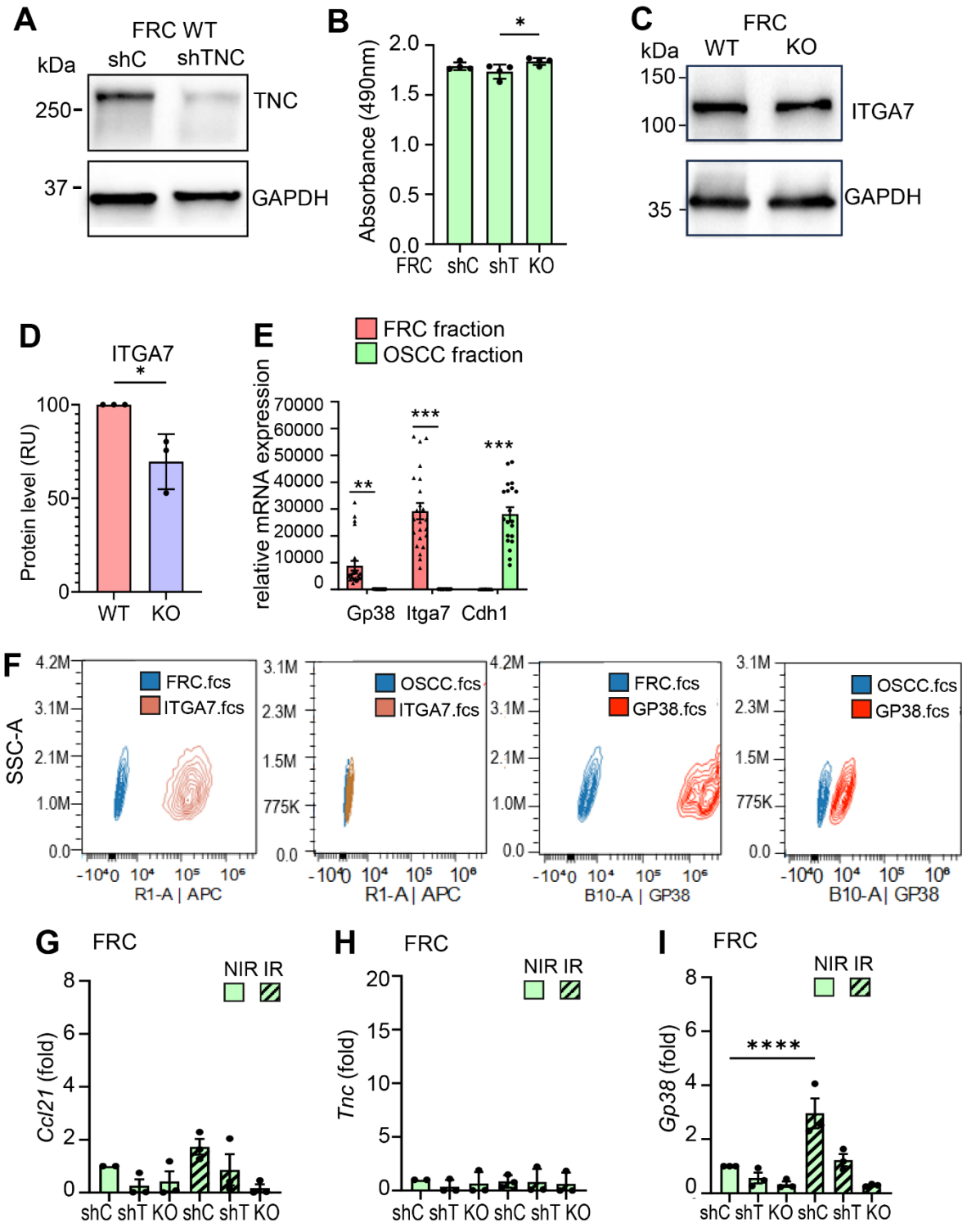
A
FRC WT
shC
shTNC
kDa
250-
TNC
37-
GAPDH
B
Absorbance (490nm)
2.0
1.5
1.0
0.5
0.0
*
FRC
shC
shT
KO
C
FRC
kDa
WT
KO
150-
100-
ITGA7
35-
GAPDH
D
ITGA7
*
Protein level (RU)
100
50
0
WT
KO
E
FRC fraction
OSCC fraction
relative mRNA expression
70000
60000
50000
40000
30000
20000
10000
0
**
***
***
Gp38
Itga7
Cdh1
F
SSC-A
FRC.fcs
ITGA7.fcs
OSCC.fcs
ITGA7.fcs
FRC.fcs
GP38.fcs
OSCC.fcs
GP38.fcs
R1-A | APC
R1-A | APC
B10-A | GP38
B10-A| GP38
G
FRC
NIR IR
Ccl21 (fold)
H
FRC
NIR IR
Tnc (fold)
I
FRC
NIR IR
****
Gp38 (fold)
shC shT KO shC shT KO

Figure S4

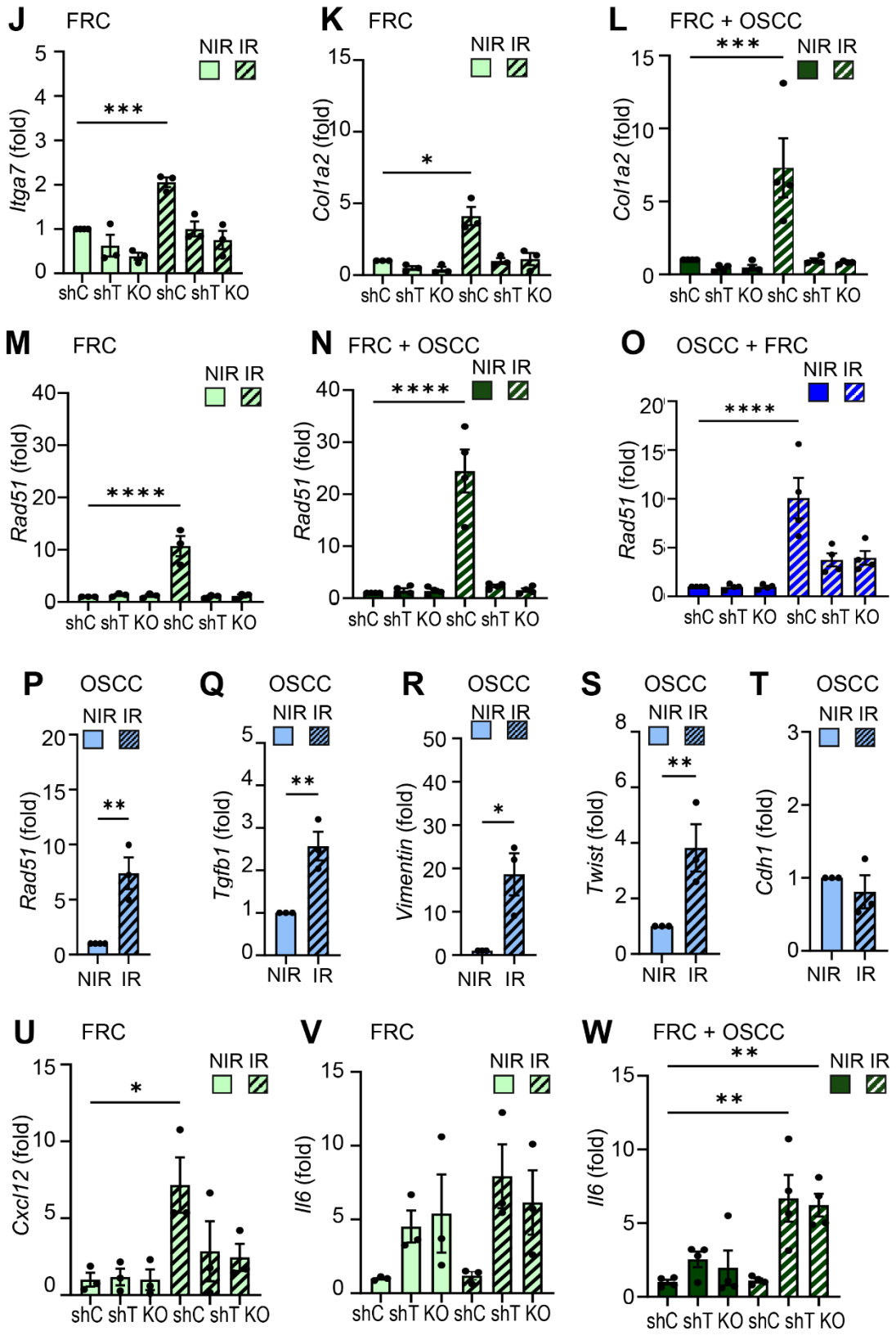
J
FRC
NIR IR
Itga7 (fold)
***
shC shT KO shC shT KO
K
FRC
NIR IR
Col1a2 (fold)
*
shC shT KO shC shT KO
L
FRC + OSCC
***
NIR IR
Col1a2 (fold)
shC shT KO shC shT KO
M
FRC
NIR IR
Rad51 (fold)
****
shC shT KO shC shT KO
N
FRC + OSCC
NIR IR
****
Rad51 (fold)
shC shT KO shC shT KO
O
OSCC + FRC
NIR IR
****
Rad51 (fold)
shC shT KO shC shT KO
P
OSCC
NIR IR
Rad51 (fold)
**
NIR IR
Q
OSCC
NIR IR
Tgfb1 (fold)
**
NIR IR
R
OSCC
NIR IR
Vimentin (fold)
*
NIR IR
S
OSCC
NIR IR
Twist (fold)
**
NIR IR
T
OSCC
NIR IR
Cdh1 (fold)
NIR IR
U
FRC
NIR IR
Cxcl12 (fold)
*
shC shT KO shC shT KO
V
FRC
NIR IR
Il6 (fold)
shC shT KO shC shT KO
W
FRC + OSCC
**
**
NIR IR
Il6 (fold)
shC shT KO shC shT KO

Appendix Figure S4: **TNC impact on the OSCC/FRC crosstalk upon irradiation (A)** TNC expression (western blot) in shC and shTNC FRCs. GAPDH is used as control. **(B)** Absorbance at 490 nm after an MTS assay in shC, shTNC and TNCKO FRCs. **(C, D)** Expression of ITGA7 (western blot) in WT and TNCKO FRCs. GAPDH is used as control **(E)** Gene expression (qRTPCR) analysis of *Gp38, Cdh1* and *Itga7* upon OSCC13/FRC coculture, followed by isolation of cells by MACS. Note, that OSCC13 cells express *Cdh1* but not *Gp38* nor *Itga7*, while FRCs express *Gp38* and *Itga7* but not *Cdh1*. **(F)** FACS analysis of GP38 and ITGA7 in OSCC13 and FRC cells. **(G-N, U-W)** Gene expression (qRTPCR) analysis of *Ccl21* **(G)**, *Tnc* **(H)**, *Gp38* **(I)** , *Itga7* **(J)**, *Col1a2* **(K-L),** *Rad51* **(M-N),** *Cxcl12* **(U)** and *Il6* **(V-W)** in FRC monocultures (light green) or in the sorted cocultures with OSCC13 (dark green), before (NIR) or 2 days after 2 Gy irradiation (IR). **(O-T)** Gene expression (qRTPCR) analysis of *Rad51* (**O-P**)*, Tgfb1* **(Q)**, *vimentin* **(R)**, *Twist* **(S)** and *Cdh1* **(T)**, in OSCC13 monocultures (light blue) or in co-cultures with FRCs (shC, shTNC, KO) (dark blue), NIR or 2 days after 2 Gy irradiation (IR). Error bars represent mean ± SEM. N = 3. One way ordinary ANOVA test with * $P < 0,05$, ** $P < 0,01$, *** $P < 0,001$, **** $P < 0,0001$. The exact p values are listed in **Appendix Table S5**.

Figure S5

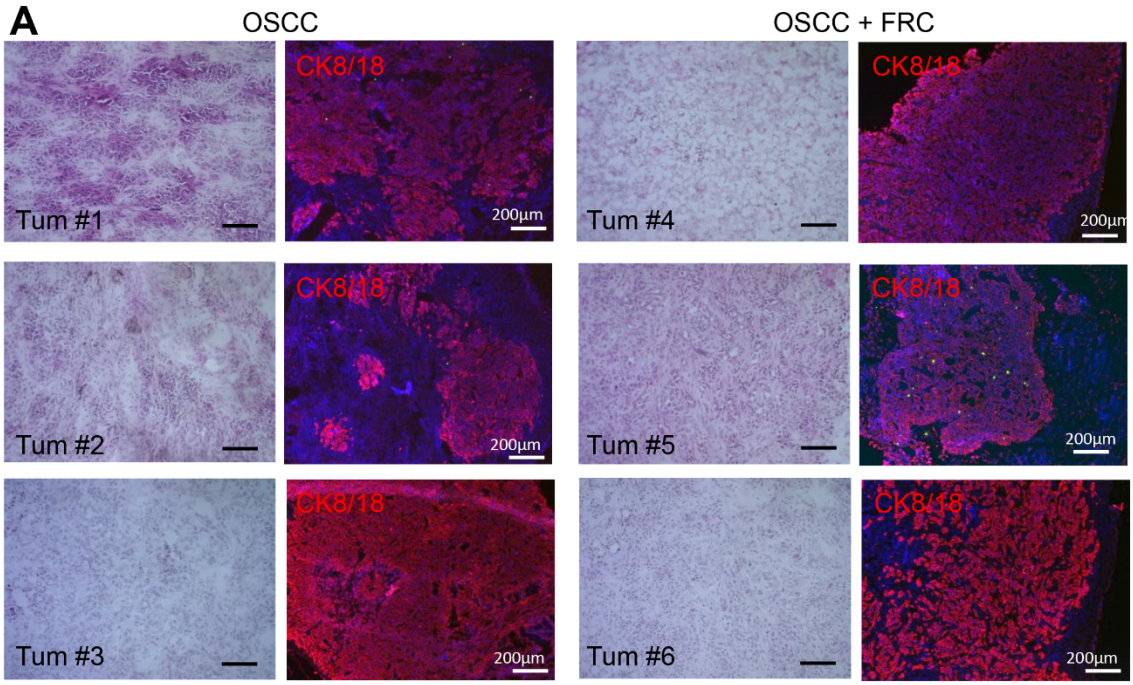
A
OSCC
OSCC + FRC
CK8/18
Tum #1
Tum #2
Tum #3
Tum #4
Tum #5
Tum #6
200µm

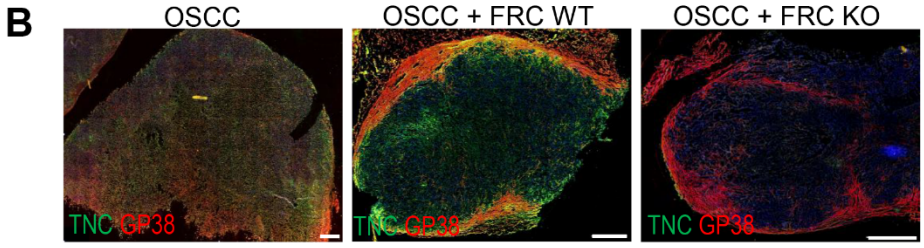
B
OSCC
OSCC + FRC WT
OSCC + FRC KO
TNC GP38

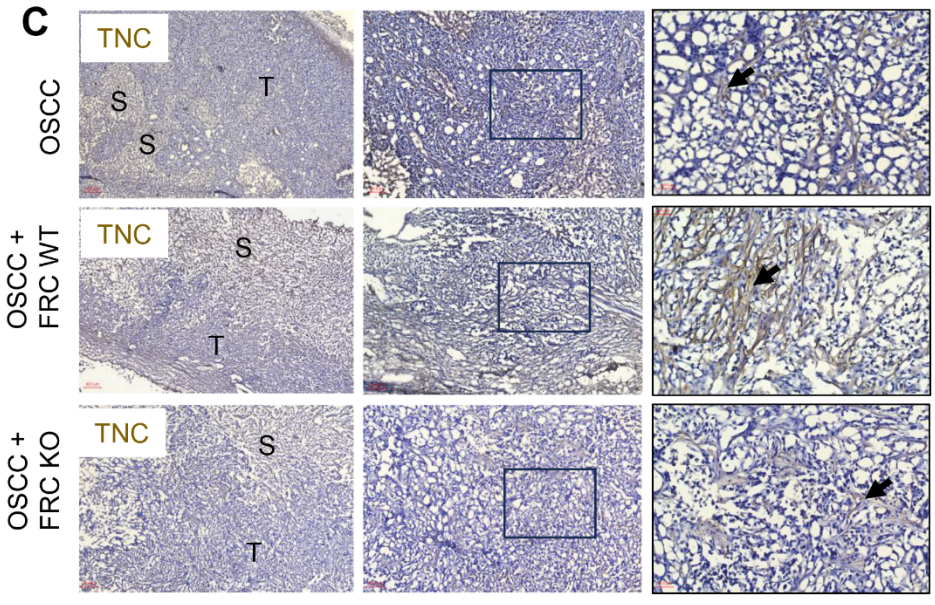
C
TNC
OSCC
OSCC + FRC WT
OSCC + FRC KO
S
T

Appendix Figure S5: Characterization of neck engrafted tumors in C57Bl6 mice (A) Staining of hematoxylin-eosin (HE) and IF staining in sections from 6 representative neck tumors obtained after OSCC grafting (1.5 x 10^6 cells) or OSCC/FRC (5:1) co-grafting of cells in WT mice. The CK8/18 IF image corresponding to **Fig 5B** is included here alongside additional tumors and H&E staining. Scale bar, 200 μm (**B, C**) Representative immunofluorescence images of TNC and GP38 (**B**) or Immunohistochemistry (IHC) images of TNC (**C**) in the tumors upon engraftment of OSCC cells alone (3 x 10^6 cells) or combined with WT FRC, or combined with FRC TNCKO cells, in a 5:1 ratio into the neck of WT mice, showing the tumor nests (S) and stroma (T) in the different conditions. OSCC indicates OSCC13 cells. Arrow points at TNC. Note that TNC is more abundant in FRC WT engrafted tumors. The IF image of the OSCC/FRC WT tumor shown in (**B**) is used in the summary cartoon of **Fig 7C.** Scale bar, 50 μm

Figure S6

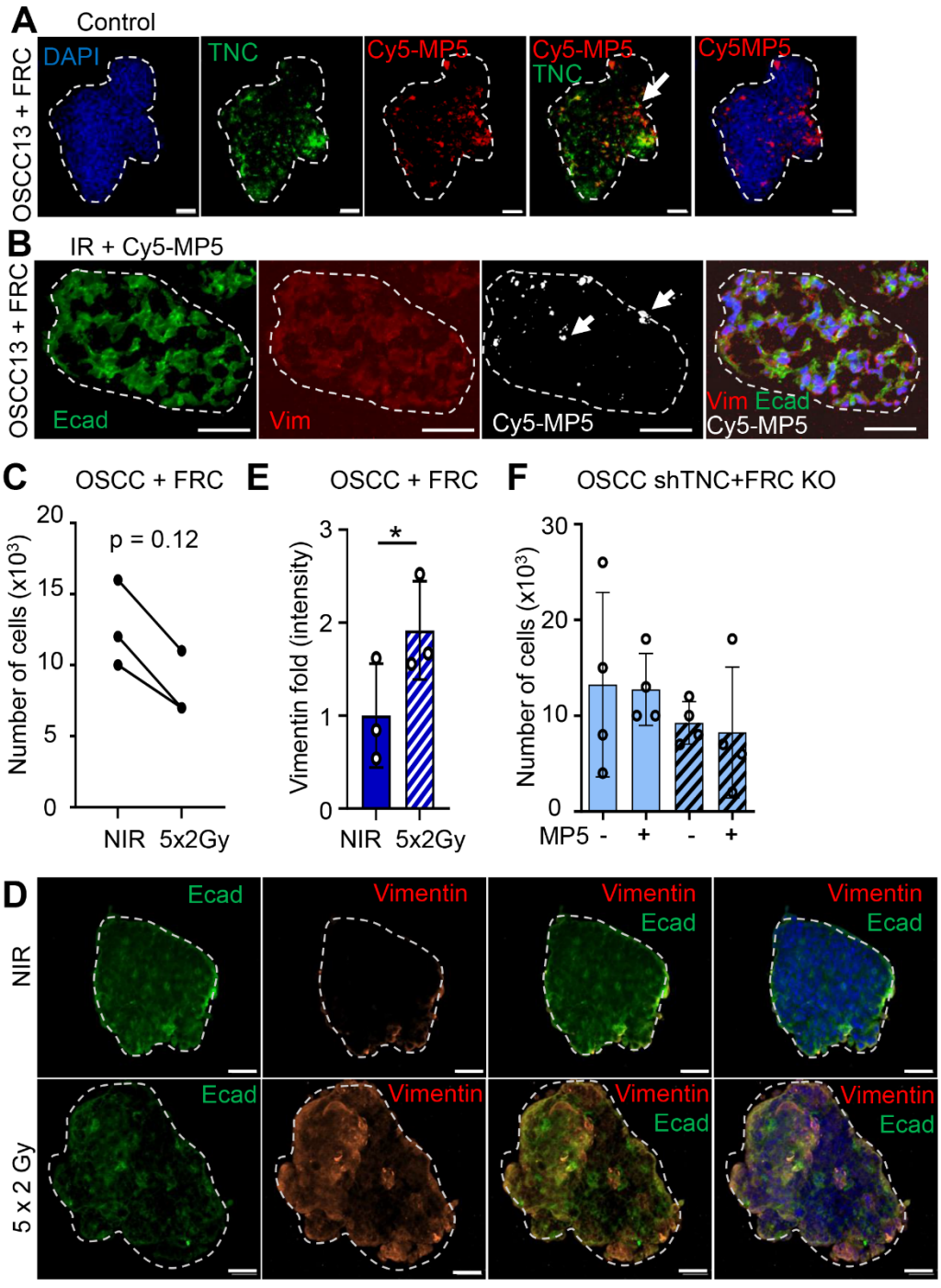
A
Control
OSCC13 + FRC
DAPI
TNC
Cy5-MP5
Cy5-MP5
TNC
Cy5MP5
B
IR + Cy5-MP5
OSCC13 + FRC
Ecad
Vim
Cy5-MP5
Vim Ecad
Cy5-MP5
C
OSCC + FRC
Number of cells (x10³)
p = 0.12
NIR 5x2Gy
E
OSCC + FRC
Vimentin fold (intensity)
*
NIR 5x2Gy
F
OSCC shTNC+FRC KO
Number of cells (x10³)
MP5 - + - +
D
NIR
5 x 2 Gy
Ecad
Vimentin
Vimentin
Ecad

Figure S6

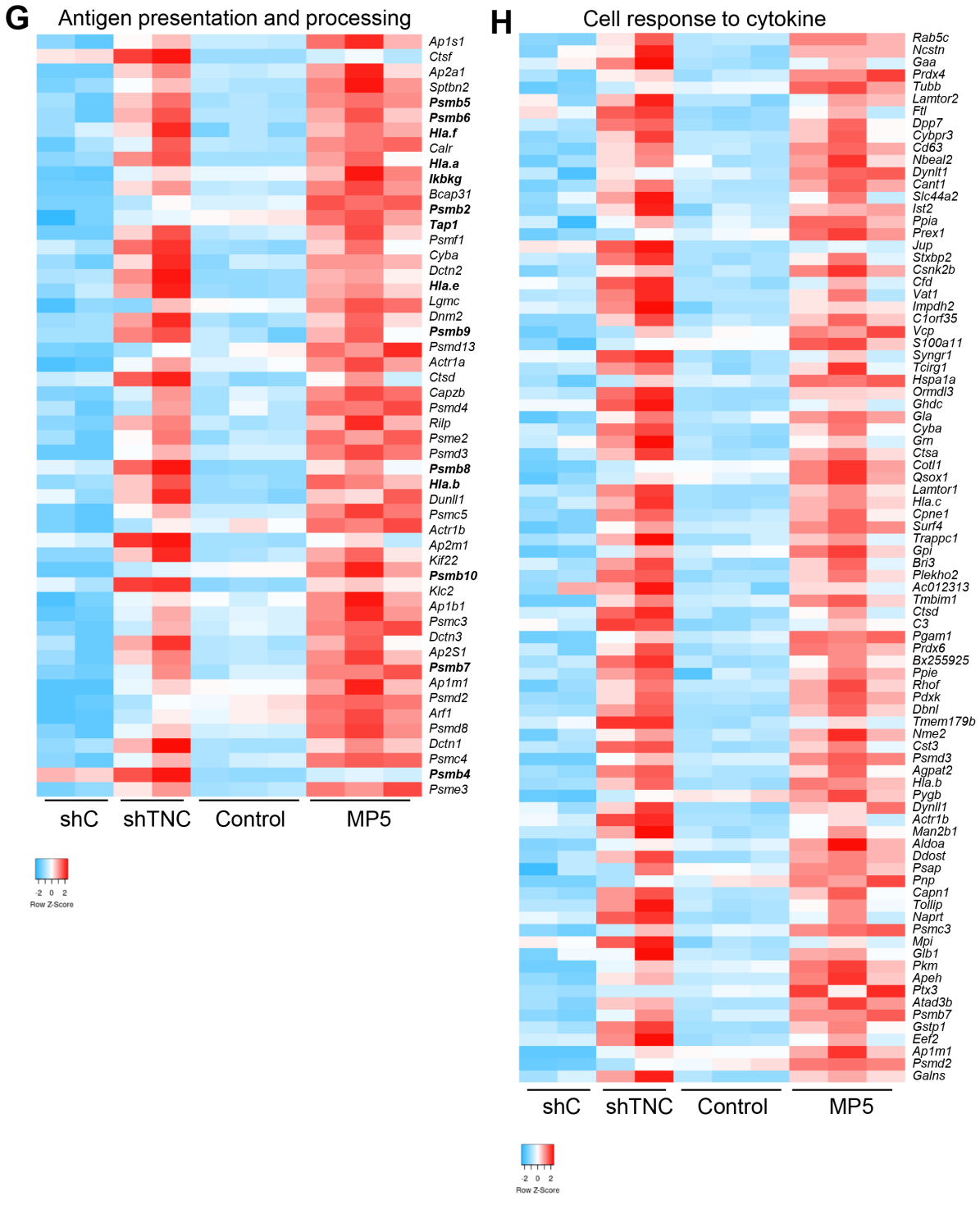
G
Antigen presentation and processing
Ap1s1
Ctsf
Ap2a1
Sptbn2
Psmb5
Psmb6
Hla.f
Calr
Hla.a
Ikbkg
Bcap31
Psmb2
Tap1
Psmf1
Cyba
Dctn2
Hla.e
Lgmc
Dnm2
Psmb9
Psmd13
Actr1a
Ctsd
Capzb
Psmd4
Rilp
Psme2
Psmd3
Psmb8
Hla.b
Dunll1
Psmc5
Actr1b
Ap2m1
Kif22
Psmb10
Klc2
Ap1b1
Psmc3
Dctn3
Ap2S1
Psmb7
Ap1m1
Psmd2
Arf1
Psmd8
Dctn1
Psmc4
Psmb4
Psme3
shC
shTNC
Control
MP5
-2 0 2
Row Z-Score
H
Cell response to cytokine
Rab5c
Ncstn
Gaa
Prdx4
Tubb
Lamtor2
Ftl
Dpp7
Cybpr3
Cd63
Nbeal2
Dynlt1
Cant1
Slc44a2
Ist2
Ppia
Prex1
Jup
Stxbp2
Csnk2b
Cfd
Vat1
Impdh2
C1orf35
Vcp
S100a11
Syngr1
Tcirg1
Hspa1a
Ormdl3
Ghdc
Gla
Cyba
Grn
Ctsa
Coll1
Qsox1
Lamtor1
Hla.c
Cpne1
Surf4
Trappc1
Gpi
Bri3
Plekho2
Ac012313
Tmbim1
Ctsd
C3
Pgam1
Prdx6
Bx255925
Ppie
Rhof
Pdxk
Dbnl
Tmem179b
Nme2
Cst3
Psmd3
Agpat2
Hla.b
Pygb
Dynll1
Actr1b
Man2b1
Aldoa
Ddost
Psap
Pnp
Capn1
Tollip
Naprt
Psmc3
Mpi
Glb1
Pkm
Apeh
Ptx3
Atad3b
Psmb7
Gstp1
Eef2
Ap1m1
Psmd2
Galns
shC
shTNC
Control
MP5
-2 0 2
Row Z-Score

Appendix Figure S6: Targeting TNC with MAREMO peptide MP5 reduces tumor cell numbers and plasticity upon IR (**A,B**) representative IF images of TNC (**A**) and Vim and Ecad (**B**) after addition of 50 ng Cy5-MP5 for 72h to OSCC13/FRC (2.1 ratio) spheroid cocultures. The individual fluorescence channels correspond to the composite images shown in **Fig 6A, E**. Spheroid cultures were exposed to 10 Gy IR followed by exposure to Cy5-MP5 for another 72h. (**C-E**) Cell number (**C**), representative IF images of Ecadherin and Vimentin (**D**) and quantification of vimentin intensity (**E**) before or after 5 doses of 2 Gy IR in OSCC13/FRC spheroid cocultures. (**F**) Cell number quantification of OSCC13 shTNC /FRC TNCKO spheroids before (NIR) or after 10 Gy IR and, with or without the addition of 50 ng MP5 for 72h. (**G, H**) Heatmap representation of gene expression data derived from RNA seq analysis of NT193 tumors of the indicated conditions. $P < 0.05$. Scale bars, 50 μm. One way-ordinary ANOVA with * $P < 0.05$, ** $P < 0.01$, *** $P < 0.005$. The exact p values are listed in **Appendix Table S5**.

Table S1 Differential gene expression in TNCKO TdLNs in comparison to WT TdLNs

Expression and p values of the genes differentialy expressed in TNCKO TdLNs in comparison to WT TdLNs as determined by RNA sequencing analysis with p value < 0.05. Data are deposited at the EMBL-EBI ArrayExrpress archive (E-MTAB-16360).

Table S1.1 TNCKO TdLNs vs WT TdLNs

Gene name	log2 (FoldChange)	padj
Gm12987	2.511966203	0.041167779
Sema3d	2.567876577	0.014276272
Gm37126	2.592280617	0.041167779
Ighv2-2	2.632829109	0.020735723
8030451A03Rik	2.709609155	0.042088513
Vwc2	2.72165088	0.020357857
Elfn2	2.731762113	0.04641008
Lyve1	2.797793007	0.011094218
Adra1b	2.828720367	0.005147109
Alpk3	3.043175694	0.037722793
Gm13868	3.049307321	0.024225547
Mmrn1	3.081743339	0.028507208
Igkv9-120	3.156997628	0.03396288
Igkv10-96	3.242494261	0.036807815
Ighv10-1	3.293828605	0.047130474
Igkv10-94	3.317565048	0.046705107
Cd5l	3.372442946	0.008102236
Igkv6-25	3.377964341	0.031061075
Igkv1-110	3.407651813	0.039613645
Clec4n	3.508842111	0.022263943
Igkv12-98	3.63722609	0.041826946
A130023I24Rik	3.66219486	0.0436441
Igkv4-79	3.673405716	0.029864011
Neb	3.678289573	0.020735723
Igkv10-95	3.756552702	0.04401888
Ighv1-58	3.856734247	0.017357758
Ighv9-3	3.998069033	0.038844683
Ighv1-7	4.072525674	0.013961075
Igkv4-86	4.208188449	0.030641479
Ccl8	4.232857541	0.003744706
Gm30648	4.291271862	0.046449898
Mybpc1	4.302796745	0.025112208
Cacna1s	4.339475354	0.017357758

Igkv6-17	4.397951382	0.024415161
Ighg2c	4.430442467	0.023281198
Ighv1-4	4.568696561	0.005147109
Ighv4-1	4.592402064	0.010983625
Gm13453	4.607759915	0.005452016
Igkv8-28	4.914650833	0.005147109
Igkv14-111	4.914975877	0.00962195
Ckmt2	5.201991649	0.030137594
Myh3	5.271677386	0.026430348
Gm47523	5.300097721	0.01425198
Gm44428	5.334805372	0.029703678
Sebox	5.418034693	0.016708274
Igkv5-45	5.464465711	0.016209472
Igkv14-126	5.540184388	0.004654508
Art1	5.786544269	0.045709433
Igkv11-125	5.864876769	0.034860387
Lrrc2	6.029266812	0.020739803
A930016O22Rik	6.265093315	0.034478029
Hotairm1	6.441699375	0.003744706
Jsrp1	6.453687282	0.018694338
Ckm	6.721148762	0.038610518
Tcap	6.826427953	0.033168524
Kcnj11	6.884147782	0.025771171
Myh2	8.416161373	0.02719909
Acta1	9.777444106	0.016851919
2310065F04Rik	18.48034991	0.00723355
Cav3	19.11940832	0.005232615
Eef1a2	23.96702039	0.00013999
Xirp2	25.4350714	2.656E-05
Gm13848	-23.13927738	6.372E-07
Klk1b5	-12.02669382	0.005147109
Gm31497	-9.874301897	0.028507208
Ttc22	-9.789559717	0.026277587
Sowaha	-9.493708605	0.023913406
Gm14130	-9.390506843	0.005232615
Olfr459	-9.237650161	0.005232615
Gm37427	-9.173565658	0.048649149
Dcdc5	-8.802442662	0.017019191
Itprid1	-8.51604231	0.023952601
Gm28401	-8.489791063	0.010983625
Gm18636	-8.451344218	0.019125517
AC132444.6	-8.451305831	0.011094218
Pgr	-8.182130001	0.005232615

Gm21083	-8.136007925	0.017019191
Gm37673	-8.130671855	0.033225513
Gm30251	-8.072061998	0.016851919
Gm42575	-8.06310539	0.016162143
Gm36346	-8.025759187	0.018694338
Fut9	-8.01086766	0.005232615
Slc28a3	-7.995815727	0.018918241
Gm16138	-7.990769404	0.020589312
Ly6g6c	-7.961366638	0.005147109
9130214F15Rik	-7.846888281	0.020589312
1700111E14Rik	-7.806165259	0.044241867
Gm15454	-7.79755515	0.041167779
Klk1	-7.732902952	0.010796781
Gm4963	-7.726482557	0.046568935
Gm43534	-7.713948347	0.020589312
Gm40999	-7.661058887	0.010796781
Prr27	-7.642167321	0.045864383
Gm8439	-7.627393215	0.010983625
Gm36945	-7.583896537	0.024933342
Gm28845	-7.579135703	0.015082811
Gm20515	-7.533033392	0.016895148
Gm48092	-7.524642607	0.016708274
Gm41333	-7.474842916	0.020589312
Acsm1	-7.455464825	0.040871261
Gm32358	-7.446791105	0.011820252
Sval2	-7.441316561	0.043302679
Gm20758	-7.392733666	0.016851919
Mir6362	-7.364901687	0.011193115
Gm26918	-7.236065072	0.010416256
9430085M18Rik	-7.207300793	0.005147109
Gm47832	-7.203717135	0.017727415
Gm37184	-7.122976889	0.034342169
Cftr	-7.121437793	0.005232615
Gm49028	-7.041075532	0.015457445
Klk1b11	-7.026317873	0.024933342
Tcfl5	-6.997771239	0.00962195

Table S1.2 TNCKO TdLNs vs WT TdLNs
(inflammatory and adaptive immune responses)

Gene name	**log2 (FoldChange)**	**padj**
Igkv6-23	2.060094431	0.135716743

Klrc2	1.866847764	0.282105464
Ighv5-16	3.269982074	0.136438119
Trbv13-1	2.087068105	0.18926946
Ighv7-3	3.860142387	0.083803887
C1ra	1.283167598	0.173520807
Emp2	-1.289348725	0.168713276
Batf3	0.317544759	0.886344282
Prdm1	1.117802797	0.217753876
Ighm	1.512306097	0.180492633
Il17f	3.615860703	0.148797525
Ctla4	1.818144921	0.302111123
Cd81	-1.173811793	0.217753876
Havcr2	1.239762723	0.123621124
Clec4a1	1.495769426	0.273799206
Jam3	0.755781065	0.232618652
Igkv3-4	2.590395887	0.131237621
Ighv2-9-1	0.777117541	0.792026673
Igkv3-10	2.755912605	0.093519428
Ighv14-1	3.066337367	0.11500285
Ighv5-9	3.236577544	0.086448295
C1rl	-3.559422562	0.049102116
C1rb	3.747613016	0.082732098
Cd7	1.601309114	0.142197237
Ighv1-72	2.203084167	0.088387379
Igkv6-17	4.397951382	0.024415161
Igkv5-39	2.780336021	0.077892106
Ighv6-3	4.474278246	0.082722342
Ighv1-18	1.772684791	0.167513685
Ighv1-61	1.900667592	0.295995218
Trav12-2	2.605275765	0.206580636
Ifnk	-1.182059361	0.308141746
Clec4n	3.508842111	0.022263943
Rora	-1.226237066	0.214615554
Ighv1-69	2.369196343	0.146445523
Fcer1g	1.156495434	0.130809238
Igkv4-72	2.969074859	0.085418535
Treml4	2.027479001	0.157426935
Nedd4	-1.443508712	0.172934123
Igkv6-25	3.377964341	0.031061075
Raet1e	-1.755473963	0.199252937
Jag1	-0.890201081	0.286109368

Myd88	0.57070605	0.205105788
Ighv1-76	1.738478548	0.114460061
Il18bp	0.1637887	0.876742243
Nlrp10	1.727264582	0.162633934
Ighv1-58	3.856734247	0.017357758
C1qa	1.302911915	0.172730554
Igkc	2.71812945	0.067504255
Trbv20	1.724837589	0.311617314
C1s2	-2.015236263	0.30966936
Ighv1-47	2.351233196	0.178322674
Rnf125	1.143583988	0.220300129
Igkv12-38	3.54323699	0.134403591
C6	2.622346623	0.196495141
Ighv5-6	2.350470303	0.117085389
Igkv16-104	2.657092932	0.100276052
Ighv1-78	2.058015783	0.31168129
Igkv6-32	1.533086997	0.213386109
C1qc	1.610577595	0.077429026
Ighv2-5	2.81743118	0.053273658
Igkv3-5	2.097423952	0.121760633
Otub1	0.336445094	0.26570892
Igkv10-94	3.317565048	0.046705107
H2-Aa	0.961139711	0.279684189
Ighv9-1	3.237979016	0.160321272
Ighv14-4	2.030219047	0.11921615
C3	1.516298903	0.116210434
Ighv9-3	3.998069033	0.038844683
Entpd7	-1.308662757	0.067858687
Igkv9-120	3.156997628	0.03396288
Ighv1-19	2.715117067	0.165101291
Mb	2.834808849	0.241950982
Cracr2a	-1.921282414	0.097918084
Ighv1-22	2.850804887	0.067918715
Igkv2-137	3.110738031	0.137216543
Trbv5	2.090686879	0.288707442
Igkv10-96	3.242494261	0.036807815
Ung	-0.939395383	0.29851765
Igkv1-117	2.737634802	0.138936856
Igkv2-109	2.58980865	0.106607565
Igkv4-74	2.344448715	0.232929953
Trgv2	2.04184972	0.283267467

Igkv14-100	2.784154149	0.169827859
Igkv8-24	4.072872704	0.124535813
Trpm4	-1.700837765	0.109265022
Igkv13-85	3.211007478	0.168227914
Igkv8-21	2.103661668	0.185050714
Mcoln2	0.98925485	0.199029178
Gm12990	3.015204482	0.168227914
Cd4	1.257127706	0.267522615
Trav16	1.486249795	0.267522615
C1qb	1.333626464	0.181349428
Jchain	1.936710012	0.158551673
Clec4a2	2.31221991	0.168138186
Gzmb	2.251607353	0.264571985
Ighv1-11	2.383967925	0.260406932
Marchf8	-1.520047271	0.275550236
Ighv10-1	3.293828605	0.047130474
Tarm1	2.093582267	0.223227068
Ighv3-8	2.437131225	0.145282657
Ighv5-9-1	2.099033256	0.253629053
Mpeg1	1.205405468	0.176950538
Mfsd6	-1.886789909	0.098112064
Pdcd1lg2	1.395987723	0.138129283
Trbv19	2.270866541	0.263535227
Ighv3-5	4.696108866	0.054468986
Ighg2c	4.430442467	0.023281198
Ighv1-81	2.730974426	0.07793831
Iglc2	1.373875467	0.231326066
Anxa1	-1.601583217	0.272783014
Serpinb9b	2.669977269	0.258023492
Ifng	3.267871042	0.287667569
Ighv1-66	2.747434728	0.205398723
Ifnar1	0.518456796	0.512411322
Ifnar2	0.12403608	0.86142948
Fam114a1	-1.362696967	0.130809238
Slc7a2	-3.910718134	0.050873476
Vnn1	-4.447793763	0.06023864
Pomgnt1	-1.251934423	0.075066604
Lrrc25	1.353640206	0.171402892
Tyrobp	0.964393663	0.221776837
Csf1r	1.134204787	0.131237621
Ccl7	2.84628275	0.165431132

Il17f	3.615860703	0.148797525
Pla2g3	-2.409834618	0.106750796
Casp7	-1.289799404	0.126832892
Cd68	0.7911457	0.240992906
Havcr2	1.239762723	0.123621124
Jam3	0.755781065	0.232618652
Cxcl9	2.426840578	0.258023492
Mal	-5.351686848	0.177571444
Chia1	-6.777023819	0.041735252
Mefv	1.791724776	0.177761923
Nupr1	-3.790631422	0.022263943
Saa3	4.423792357	0.150330847
Gnat2	-2.122885708	0.041167779
Smpdl3b	-3.166037305	0.053611748
Il23r	1.674024279	0.202241438
Nfix	-2.438962849	0.082567316
Agt	-5.093882591	0.118546845
Tlr2	0.935904281	0.258835596
Hpse	1.213543218	0.20188904
Serpinb1a	0.994210409	0.199029178
Il17rc	-1.596305852	0.169682616
Fcer1g	1.156495434	0.130809238
Serpina1b	1.698154699	0.207834507
Egfr	-1.315420633	0.299173238
Vcam1	1.135584218	0.268600145
Cxcr2	2.05190639	0.205398723
Ufl1	-0.93943122	0.172934123
Hyal1	-1.911807295	0.158428994
Myd88	0.57070605	0.205105788
Il31ra	2.37706897	0.161180117
Il18bp	0.1637887	0.876742243
Nlrp10	1.727264582	0.162633934
Pla2g2d	1.407508699	0.231936063
C1qa	1.302911915	0.172730554
Pla2g7	-2.2862543	0.128941532
Cd300a	0.950488387	0.257315141
Gpr15	2.90596576	0.196495141
Naip1	1.511439076	0.120262083
Cybb	1.15739914	0.273634695
Snca	-4.839158665	0.227817618
Nr4a1	-1.454044888	0.106607565

Il34	-2.327650768	0.11392492
Cx3cl1	-1.224048828	0.243899532
Smo	-1.571167724	0.292633837
Scyl1	-0.757954651	0.263535227
Alg3	-0.927808463	0.133945962
C3	1.516298903	0.116210434
Gna14	-1.161605622	0.190414485
Cebpb	-1.531873815	0.206411395
F12	1.647153187	0.159552467
Casp6	-1.07991334	0.231936063
Zfp941	1.569842874	0.396838823
Adamdec1	2.09160785	0.176617002
Thrb	-2.346395092	0.141931576
Nlrp9b	-5.035607983	0.089565358
Ccl19	2.623513567	0.161869829
Cxcr6	0.834798323	0.297349639
Il1rap	-1.273696765	0.162902192
Tnfrsf1b	1.145111728	0.291730891
Hmox1	1.702187244	0.171384835
Ifngr1	1.06058828	0.121462981
Il17re	-3.502028678	0.037380691
F2r	1.457635002	0.197353699
Elf3	-5.897147654	0.072593349
Pbxip1	-0.679991313	0.291788747
Serpina3n	2.276323533	0.196495141
Tfrc	-0.782547264	0.189101402
P2rx1	2.034831103	0.242835458
Pomt2	-1.197256333	0.20218044
Ccl12	2.72440139	0.086193977
Slc11a1	0.895556229	0.300768831
Odam	-6.741045436	0.022644205
P2rx7	-0.876566399	0.299048232
Epha2	-3.095428975	0.038241923
Gzmb	2.251607353	0.264571985
Cxcl10	1.924662327	0.106607565
Ptgir	0.930924666	0.089651665
Stk39	-2.366996113	0.046153392
Ccl3	2.584398254	0.220464882
Dab2ip	-1.64576505	0.249601881
Klk1b11	-7.026317873	0.024933342
Ano6	0.294258285	0.302612534

Il17d	-4.630830233	0.022133015
Adcy8	-6.275325056	0.0248165
Ccl28	-5.007994902	0.055174806
Lats1	-0.446218866	0.261434459
Mavs	-0.900345363	0.234608387
Cp	0.945395994	0.287631157
Zdhhc15	1.014823087	0.547153666
Il1f5	-4.408381039	0.212470217
Cmtm4	-2.353648446	0.085432396
Kit	-1.974174656	0.130146244
Anxa1	-1.601583217	0.272783014
Alox5ap	1.245170203	0.175944393
Casp3	1.15352974	0.167448857
F8	1.390147618	0.070274968
Zeb2	0.685861352	0.258003473
Ifng	3.267871042	0.287667569
Itgam	1.709764278	0.115313718

Table S2 Differential gene expression in WT FRCs in comparison to TNCKO FRCs

Expression and p values of the genes differentialy expressed in WT FRCs in comparison to TNCKO FRCs as determined by RNA sequencing analysis with p value < 0.05. Data are deposited at the EMBL-EBI ArrayExrpress archive (accession no E-MTAB-14801).

Gene name	**log2 (FoldChange)**	**padj**
Pdpn	0.9066	0.32465967
Ccl21 (Ckb9)	0.918584905	0.602453789
Vcam1	0.34537292	0.7461508
Col6a1	1.70150337	0.109207083
Ccl19 (Ckb11)	0.293943055	0,613416044
Col1a2	0.683499388	0.933790068
Col1a1	0.405388035	0.574245747
Acta2	0.788261593	0.533430249
Ltbr	0.202147496	0.831079757
Icam1	-6.021832898	0.002841558
Il7	-2.625790363	0.295134076
Igfbp4	-1.245117066	0.29552561
Il7	-2.625790363	0.295134076
Cxcl10	-6.772976388	0.236006461
Cxcl1	-0.570922899	0.945824603
Cxcl16	-2.715864475	0.521381362

Tgfb2	-0.242581639	0.94255552
Ccl5	-2.022505602	0.432339941
Il15	-2.969866695	0.287998067
Il6	-0.265916546	0.968089207
Igfbp3	-2.139929297	0.502956655
Ccl27a	-1.320227028	0.310626853
Il33	-4.21210021	0.006072829
Crp	-0.159696707	0.976510675
Tnfa (Tnfsf2)	-1.681406034	0.829677164
Il34	-0.119826095	0.976510675
Ccl25	-0.018259794	0.992838044
Il16	0.144489022	0.975575439
Ccl9	4.464008769	0.051145251
Ccl2	0.003586239	0.999307763
Hgf	1.048730604	0.646667667
Vegfa	0.960713505	0.345126123
Cxcl14	9.684574217	0.132596255
Adipoq	26.28602822	1.61e-10
Ccl7	1.430097504	0.528721404
Tgfb1	1.084297453	0.354767505
Ccl8	3.763700754	0.185308077
Tgfbi	3.625251642	0.152086568
Cxcl12	0.301928787	0.916853433
Lgals9	-0.752434186	0.288990611
Eif2ak2	-1.360615552	0.094921087
F2rl1	-3.841659033	0.023169835
Tlr2	-1.390095548	0.321701722
Egf1	-1,960461286	0.121843013
Ccl5	-2.022505602	0.432339941
Epha2	-1.051348615	0.17436972
Il33	-4.21210021	0.006072829
Cd24a	-8.255105481	0.001743409
Il7	-2.625790363	0.295134076
Tlr3	-2.556072186	0.020666461
Wnt5a	0.392162701	0.399524647
Csf1r	1.405081728	0.159563197
Apod	3.218643081	0.05747062
Snai2	0.638650028	0.355213351
Ffar2	1.933807649	0.32465967
Il17ra	0.799270997	0.15901213
Twist1	1.276393849	0.239292064
Adipoq	26.28602822	1.61e-10
Il1rl1	4.214144229	0.05747062

Lpl	3.161434253	0.089168476
Rel	-1.025996838	0.378344336
Isg15	-3.295043876	0.009973609
Irf7	-4.982330684	0.012718103
Stoml2	-0.857129051	0.301717494
Txk	-1.754646539	0.181038613
Spn	-2.734786632	0.009973609
Inava	-2.059321604	0.015493105
Runx3	-3.234719567	0.175944291
Gadd45b	-0.744995599	0.440039021
Lyn	-0.760310299	0.379913438
Kit	-8.642351023	0.160778438
Pcsk5	-4.116269896	0.048680318
Gbp5	-3.990967972	0.01938699
Tnfaip8	-1.341020009	0.382772181
F2rl1	-3.841659033	0.023169835
Trex1	-2.289907425	0.066002196
Rgcc	-4.221250551	0.148330764
Casp1	6.958609484	0.407489104
Fabp4	5.152788419	0.092264898
Kat2a	-0.807567863	0.367133179
Nod1	-1.682933597	0.090534737
Gata3	1.431834337	0.265647885
Irf9	1.627592456	0.079488545
Ephb6	3.389544468	0.031818849
Tlr2	1.390095548	0.321701722
Gpam	0.621859639	0.257674652
Zbtb7b	0.629449632	0.210136474
Cd59a	0.833568431	0.298280029
Gas6	2.285046779	0.343951042
Cd36	8.263129481	0.031025652
Agt	3.286630024	0.151014761

Table S3 Differential protein expression in FRCs in dependence of TNC and IR

Expression and p values of the proteins differentially expressed in WT FRCs in comparison to TNCKO FRCs and in dependence of IR as determined by mass spec analysis with p value < 0.05. Data are deposited at the EMBL-EBI ArrayExrpress archive (accession no at the PRIDE partner repository with the dataset identifier PXD060164).

Table S3.1 FRC WT NIR vs FRC TNCKO NIR

Gene name	logFC	P_Value
Nid1	1.25655397	0.0087878
Col5a1	4.82	1.54934E-09
Ero1a	3.49	4.15E-10
Cav1	2.25	7.36E-09
Eng	5.19	4.43811E-13
Lgals3	2.10262835	0.01426803
Adamts2	1.4	0.00104054
Col1a2	9.64	3.85E-15
Pdgfra	4.33	1.31E-07
Col12a1	2.3405077	0.03486441
P3h4	5.58	1.50E-11
Loxl3	3.3	1.41E-10
Mmp14	4.46	8.44E-10
Crtap	2.05	4.65E-07
Serpinh1	0.9	8.07E-06
Lox	3.64	4.22E-11
Col15a1	4.02	2.48E-05
Postn	6.66	4.79E-14
Mmp11	5.07	3.99E-14
Ddr2	6.92	2.01E-16
Hsd17b1	3.23	1.96251E-09
Flot1	0.211636	0.32368855
P3h1	3.28	4.77E-05
Cav2	1.99	0.00107278
Mmp2	7.01	4.96E-16
Aplp2	0.40334582	0.32726395
Myo1e	2.66	2.93E-06
Efemp2	4.1	3.13E-07
P4ha1	2.02	1.40E-09
Tcp1	-0.53139757	0.00514761
Col8a1	-0.35479269	0.05696238
Col14a1	-4.6356	4.01957E-10

Flrt2	-4.7238	2.55639E-11
Kpna1	1,3843	1.86893E-06
Larp1	1.03481161	0.0202512
Pafah1b1	0.22793755	0.31247988
Cops2	0.29835892	0.28276225
Rps6	1.16	8.83E-05
Gstp1	0.75	0.00231166
Gnb1	0.72801585	0.02311979
Prdx1	0.68	0.00216506
Prkcd	3.65	4.35E-08
Cdk1	2.84	3.27E-05
Impdh2	1.28	5.77E-05
Gnl3	1.43	0.00466183
Epha2	1.92	0.0002052
Purb	4.91	6.52E-09
Gba	3.02	2.11E-11
Ythdf2	2.39	1.30E-08
Gnai2	0.57	0.00052856
Mvp	1.51	2.46E-06
Txnrd1	1.64	2.71E-05
Stat6	1.52	0.00038429
Prpf19	1.28	6.04E-06
Pes1	2.09	0.00056149
Fubp1	2.67	5.46E-07
Cdk5rap3	2.27	1.23E-05
Mcm7	2.76	1.39E-07
Cxcl12	3.77	8.35E-09
Psmg1	1.28	0.0002308
Smad1	0.4619	0.004599501
Ccn3	3.34	0.00018798
Etv6	3.92	8.92E-12
Otud6b	1.2159	0.001648941
Prkar1a	0.36004737	0.27482184
Serpinb1a	2.59	6.17E-08
Bysl	0.37859199	0.43220622
Prdx2	1.73	6.12E-08
Pura	1.59	1.63E-06
Yme1l1	1.60368809	0.03843443
Dlg1	3.83	1.59E-07
Dab2	1.0799	0,004384278
Lipa	3.19	1.74E-06

Lrp1	4.94	1.06E-06
Ncstn	0.7	0.00032801
Cd151	-2.19	1.86E-06
Kif1a	1.31	0.00052711
Larp7	-0.83554952	0.01131989
Ddr3	-6.92	2.01E-16
Sidt2	-1.07	0.00013116
Pdgfrb	-2.45099623	0.04332009
Npr3	-3.28	2.98813E-09
Dbn1	-1.06	1.34E-05
Hprt1	-3	4.74E-07
Plxnb2	-1.84	4.24E-07
Serpinh1	0.9	8.07E-06
Ddr2	6.92	2.01E-16
Crtap	2.05	4.65E-07
Col5a1	4.82	1.55E-09
Adamts2	1.4	0.00104054
P4ha1	2.02	1.40E-09
Strap	1.33	0.00048527
Vasn	1.2187029	0.03107797
Lox	3.64	4.22E-11
Tcp1	0.53139757	0.00514761
Hsp90aa1	0,65	0,001119881
Tgfb2	1.3	8.04E-05
Fbn1	1.45	0.00033005
Cav1	2.25	7.36E-09
Htra1	2.27	3,19698E-09
Cd109	4.98	3.54E-10
Thbs1	8.67	4.93E-16
Got1	2.77	1.53E-08
Dnm2	0.00575385	0.97626355
Itga3	-6.89	2.01877E-12
Mpp5	-1.09	0.00189969
Snx1	-1.24019313	0.03143405

Table S3.2. FRC WT IR vs NIR

Gene name	logFC	P Value
Rhoa	0.46734991	0.40846868
Vkorc1	0.96389137	0.09372388

Gnb1	0.24066404	0.53679014
Ndufs4	0.93630231	0.2190456
Fam162a	1.65	0.00907001
Macrod1	0.2154367	0.72553395
Rpl30	1.46	0.00678679
Stxbp1	0.2105802	0.73203121
Cdk5 (Crk6)	0.58329804	0.62984251
Samhd1	0.25734939	0.77848329
Ddx21	0.71508945	0.02805155
Mcm6	1.85	3.33E-05
Rps19	2.29	5.35E-06
Cxcl12	1.42	0.0001391
Mif	2.54	0.00037409
Hmgb1	3.42	1.15E-07
Mrps27	1.03	0.000254888
Mcm3	2.12	9.98E-05
Mcm5	1.63	1.52E-05
Zyx	1	0.00076839
Mcm4	2.47	5.63E-07
Asns	1.44	0.00020161
Clec2d	1.79	1.16E-06
Nono	0.06215871	0.76066853
Pdgfrb	0.26941214	0.28954524
Colec12	1.16	0.00040782
F3	2.01	0.00010822
Mgst1	0.00679346	0.96363743
Sod2	0.5502238	0.0173167
Ube2n	2.67	0.00015748
Rbm14	0.77684232	0.02965056
C1qbp	0.38614221	0.08233306
Cdc42	1.07	2.32E-05
Col3a1	4.28	2.96E-07
Dnaja2	0.66293194	0.05529391
Gstp1	1.01	5.90E-05
Rbm3	1.2	0.00240381
Sqstm1	0.81	0.00188574
Cfl1	1.18	0.00128202
Prdx1	0.93	0.00081993
Mapk1	1.31	0.00226913
Rac1	1.22515284	0.0265266
Prdx5	3,67	8.091E-06

Ipo7	1.13	0.00081783
Dbi	1.57	0.00054805
Sec61b	2.88	0.00037676
Cnpy3	2.26	0.00048108
Cst3	2.62	1.76E-06
Oxsr1	1.39	0.00011428
Hsp90aa1	0.96	8.08E-05
Hsp90ab1	0.7	0.00095471
Dpysl3	1.07	0.00014194
Otub1	1.38	0.00095902
Spr	1.64	0.00056102
Mcm7	3	1.77E-09
Ubqln2	1.17	2.02E-05
Pcna	2.94	8.74E-05
Lox	0.76	0.00016952
Uba1	0.81	0.00035936
Ddx3x	2.4	6.00E-06
Ywhaz	1.05	2.81E-05
Ide	0.82	0.000254359
Mcm2	1.83	7.99E-05
Cnn2	1.67	0.00033997
Ggt5	3.16	0.000490244
Hnrnpd	1.29	0.000387103
Dpep1	1.55	0.00051699
Irgm1	-0.98	0.00081527
Epha2	-1.98	6.39E-05
Serpinb1a	-1.05	0.00014934
Poldip2	-1.18	0.00300716
Tapbp	-2.06	0.000448726
Tap1	-1.7	1.76E-06
Aldh3a2	-1.37	1.73E-06
Ptprz1 (Hptpz)	0.59	0.003400374
Fth1	0.38173893	0.07945144
Gstp1	1.01	5.90E-05
Rps3a	0,72	0.004536503
Sod2	1.27	0.000105348
Mif	2.54	0.00037409
Tkt	1.17	4.65E-05
Ndufs4	0.93630231	0.2190456
Pdgfrb	0.26941214	0.28954524
Serpine1	-0.29698804	0.15042892

B4galt7	-1	0.00015715
Tcp1	0.63	0.00490854
Tkt	1.17	4.65E-05
Crtap	-0.13765949	0.56691166
P3h4	0.18826537	0.57238582
Flot1	-0.25129768	0.18833448
Postn	0.64	0.00094707
Ddr2	0.63	0.00345901
Serpinh1	0.02466483	0.86378546
Lox	0.76	0.00016952
P4ha1	0.08733152	0.55827607
Ero1a	0.0696698	0.64698749
Mmp14	0.54291001	0.01461059
Mmp11	1.44364716	0.01980396
Lgals3	0.58058339	0.04068826
Mmp2	0.49	0.00901394
Col1a2	0.7	0.00493934
Tnc	0.356591	0.51340939
Cav1	0.13695505	0.3727634
Myo1e	0.33974737	0.47637916
Loxl2	0.35445031	0.22989815
P3h1	0.54043408	0.13121827
Nid1	0.06380708	0.82801393
Col5a1	0.617897	0.11556653
Emilin1	0.11354898	0.72112982
Col1a1	0.84245017	0.0347062
Col15a1	0.07897689	0.90820059
Col12a1	0.28945392	0.72305869
Pdgfra	0.85791672	0.08353464
Ccn2	0.30836172	0.55568145
Col8a1	0.31532387	0.06394914
Efemp2	-0.12619315	0.72648919
Loxl3	-0.46876663	0.0338956
Stxbp1 (Munc18-1)	-0.51	0.001813249
Acsl1	0.33769687	0.24409524
Bcat2	0.08054628	0.6601347
F3	2.01	0.00010822
Csnk2b	1.84	0.00556816
Hmgb1	3.42	1.15E-07
Il6st	1.84	8.56E-05
Mcm2	1.83	7.99E-05

Rpl3	1.02	0.00017467
Oxsr1	1.39	0.00011428
Hsp90ab	0.70	0.000954713
Zyx	1	0.00076839
Stip1	1.01	0.00032317
Tfrc	1.62	0.00066124
Lox	0.76	0.00016952
Cdc42	1.07	2.32E-05
Col3a1	4.28	2.96E-07
Ybx1	0.299501	0.08671835
Mapk1	1.31	0.00226913
Impdh2	2.11	0.00019303
Cfl1	1.18	0.00128202
Rplp0	0.95	2.18E-05
Fkbp1a	2.01	0.00019824
Cxcl12	1.42	0.0001391
Ubtf	1.21	0.00020596
Cacybp	1.44	0.00025378
Eef1e1	2.59	3.65796E-07
Serpine1	0.29698804	0.15042892
Asah1	0.32301578	0.08570793
Irgm1	-0.98	0.00081527
Mapk1	1.31	0.00226913
Rac1	1.22515284	0.0265266
Cxcl12	1.42	0.0001391
C1qbp	0.38614221	0.08233306
Thy1	1.25	4.76E-05
Mif	2.54	0.00037409
Cd99 (Mic2)	1.14	0.00479148
Oxsr1	1.39	0.00011428
Swap70	2.48	1.14E-06
Spr	1.64	0.00056102
Serpine1	0.29698804	0.15042892
Mpp1	0.41102678	0.12788852
Ano6	-0.30183702	0.32596197

Table S3.3 FRC WT IR vs FRC TNCKO IR

Gene name	**logFC**	**P Value**
Sfrp1	-4.17	2.48E-10

Isg15	-2.79	5.26E-05
Bcat2	-2.21	1.43E-07
Tollip	-1.65	3.20E-05
Gsn	-0.71	0.00511165
Myo1c	-0.45	0.00416351
Asah1	-1.73	4.24E-07
Cxcl12	2.07	1.48E-09
Bclaf1	3.07	2.62E-06
Ctbp2	2.31	2.42E-05
Gas6	0.42	0.49199572
Zc3h15	1.37	0.00014258
Cdk9	0.98	2.34279E-05
Entpd2	1.74	4.73E-08
Rpl3	1.62	1.08E-05
Mcm2	5.47	2.02E-09
Hsp90ab1	0.85	0.000549904
Ifi204	1.29	0.001341586
Dapk3	1.21	5.72E-05
Smarca5	4.33	2.13E-06
Kars1	1.01	0.00029804
Gba	3.09	5.00E-10
Lox	2.81	5.73E-10
Rplp0	0.37	0.03344401
Actn4	0.75	0.00033299
Srsf3	0.08	0.9225257
Dbn1	0.69	0.00306163
Rps3	1.07	3.29E-05
Upf1	2.27	3.30E-08
Ncl	1.07	1.94E-05
Tfrc	4.97	8.75E-10
Mapk1	0.25	0.57796411
Atic	1.4	8.79E-05
Oxsr1	1.98	1.49E-06
Ifitm3	0.12	0.84266258
Alad	3.32	3.31879E-09
Trex1	1.85	7.21264E-05
Tgtp1	3.51	1.57573E-07
Stat2	1.90	2.89369E-06
Il1rap	2.92	5.92E-10
Ybx3	2.05	5.10E-07
Crkl	0.21	0.46948913

Sting1	0.63	0.0058375
Ybx1	1.66	9.06E-08
Irgm1	0.09	0.55491096
Erbin	2.48	1.95E-09
Ndufa13	2.37	0.00025289
Adar	1.94	1.27252E-05
Stat1	3.6	1.91E-09
Nmi	4.51	8.76759E-13
Iigp1	6.99	1.0626E-15
Ifit1	2.46	0.00043826
Pml	1.03	0.00025181
Eef1e1	1.08	1.90E-05
Jak1	3.67	1.23E-09
Nrp2	2.73	9.21E-05
Prkca	1.40	0.004123093
Ifit3	3.97	1.93896E-10
Impdh2	2.85	1.35E-05
Syncrip	2.11	4.93E-08
Eif4a2	1.89	0.00081529
Kif5b	1.94	3.21E-05
Gbp2	3,59	5.41146E-10
Anxa1	1.99	7.86E-08
Oas2	1.08	0.002870635
Usp10	1.47	3.92E-05
Gbp4	2.85	2.2778E-07
Ifit2	2.50	4.48639E-05
Smpd4	0.83515082	0.0484886
Zyx	2.47	6.25526E-09
Eif2ak2	2.54	2.44E-08
Stip1	1.17	0.00013831
Mat2a	0.86455759	0.00852482
Cacybp	1.85	5.31E-05
Flnb	1.65	0.00154126
Cad	0.90304897	0.04147857
Eprs1	0.65507942	0.11847934
Pdia3	0.76	8.25E-05
Rab12	-1.84	0.00015204
Rab11fip5	0.42915921	0.38414977
Ggt7	0.78455726	0.30103674
Shmt2	0.85	5.70E-05
Cox6a1	-2.80	0.000346801

Ndufa8	-0.54791588	0.03381228
Sco2	-3,67	2.15765E-06
Mtnd2	-0.54	0.004140451
Cycs	-0.71834406	0.01427243
Ndufc2	-0.101576	0.61944516
Cox5a	1.25305346	0.0345687
Mdh1	-1.83272413	0.00825116
Mybbp1a	-1.98751495	0.01258872
Adsl	-1.8	0.00035699
Aco1	-2.42	3.78E-07
Dlst	-0.42209797	0.04243473
Idh2	-0.67	0.00041874
Sdha	-0.08887283	0.52308894
Suclg1	0.88	0.00012556
Cat	-1.44	1.07E-05
Sucla2	0.95	8.62E-05
Slc37a2	0.87	0.00072168
Ndufb6	1.07049324	0.01579918
Cav1	1.66	1.09E-06
Ero1a	3.45	1.04E-09
Col1a2	8.66	2.08E-17
Lox	2.81	5.73E-10
Serpinh1	0.69	0.00013058
Flot1	0.03163443	0.87938753
P3h4	5.11	3.95E-11
Mmp14	3.86	7.80E-07
Crtap	2.54	3.02E-06
Ccn2	3.06	9.17E-07
Ddr2	6.01	4.83E-14
Tnc	2.92	1.37E-05
P3h1	3.8	1.45E-05
Mmp11	3.35	3.64E-05
Lgals3	2.31	0.0016581
Pdgfra	3.19	1.81E-08
Col15a1	3.66	4.32E-08
Col12a1	1.12907197	0.10516776
Nid1	0.82	0.00415414
Col5a1	3.92	1.01E-09
Eng	5.56	3.57023E-14
Loxl3	3.48	2.86E-12
Emilin1	5.01	5.47E-13

Postn	5.32	5.27E-12
Mmp2	6.24	8.37E-15
Tkt	1.69	5.84E-07
Efemp2	4.21	3.60E-13
Myo1e	2.13	0.0002141
Col1a1	0,98	1.98
Tcp1	-0.74	0.00244475
Col8a1	-0.41761062	0.02041826
Flrt2	-4.81	1.73763E-12
Loxl2	-1.15	1.87508E-05
Col14a1	-4.33	1.55902E-09
Ccn1	-1.91	0.002536102
P4ha1	0,60	0.002285728

Table S4 Cox regression analysis for HNSCC RT cohort (TNC-high)

Parameters	n (%) mean (SD)/median (IQR)	Univariate p value	Hazard Ratio (HR)	LowerCI	HigherCI	Multivariate p value	HR	LowerCI	HigherCI
TNC	148.69 (96.55-236.61)	0.617	1	0.999	1.002				
PDPN	48.88 (32.81-72.61)	0.886	0.999	0.991	1.008				
CCL21	15.86 (5.52-46.34)	0.507	1.001	0.998	1.004				
CCL19	4.33 (1.47-12.15)	0.416	1.002	0.998	1.005				
VCAM1	2.25 (0.99-5.33)	0.941	0.999	0.981	1.018				
COL1A1	523.04 (243.87-1328.81)	0.571	1	1	1				
COL6A1	158.45 (82.59-291.30)	0.511	0.999	0.998	1.001				
ACTA2	11.45 (6.15-21.51)	0.258	1.006	0.995	1.018				
LTBR	29.00 (24.07-36.54)	0.586	0.994	0.972	1.016				
Age	59 (51-67)	0.287	1.015	0.988	1.042				
Gender									
Male	104 (78.20)		ref						
Female	29 (21.80)	0.939	0.973	0.482	1.966				
Tabacco amount									
0	1 (0.75)		ref						
1	26 (19.55)	0.912	7608.951	0	1.11E+73				
2	52 (39.10)		13494.747	0	1.97E+73				
3	16 (12.03)		8361.312	0	1.22E+73				
4	37 (27.82)		17518.341	0	2.56E+73				
5	1 (0.75)		1.433	0	2.08E+150				
Grade									
1	14 (10.53)		ref						
2	76 (57.14)	0.206	2.529	0.6	10.656				
3	38 (28.57)	0.189	2.689	0.615	11.758				

4	2 (1.50)	0.979	0	0	0
x	3 (2.26)	0.434	2.611	0.236	28.83
Pathological stage					
1	5 (3.76)		ref		
2	8 (6.01)	0.903	3762.336	0	2.33E+61
3	17 (12.78)	0.895	7894.013	0	4.87E+61
4a	83 (62.41)	0.893	9023.291	0	5.55E+61
4b	3 (2.26)	0.883	22340.409	0	1.38E+62
x	17 (12.78)	0.885	625.184	0	1.09E+62

(continued)

Clinical stage					
1	2 (1.50)		ref		
2	14 (10.53)	0.919	1417.294	0	3.71E+63
3	21 (15.79)	0.911	2765.219	0	7.22E+63
4a	86 (64.66)	0.907	3840.715	0	1.00E+64
4b	3 (2.26)	0.909	3374.122	0	8.91E+63
4c	3 (2.26)	0.908	3658.352	0	9.66E+63
x	4 (3.01)	1	0.996	0	1.96E+72
T stage					
1	11 (8.27)		ref		
2	25 (18.80)	0.311	2.963	0.362	24.269
3	32 (24.06)	0.161	4.299	0.56	33.013
4	4 (3.01)	0.476	2.744	0.171	43.94
4a	43 (32.33)	0.19	3.875	0.51	29.415
4b	2 (1.50)	0.034	13.583	1.223	150.824
x	16 (12.03)	0.056	7.585	0.948	60.699
N stage					
0	35 (26.32)		ref		
1	14 (10.53)	0.876	1.114	0.287	4.318

2	3 (2.26)	0.595	1.767	0.217	14.414				
2a	2 (1.50)	0.317	2.916	0.358	23.778				
2b	41 (30.83)	0.102	2.112	0.863	5.169				
2c	18 (13.53)	0.001	4.824	1.858	12.527				
3	1 (0.75)	0.977	0	0	2.49E+281				
x	19 (14.29)	0.103	2.347	0.841	6.554				
Alcohol history									
Never	33 (24.81)		ref						
Yes	100 (75.19)	0.286	1.488	0.717	3.088				
FRC marker						0.042			
Low	66 (49.62)		ref				ref		
High	67 (50.38)	0.042	1.863	1.022	3.395	0.042	1.86	1.022	3.395

Table S5 p values

Main Figures		
Figure	**Group**	**p value**
1A	WT vs KO	0.0181
	WT NIR vs WT IR	0.037
	KO NIR vs KO IR	0.9985
	WT NIR vs KO IR	0.0257
	WT IR vs KO IR	0.9981
1C	WT vs KO	>0.9999
	WT NIR vs WT IR	0.001
	KO NIR vs KO IR	>0.9999
	WT IR vs KO IR	0.9379
1D	WT vs KO	<0.0001
	WT NIR vs WT IR	0.0436
	KO NIR vs KO IR	0.9959
	WT IR vs KO IR	<0.0001
1E	WT vs KO	0.048
	WT NIR vs WT IR	0.0246
	KO NIR vs KO IR	0.9996
	WT IR vs KO IR	0.0465
1F	WT vs KO	<0.0001
	WT NIR vs WT IR	0.0594
	KO NIR vs KO IR	0.9863
	WT IR vs KO IR	<0.0001
1G	WT vs KO	0.0272
	WT NIR vs WT IR	0.0111
	KO NIR vs KO IR	>0.9999
	WT IR vs KO IR	<0.0001
1H	WT vs KO	<0.0001
	WT NIR vs WT IR	0.0055
	KO NIR vs KO IR	0.9851
	WT IR vs KO IR	<0.0001
1K	WT vs KO (B220)	0.0159
	WT vs KO (CD3)	0.0317
2F	WT Ctrl vs WT + TNC	0.0004
	WT Ctrl vs KO Ctrl	0.0012
	WT + TNC vs KO + TNC	0.507
	KO Ctrl vs KO + TNC	0.8945

3B	WT vs KO	<0.0001
3D	WT vs KO	0.0486
	WT NIR vs WT IR	0.5147
	KO NIR vs KO IR	0.9935
	WT IR vs KO IR	0.275
3F	WT vs KO	<0.0001
	WT vs WT + α- CCR7	<0.0001
	WT vs WT + Nb3	0.0002
	WT vs WT IR	0.0001
	WT IR vs KO IR	<0.0001
	WT IR vs WT IR + α-CCR7	<0.0001
	WT IR vs WT IR + Nb3	<0.0001
3G	No FBS NIR vs TGFβ NIR	<0.0001
	No FBS NIR vs OSCC-CM NIR	<0.0001
	No FBS NIR vs OSCC-CM/GW NIR	0.4003
	OSCC-CM NIR vs OSCC-CM/GW NIR	<0.0001
	No FBS IR vs TGFβ IR	<0.0001
	No FBS IR vs OSCC-CM IR	0.0001
	No FBS IR vs OSCC-CM/GW IR	0.0002
	OSCC-CM IR vs OSCC-CM/GW IR	<0.0001
	No FBS NIR vs IR	<0.0001
	TGFβ NIR vs IR	<0.0001
	OSCC-CM NIR vs IR	0.0004
	OSCC-CM/GW NIR vs IR	0.999
3H	No FBS NIR vs TGFβ NIR	<0.0001
	No FBS NIR vs OSCC-CM NIR	0.0007
	No FBS NIR vs OSCC-CM/GW NIR	>0.9999
	OSCC-CM NIR vs OSCC-CM/GW NIR	0.0008
	No FBS IR vs TGFβ IR	<0.0001
	No FBS IR vs OSCC-CM IR	0.7623
	No FBS IR vs OSCC-CM/GW IR	<0.0001
	OSCC-CM IR vs OSCC-CM/GW IR	<0.0001
	No FBS NIR vs IR	<0.0001
	TGFβ NIR vs IR	<0.0001
	OSCC-CM NIR vs IR	0.0016
	OSCC-CM/GW NIR vs IR	0.4509
4B	shC NIR vs shT NIR	0.5503
	shC NIR vs KO NIR	0.4654
	shC NIR vs shC IR	<0.0001

	shC NIR vs shT IR	0.7733
	shC NIR vs KO IR	0.9382
4D	shC NIR vs IR	<0.0001
	shT NIR vs IR	0.0677
	KO NIR vs IR	0.0953
4E	shC NIR vs shT NIR	0.6281
	shC NIR vs KO NIR	0.5544
	shC NIR vs shC IR	0.0001
	shC NIR vs shT IR	0.0516
	shC NIR vs KO IR	0.2038
4F	shC NIR vs shT NIR	0.9943
	shC NIR vs KO NIR	0.5666
	shC NIR vs shC IR	<0.0001
	shC NIR vs shT IR	0.0079
	shC NIR vs KO IR	0.1367
4H	NIR vs IR	0.001
	IR vs IR + GW	0.0002
	NIR vs IR+ GW	0.4818
4I	NIR vs IR	0.0002
	IR vs IR + GW	0.0076
	NIR vs IR+ GW	<0.0001
5C	Ccl21 OSCC vs OSCC+ FRC	0.0002
	Ccr7 OSCC vs OSCC+ FRC	<0.0001
	Tgfβ1 OSCC vs OSCC+ FRC	<0.0001
	Il-10 OSCC vs OSCC+ FRC	0.0015
	Il-7 OSCC vs OSCC+ FRC	>0.9999
	Il-17 OSCC vs OSCC+ FRC	0.0012
	Acta2 OSCC vs OSCC+ FRC	<0.0001
	Tnc OSCC vs OSCC+ FRC	0.0011
	Col1a2 OSCC vs OSCC+ FRC	0.0001
	Cd206 OSCC vs OSCC+ FRC	0.9837
	Foxp3 OSCC vs OSCC+ FRC	0.534
	Ctla4 OSCC vs OSCC+ FRC	>0.9999
5D	Day1 OSCC vs OSCC + FRC	>0.9999
	Day1 OSCC vs OSCC + FRC KO	>0.9999
	Day1 OSCC+FRC vs OSCC + FRC KO	>0.9999
	Day8 OSCC vs OSCC + FRC	0.004623929
	Day8 OSCC vs OSCC + FRC KO	0.015315977
	Day8 OSCC+FRC vs OSCC + FRC KO	0.050026019

	Day15 OSCC vs OSCC + FRC	0.000726622
	Day15 OSCC vs OSCC + FRC KO	5.24083E-05
	Day15 OSCC+FRC vs OSCC + FRC KO	0.056366275
	Day18 OSCC vs OSCC + FRC	0.000325007
	Day18 OSCC vs OSCC + FRC KO	0.000836047
	Day18 OSCC+FRC vs OSCC + FRC KO	0.076750028
6B	NIR vs NIR + MP5	0.4786
	NIR vs IR	0.0087
	NIR vs IR + MP5	0.001
	IR vs IR+ MP5	0.0591
6D	NIR vs NIR + MP5	0.0456
	NIR vs IR	0.0039
	NIR vs IR + MP5	0.0011
	IR vs IR+ MP5	0.03
6F	NIR vs IR	0.0021
	NIR vs IR + MP5	0.8608
	IR vs IR+MP5	0.0013
7A	TNC high	0.039
7B	TNC low	0.08
Extended view Figures		
Figure	**Group**	**p value**
EV1B	WT vs KO	0.0366
	WT NIR vs WT IR	0.0055
	KO NIR vs KO IR	0.6333
	WT IR vs KO IR	0.3239
EV1E	WT vs KO	0.0094
	WT NIR vs WT IR	0.6905
	KO NIR vs KO IR	0.9975
	WT IR vs KO IR	0.0006
EV3E	WT vs KO	>0.9999
	WT NIR vs WT IR	0.017
	KO NIR vs KO IR	>0.9999
	WT IR vs KO IR	0.0179
EV1F	WT vs KO	0.067
	WT NIR vs WT IR	0.0127
	KO NIR vs KO IR	0.9241
	WT IR vs KO IR	0.0006
EV1G	WT vs KO	0.0723
	WT NIR vs WT IR	0.0103

	KO NIR vs KO IR	>0.9999
	WT IR vs KO IR	<0.0001
EV3G	No FBS NIR vs TGFβ NIR	<0.0001
	No FBS NIR vs OSCC-CM NIR	<0.0001
	No FBS NIR vs OSCC-CM/GW NIR	0.4538
	OSCC-CM NIR vs OSCC-CM/GW NIR	0.0059
	No FBS IR vs TGFβ IR	<0.0001
	No FBS IR vs OSCC-CM IR	0.8758
	No FBS IR vs OSCC-CM/GW IR	0.0017
	OSCC-CM IR vs OSCC-CM/GW IR	0.0001
	No FBS NIR vs IR	<0.0001
	TGFβ NIR vs IR	0.0004
	OSCC-CM NIR vs IR	0.7653
	OSCC-CM/GW NIR vs IR	>0.9999
EV3H	No FBS NIR vs TGFβ NIR	0.0026
	No FBS NIR vs OSCC-CM NIR	<0.0001
	No FBS NIR vs OSCC-CM/GW NIR	0.0317
	OSCC-CM NIR vs OSCC-CM/GW NIR	0.0042
	No FBS IR vs TGFβ IR	<0.0001
	No FBS IR vs OSCC-CM IR	<0.0001
	No FBS IR vs OSCC-CM/GW IR	0.0023
	OSCC-CM IR vs OSCC-CM/GW IR	<0.0001
	No FBS NIR vs IR	0.0306
	TGFβ NIR vs IR	0.0004
	OSCC-CM NIR vs IR	<0.0001
	OSCC-CM/GW NIR vs IR	0.0021
EV4D	shC NIR vs shT NIR	0.8354
	shC NIR vs KO NIR	0.916
	shC NIR vs shC IR	<0.0001
	shC NIR vs shT IR	0.0011
	shC NIR vs KO IR	0.1521
EV4E	shC NIR vs shT NIR	0.9996
	shC NIR vs KO NIR	0.8909
	shC NIR vs shC IR	<0.0001
	shC NIR vs shT IR	>0.9999
	shC NIR vs KO IR	0.9787
EV4F	shC NIR vs shT NIR	0.982
	shC NIR vs KO NIR	0.9995
	shC NIR vs shC IR	<0.0001

	shC NIR vs shT IR	0.1796
	shC NIR vs KO IR	0.919
EV4H	shC NIR vs shT NIR	>0.9999
	shC NIR vs KO NIR	0.3737
	shC NIR vs shC IR	0.001
	shC NIR vs shT IR	0.8021
	shC NIR vs KO IR	>0.9999
EV4G	shC NIR vs shT NIR	>0.9999
	shC NIR vs KO NIR	>0.9999
	shC NIR vs shC IR	<0.0001
	shC NIR vs shT IR	<0.0001
	shC NIR vs KO IR	0.0003
EV4I	shC NIR vs shT NIR	0.7047
	shC NIR vs KO NIR	0.9898
	shC NIR vs shC IR	<0.0001
	shC NIR vs shT IR	0.985
	shC NIR vs KO IR	0.0816
EV6A	TNC vs MP5	0.0305
	TNC vs Cy5-MP5	0.0255
	MP5 vs Cy5-MP5	0.9873
EV6B	MP5 vs Cy5-MP5	0.1765
Appendix Figures		
Figure	**Group**	**p value**
S1C	WT vs KO	0.4
S1D	WT vs KO	0.6804
	WT NIR vs WT IR	0.1881
	KO NIR vs KO IR	0.9994
	WT IR vs KO IR	0.0325
S1E	WT vs KO	0.0372
	WT NIR vs WT IR	0.7364
	KO NIR vs KO IR	0.2483
	WT IR vs KO IR	0.0022
S1F	WT vs KO	0.9833
	WT NIR vs WT IR	0.0132
	KO NIR vs KO IR	0.9979
	WT IR vs KO IR	0.0143
S1G	WT vs KO	0.9932
	WT NIR vs WT IR	0.0159
	KO NIR vs KO IR	0.9723

	WT IR vs KO IR	0.0023
S1H	WT vs KO	0.0889
	WT NIR vs WT IR	0.0103
	KO NIR vs KO IR	>0.9999
	WT IR vs WT IR	<0.0001
S1I	WT vs KO	0.003
	WT NIR vs WT IR	0.9988
	KO NIR vs KO IR	0.944
	WT IR vs KO IR	0.0032
S1J	WT vs KO	0.1943
	WT NIR vs WT IR	0.0446
	KO NIR vs KO IR	0.0476
	WT IR vs KO IR	0.2159
S1K	WT vs KO	0.9078
	WT NIR vs WT IR	0.9862
	KO NIR vs KO IR	0.0303
	WT IR vs KO IR	0.937
S1L	WT vs KO	0.9852
	WT NIR vs WT IR	0.9123
	KO NIR vs KO IR	0.9998
	WT IR vs KO IR	0.9784
S1M	WT vs KO	0.8857
	WT NIR vs WT IR	0.9796
	KO NIR vs KO IR	0.0214
	WT IR vs KO IR	0.0344
S1N	WT vs KO	0.6906
	WT NIR vs WT IR	0.9987
	KO NIR vs KO IR	0.2132
	WT IR vs KO IR	0.0241
S1O	WT vs KO	0.0779
	WT NIR vs WT IR	0.9511
	KO NIR vs KO IR	0.993
	WT IR vs KO IR	0.2911
S1Q	WT vs KO	0.8874
	WT NIR vs WT IR	0.9611
	KO NIR vs KO IR	0.9957
	WT IR vs KO IR	0.7625
S2E	WT Ctrl vs WT + TNC	<0.0001
	WT Ctrl vs KO Ctrl	<0.0001

	WT + TNC vs KO + TNC	0.8729
	KO Ctrl vs KO + TNC	0.896
S2F	WT vs KO	>0.9999
	WT NIR vs WT IR	0.7805
	KO NIR vs KO IR	0.9871
	WT IR vs KO IR	0.5516
S3B	WT vs KO	0.0706
	WT NIR vs WT IR	<0.0001
	KO NIR vs KO IR	<0.0001
	WT IR vs KO IR	<0.0001
S3J	Lox NIR vs IR	0.228571
	TGM2 NIR vs IR	0.771429
	MMP11 NIR vs IR	0.228571
	MMP2 NIR vs IR	0.771429
	MMP14 NIR vs IR	0.228571
S3K	Lox NIR vs IR	0.002165
	TGM2 NIR vs IR	0.002165
	MMP11 NIR vs IR	0.002165
	MMP2 NIR vs IR	0.002165
	MMP14 NIR vs IR	0.002165
S3M	No FBS FRC WT vs No FBS FRC KO	0.001
	No FBS NIR vs TGFβ NIR	0.0107
	No FBS NIR vs OSCC-CM NIR	0.412
	No FBS NIR vs OSCC-CM/GW NIR	0.9697
	OSCC-CM NIR vs OSCC-CM/GW NIR	0.1989
	No FBS IR vs TGFβ IR	0.1646
	No FBS IR vs OSCC-CM IR	0.3244
	No FBS IR vs OSCC-CM/GW IR	0.1568
	OSCC-CM IR vs OSCC-CM/GW IR	0.9764
	No FBS NIR vs IR	0.0008
	TGFβ NIR vs IR	0.0234
	OSCC-CM NIR vs IR	0.0013
	OSCC-CM/GW NIR vs IR	0.5057
S3N	No FBS FRC WT vs No FBS FRC KO	0.0036
	No FBS NIR vs TGFβ NIR	0.0037
	No FBS NIR vs OSCC-CM NIR	0.4403
	No FBS NIR vs OSCC-CM/GW NIR	0.3818
	OSCC-CM NIR vs OSCC-CM/GW NIR	0.9996
	No FBS IR vs TGFβ IR	0.8587

	No FBS IR vs OSCC-CM IR	0.9069
	No FBS IR vs OSCC-CM/GW IR	0.7934
	OSCC-CM IR vs OSCC-CM/GW IR	0.9945
	No FBS NIR vs IR	0.9142
	TGFβ NIR vs IR	0.1639
	OSCC-CM NIR vs IR	>0.9999
	OSCC-CM/GW NIR vs IR	>0.9999
S3O	No FBS FRC WT vs No FBS FRC KO	0.0009
	No FBS NIR vs TGFβ NIR	<0.0001
	No FBS NIR vs OSCC-CM NIR	0.0321
	No FBS NIR vs OSCC-CM/GW NIR	0.0049
	OSCC-CM NIR vs OSCC-CM/GW NIR	0.9044
	No FBS IR vs TGFβ IR	0.0026
	No FBS IR vs OSCC-CM IR	0.893
	No FBS IR vs OSCC-CM/GW IR	0.9759
	OSCC-CM IR vs OSCC-CM/GW IR	0.677
	No FBS NIR vs IR	0.0004
	TGFβ NIR vs IR	0.0992
	OSCC-CM NIR vs IR	0.1569
	OSCC-CM/GW NIR vs IR	0.9977
S4B	shC vs shT	0.3265
	shC vs KO	0.426
	shT vs KO	0.0472
S4D	WT vs KO	0.023
S4E	GP38 FRC fraction vs OSCC fraction	0.0019
	ITGA7 FRC fraction vs OSCC fraction	<0.0001
	Cdh1 FRC fraction vs OSCC fraction	<0.0001
S4G	shC NIR vs shT NIR	0.5201
	shC NIR vs KO NIR	0.7117
	shC NIR vs shC IR	0.5254
	shC NIR vs shT IR	0.9989
	shC NIR vs KO IR	0.4217
S4H	shC NIR vs shT NIR	0.8761
	shC NIR vs KO NIR	0.9872
	shC NIR vs shC IR	0.9998
	shC NIR vs shT IR	0.999
	shC NIR vs KO IR	0.9805
S4I	shC NIR vs shT NIR	0.9036
	shC NIR vs KO NIR	0.44

	shC NIR vs shC IR	<0.0001
	shC NIR vs shT IR	0.9994
	shC NIR vs KO IR	0.3586
S4J	shC NIR vs shT NIR	>0.9999
	shC NIR vs KO NIR	>0.9999
	shC NIR vs shC IR	0.0001
	shC NIR vs shT IR	0.1102
	shC NIR vs KO IR	0.8838
S4K	shC NIR vs shT NIR	>0.9999
	shC NIR vs KO NIR	0.9998
	shC NIR vs shC IR	0.032
	shC NIR vs shT IR	>0.9999
	shC NIR vs KO IR	>0.9999
S4L	shC NIR vs shT NIR	0.9815
	shC NIR vs KO NIR	0.9897
	shC NIR vs shC IR	0.0002
	shC NIR vs shT IR	>0.9999
	shC NIR vs KO IR	>0.9999
S4M	shC NIR vs shT NIR	0.9979
	shC NIR vs KO NIR	0.9998
	shC NIR vs shC IR	<0.0001
	shC NIR vs shT IR	>0.9999
	shC NIR vs KO IR	>0.9999
S4N	shC NIR vs shT NIR	0.9998
	shC NIR vs KO NIR	>0.9999
	shC NIR vs shC IR	<0.0001
	shC NIR vs shT IR	0.9703
	shC NIR vs KO IR	0.9995
S4O	shC NIR vs shT NIR	>0.9999
	shC NIR vs KO NIR	>0.9999
	shC NIR vs shC IR	<0.0001
	shC NIR vs shT IR	0.2368
	shC NIR vs KO IR	0.1799
S4T (cdh1 oscc mono)	NIR vs IR	0.9997
S4Q (Tgfb1 Oscc mono)	NIR vsIR	0.0096
S4R	NIR vs IR	0.022
S4S	NIR vs IR	0.008
S4P	NIR vs IR	0.0032
S4V	shC NIR vs shT NIR	0.6117

	shC NIR vs KO NIR	0.3908
	shC NIR vs shC IR	>0.9999
	shC NIR vs shT IR	0.0703
	shC NIR vs KO IR	0.2481
S4U	shC NIR vs shT NIR	>0.9999
	shC NIR vs KO NIR	>0.9999
	shC NIR vs shC IR	0.0181
	shC NIR vs shT IR	0.8314
	shC NIR vs KO IR	0.9309
S4W	shC NIR vs shT NIR	0.7472
	shC NIR vs KO NIR	0.9522
	shC NIR vs shC IR	>0.9999
	shC NIR vs shT IR	0.0015
	shC NIR vs KO IR	0.0032
S6C	NIR vs 5x2Gy	0.1216
S6E	NIR vs 5x2Gy	0.0253
S6F	NIR vs NIR + MP5	0.9995
	NIR vs IR	0.8065
	NIR vs IR + MP5	0.6839
	IR vs IR+ MP5	0.9958